University of
Zululand

Single muon production as a function of charged-particle multiplicity in proton-proton collisions at 8 TeV with ALICE at the LHC

By

Nomvelo G. Dindikazi

A DISSERTATION SUBMITTED IN PARTIAL FULFILLMENT OF THE
REQUIREMENTS FOR THE DEGREE OF

MASTERS IN SCIENCE
(PHYSICS)

Supervisor: Dr. S.S Ntshangase
University of Zululand

Co-Supervisor: Dr. Z.E Buthelezi
iThemba Laboratory for
Accelerator Based-Sciences

University of Zululand
2017

DECLARATION

I, Nomvelo Gqikazi Dindikazi, declare that the dissertation, which I hereby submit for the degree, Master of Science (Physics), at the University of Zululand, is my own work and has not previously been submitted by me for a degree at this or any other tertiary institution.

Signature: ....

Date: ....

I dedicate this thesis to my lovely family for their love and support. And everyone who believed in me when I did not beleieve in myself.

ACKNOWLEDGEMENTS

Special thanks goes to my supervisor Dr Z.E Buthelezi, for her guidance, encouragement and patience. Although I was difficult most of the time, she never gave up on me, she agreed to supervise me when I knew nothing about particle physics. Her wisdom did not only contribute to my proffesional growth, but I also grew mentally and personally. Thank you for taking your time to groom me, and for always having your door open when I needed help.

Thanks to Dr M Marchisone for helping me with the analysis and for the comments and contributions to this dissertation, not forgetting my fellow students Kgotlaesele Senosi and Sibaliso Mhlanga it would have been very difficult doing this work without their assistance. I also thank them for being with me through sleepless nights. In addition, my gratuity goes to Dr S.V Förtsch and the whole ALICE team. Also to South Africa CERN for funding my trips to CERN, I am thankful for the opportunity.

I am also very greatful to Dr S.S Ntshangase, for motivating me to pursue postgraduate studies, which lead to me having this wonderful experience. I am also greatful to everyone from the University of Zululand and the Univeristy of the Western Cape Department of Physics, who had an impact in my studies to get me where I am today. I appreciate the financial support from the National Research Foundation.

And to all my friends and family, thank you for your love and support, for being there when I was very stressed and felt like giving up. And I would like to thank everyone who was there for me through this exciting, fruitfull and strenous time.

To those whom I may have forgotten to mention, Je suis désolé.

ABSTRACT

At the Large Hadron Collider (LHC), ALICE (A Large Ion Collider Experiment) is a general purpose heavy-ion detector. ALICE is also studying proton-proton collisions, both as a reference for lead-lead and proton-lead collisions, and in physics areas where ALICE is competitive with other LHC experiments.

Heavy flavours (charm and beauty quarks) are formed in the initial stages of the collision through gluon fusion, which is a dominant process at the LHC. The study of heavy flavour production in proton-proton collisions at the LHC, provides an important test of perturbative Quantum Chromodynamics (pQCD) calculations, particularly in the forward rapidity of ALICE ($-4 < \eta < -2.5$), where their production is expected to be sensitive to small gluon Bjorken-x values, in parton distribution functions (PDF). In addition, the investigation of heavy flavour production in proton-proton collisions, also constitutes an essential baseline for the corresponding measurements in heavy ion collisions.

In this study, the production of heavy flavours is measured via the contribution of their muonic decay to the inclusive p_T-differential muon yield, as a function of relative charged particle multiplicity, reconstructed in proton-proton collisions at 8 TeV.

TABLE OF CONTENTS

LIST OF FIGURES

LIST OF TABLES

CHAPTER 1

INTRODUCTION

The Large Hadron Collider (LHC)[CER08] explores an unprecedented energy regime, where new physics has been observed [A$^+$15a, Col15a, DG$^+$13, Col16a, Col16c, Col12d]. At the LHC, proton-proton (pp) collisions are an important part of the program as they give a baseline and reference for heavy ion collisions, e.g, (PbPb) and (pPb) at these energies. In addition, pp collisions at the LHC are useful for understanding the background [Col12h, ATL10, C$^+$12] in rare phenomena (high transverse momentum (p_T)[1] events), such as the search for the Higgs and Super Symmetry (SUSY) [Zer14]. In these events, the background is mainly charged particles from minimum bias[2], pileup[3] and low p_T events (underlying events) occurring simultaneously with high p_T.

At the energy regime of the LHC, the measurement of multiplicity of produced particles in an acceptance of a given detector provides essential information about the global characteristics of a collision. In particular, in high energy pp collisions, the multiplicity of charged particles tells us about the number of primary charged-particles generated per event. It is a key observable to characterize the hadronic final state - hadrons[4] produced in an event before the decay into charged particles occurs.

---

[1] Transverse momentum - The component of momentum perpendicular to the beam line, associated with whatever physics that happened at the vertex. It is defined by $p_T = \sqrt{p_x^2 + p_y^2}$.

[2] Minimum bias refers to the trigger designed not to introduce a bias towards events containing high p_T particles as well as events containing many particle

[3] pileup is when a single bunch crossing produces several separate events in high-luminosity colliders

[4] hadrons are composite particle made of quarks held together by the strong force

At LHC energies multiplicity measurements are crucial, as they are used to test the ability of theoretical models, such as those incorporated in Monte Carlo event generators, e. g. as PYTHIA [S^+06] and PHOJET [GS04], to reproduce data at these energies. Event generators are used to simulate particles produced in collisions, by combining theoretical calculations such as perturbative quantum chromodynamics (pQCD) with phenomenological approaches. To simulate high-energy pp collisions, interactions involving a large momentum transfer (hard processes), are calculated using pQCD, while low momentum transfer interactions (soft processes) are calculated using different phenomenological approaches. Thus, an accurate simulation of the low momentum part is particularly important because a typical pp collision at the LHC includes multi-parton interactions (MPI) - a soft process. Consequently, a comparison of multiplicity measurements at LHC energies with theoretical predictions, enables a better tuning of these models to accurately simulate minimum bias as well as underlying event. The charged-particle multiplicity of these events is used to study the properties of soft interactions. Typically, measured distributions for multiplicity include the number of charged particles per event, N_{ch}, the number of charged particles as a function of pseudo-rapidity[5] ($dN_{ch}/d\eta$) or as a function of the transverse momentum, dN_{ch}/d_{p_T} .

Since the start of the LHC in 2009 several papers have been published on multiplicity studies [Col10c, Col12c, Col13, Col15b, Col11c, Col11d, Col10a]. For example, in [Col10b] it was observed that at the LHC the highest charged-particle multiplicities are comparable with those measured in heavy-ion collisions at lower energies, e. g, UA5 measurements [Col89] at the same energy as shown in Figure 1.1. It was observed that the charged-particle multiplicity increases with increasing collisional energy. In addition, data obtained by ALICE [Col10c] were found to be consistent with those obtained by CMS [Col10a], and when compared to various models for which they provide further constraints. These measurements therefore provide important inputs for tuning the theoretical models mentioned above.

---

[5] η - describes the angle of the particle relative to the beam axis and can be determined by equation $\eta = -\ln\left(\tan\frac{\theta}{2}\right)$.

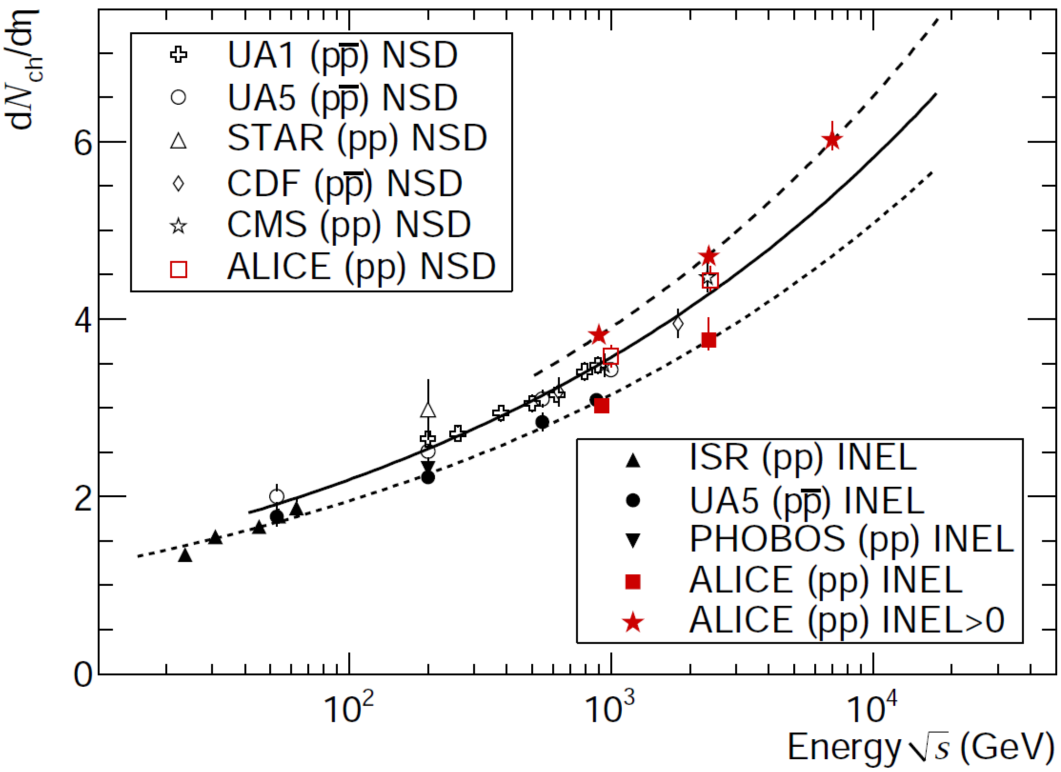

Figure 1.1: Charged particle pseudo-rapidity density in the central pseudorapidity region $|\eta| < 0.5$ for inelastic and non-single diffractive collisions, and in $|\eta| < 1$ for inelastic (INEL) collisions with at least one charged particle in that region (INEL>0$|\eta|$<1), as a function of the centre-of-mass energy. [Col10c].

As pp collisions provide a base line for heavy ion collisions, according to [B+13] it remains questionable if the small system size created in pp or pPb collisions could exhibit collective, fluid-like, features due to early thermalization, as observed in PbPb collisions. It is suggested that a relevant way to tackle this issue is to probe production mechanisms, correlations and event shapes as a function of the particle multiplicity. One way to investigate particle production is to extract the charged-particle transverse momentum spectrum or the average transverse momentum, $<p_T>$, as a function of multiplicity, N_{ch}, as it carries information about the underlying particle production mechanism. The first moment was reported in [Col82] and has been studied by many experiments at hadron colliders in pp collisions covering energies from $\sqrt{s} = 31$ GeV up to 7 TeV [Col10d, Col11a, Col11c]. In these studies an increase of $<p_T>$ with multiplicity was observed. In particular, it was observed that the $<p_T>$ increases also with collisional energy. These results were confirmed by the ATLAS Collaboration [Col11d, Col10e] and were reproduced by PYTHIA [S+06]. This strong increase of <p_T> with N_{ch} is understood in models of pp collisions as an effect of color reconnections between strings produced in multiple parton interactions (MPI). Despite PYTHIA [S+06] giving a good description of experimental data, however, a full consistency of models with data is still needed, as other investigated models, e.g, PHOJET [GS04] did not fully describe the data well. Since data at LHC energies provides a wide momentum range from low p_T (less than 0.5 GeV/c) to high momentum range, it therefore provides an additional input to the models.

In Monte Carlo event generators, high multiplicity events are perceived a result of MPI [Col14b], therefore, the observed strong correlation between the <p_T> and N_{ch} is attributed to MPIs. Hence, in high energy pp collisions, it is crucial to consider that MPIs can induce a dependence of the particle production on the charged-particle multiplicity of the event. The multiplicity of charged particles becomes a direct measurement of the number of partonic interactions in pp events. However, MPIs are a low momentum transfer process which, according to PYTHIA [S+06], is expected to affect the production of light quarks (e.g, up (u) and down (d) quarks) and gluons. This means that the production of heavy quarks, charm and beauty quarks, also known as heavy flavour, and their bound states (charm-anticharm, etc) should not be influenced by MPIs, and their production rates should then be independent of the charged-particle multiplicity of the event. But, it is also expected that at high centre-of-mass energies reached at the LHC, there might be a substantial contribution of MPI on a harder scale [Col12f]. Such hard MPIs can induce a correlation between the yield of heavy quarks and the total charged particle multiplicity.

1.1 Heavy quark production vs multiplicity in pp collisions with ALICE

Heavy quarks, which consists of charm (e.g, $D^0, D^{\pm}$) and beauty (e.g, $B^0, B^{\pm}$) and their bound states of charm-anticharm (c$\bar{c}$ e.g, J/Ψ) and beauty-antibeauty (b$\bar{b}$, e.g, upsilon (ϒ)) are formed in the initial stages of the collision through gluon fusion, a dominant process at LHC energies [A$^+$74]. As shown in Figure 1.2, copious amounts of heavy quarks are produced at LHC energies [Col12e, Col14a].

The study of heavy-flavour production in pp collisions at the LHC provides an important test for calculations of pQCD processes. Particularly, the production of heavy quarks is expected to be sensitive to small Bjorken-x[6] [Z$^+$12]. In ALICE [Col08a], heavy quarks are measured in the central barrel ($|\eta| < 0.9$) via the electronic [Col14a] as well as the hadronic [Bal11] decay channels, and in the forward region ($-4.0 < \eta < -2.5$) via the muonic channel [Col12b, Col11b]. Of note to our study, are the results obtained from the study of J/ψ production, as a function of charged particle multiplicity in pp collisions at $\sqrt{s} = 7$ TeV [Col12c] as well as from the measurement of charm and beauty production at central rapidity[7], versus charged-particle multiplicity in pp collisions at 7 TeV [Col15b]. In both studies, it was observed that the yield of heavy quarks increases linearly with multiplicity, see Figure 1.3. Clearly there is evidence of a correlation between heavy-flavour and charged-particle multiplicities. This behaviour is not expected, since heavy-flavour production is dominated by hard processes, while charged-particle yields are associated to the soft momentum scale processes. These results might be interpreted as either indicating that heavy quark production in pp collisions is always connected with a strong hadronic activity, or that MPIs could also affect the high momentum scales relevant for heavy quark production. In [Col12c], it was concluded that further studies of charged-particle multiplicity dependence of heavy quark production are therefore necessary to shed more light on the nature of the observed effect.

---

[6] Bjorken-x - is the fraction of longitudinal momentum carried by the two interacting partons.

[7] Rapidity is a representation of the speed of motion of the particle and can be determined by the equation, $y = \frac{1}{2}\ln\left(\frac{E+p_z}{E-p_z}\right)$.

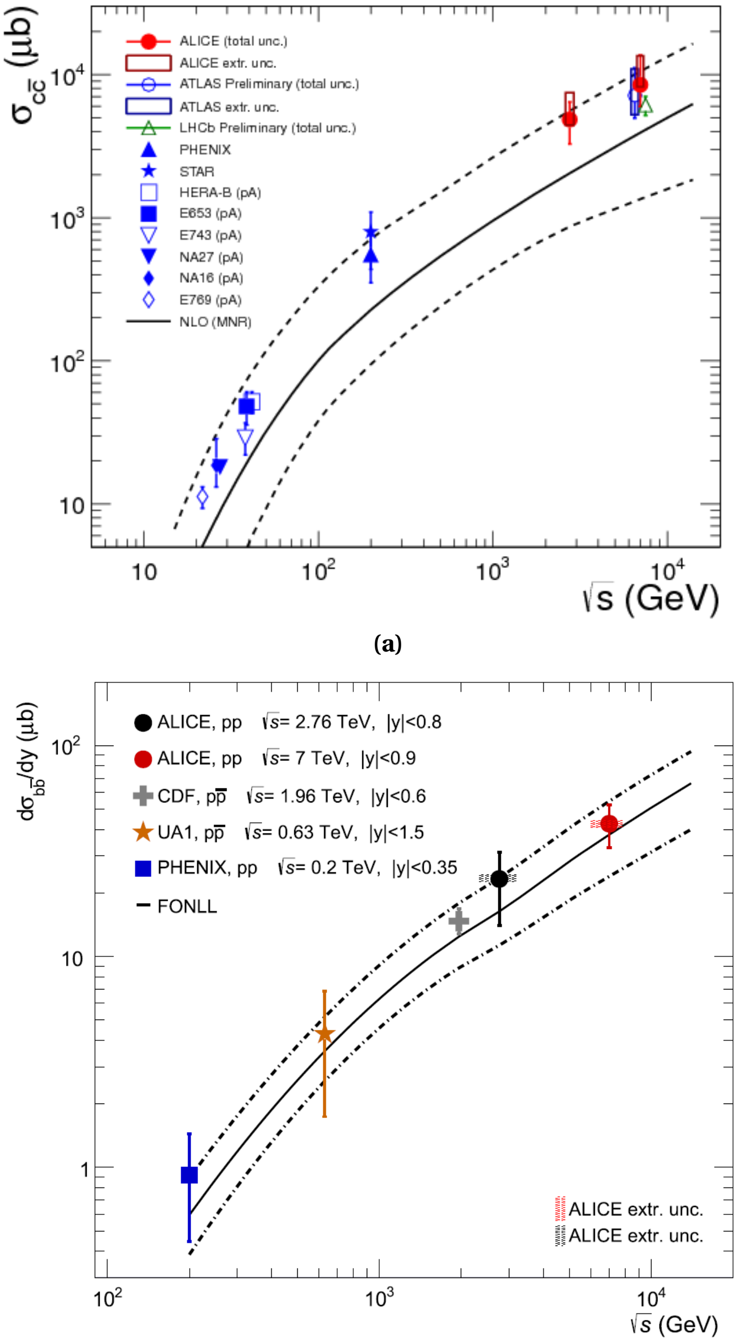

(a)

(b)

Figure 1.2: The energy dependence of the total nucleon-nucleon (a) charm and (b) beauty production cross section at the LHC compared to low energy experiments and theoretical models [Col12f, Col14a].

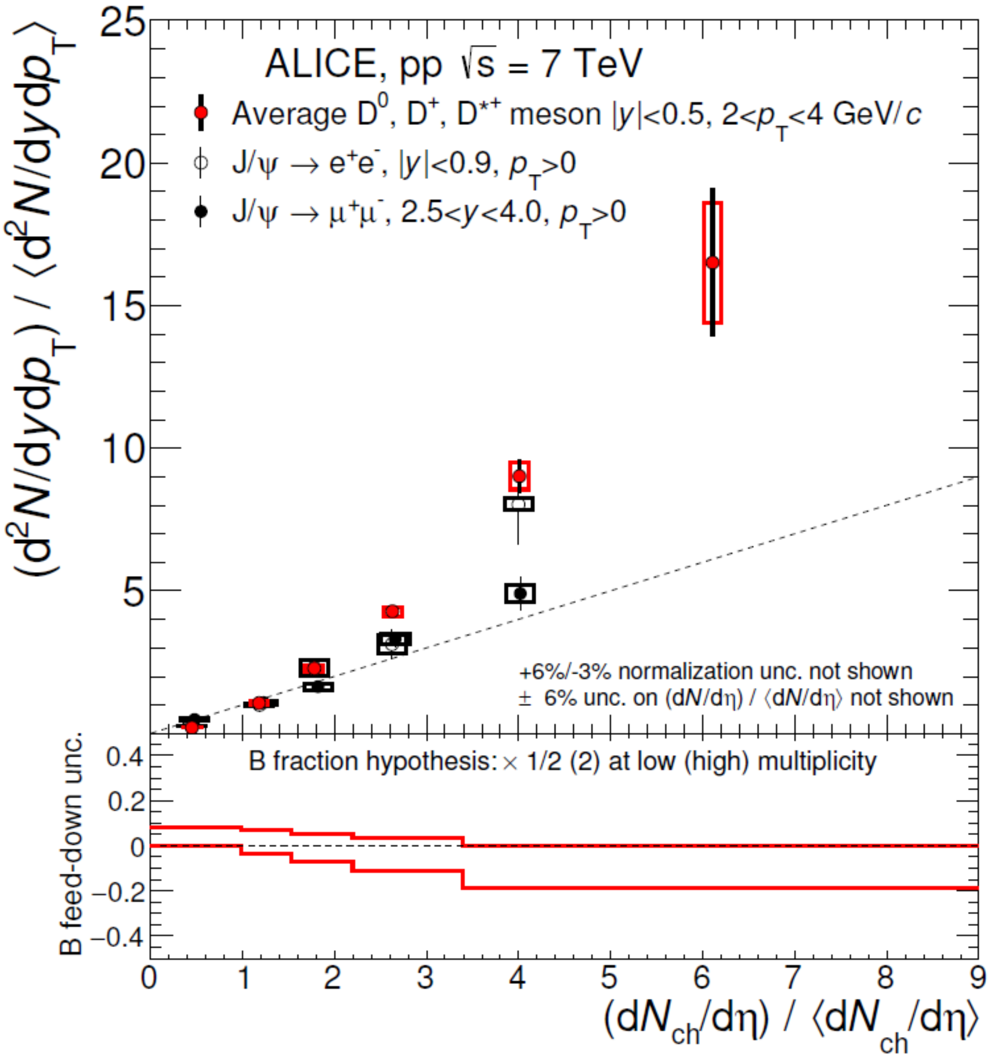

Figure 1.3: Average D meson and inclusive J/Ψ relative yields as a function of the relative charged-particle multiplicity at central rapidity. D-meson yields is shown for $2 < p_T < 4$ GeV/c, while J/Ψ yield is for $p_T > 0$ [Col15b].

1.2 Purpose of the study

We are motivated by previous measurements [Col12c, Col15b] to study the production of single muons produced from the decays of heavy-flavours (charm and beauty) in the forward rapidity ($-4.0 < \eta < -2.5$), as a function of charged-particle multiplicity in the central barrel ($|\eta| < 1$), in proton-proton collisions at 8 TeV in ALICE. The Top quark is also massive but in ALICE due to design of the detector (limitation in cross section) for pp collisions, we only measure charm and beauty. As discussed in previous sections, at LHC energies, pp collisions are expected to be dominated by MPIs, which involve only light quarks and gluons (soft processes). On the contrary, heavy-flavours are produced at the early stages of the interaction through hard scatterings. Thus it is expected that their production will not be affected by the MPI and therefore will be independent of the charged-particle multiplicity of the event. This study, together with previous studies [Col12c, Col15b] will provide more insight on the interplay between hard (high p_T) and soft (low p_T) interactions in the context of multi-partonic interactions (MPI) and underlying event in heavy flavour and heavy quark production at LHC energies in pp collisions.

1.3 Muon measurement in ALICE

The muon (an unstable subatomic particle with a mean lifetime of 2.2 μs, much longer than many other subatomic particles) is a lepton which decays to form an electron or positron. Muons have a mass of $105.7 MeV/c^2$, which is about 207 times that of the electron. Due to their greater mass, muons are not as sharply accelerated, when they encounter electromagnetic fields, and do not emit as much bremsstrahlung (deceleration radiation). This allows muons of a given energy to penetrate far more deeply into matter than electrons, since the deceleration of electrons and muons is primarily due to energy loss, by the bremsstrahlung mechanism. As a consequence, in a given material, the rates of energy loss through ionization and bremsstrahlung is much larger for muons than for electrons. As a result, muons in general, do not produce electromagnetic showers and can thus be identified easily by their presence in the outermost detectors, as all other charged particles are absorbed in the calorimeter system. This is best illustrated in Figure 1.4. In ALICE, muons are measured at forward rapidity, where the muon spectrometer is located.

There are four major experiments around the LHC ring, namely: ATLAS (A Toroidal LHC Apparatus) [Col08c], CMS (Compact Muon Spectrometer) [Col08d], LHCb (LHC-beauty) [Col08e] and ALICE - A Large Ion Collider Experiment [Col08a]. The ALICE detector is composed of the central barrel, in the pseudorapidity $|\eta| < 0.9$, and the forward muon spectrometer in the region $-4 < \eta < -2.5$. As illustrated in Figure 1.5, in ALICE, the central barrel detectors cover the pseudorapidity region which is complementary to that covered by the ATLAS [Col08c] and CMS [Col08d] detectors, while the forward rapidity of ALICE, which is

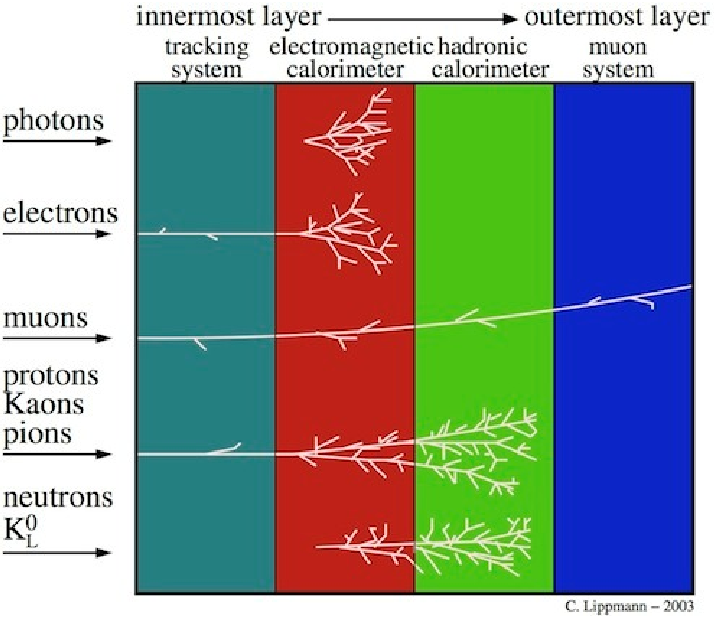

Figure 1.4: Particle identification of muons vs other particles. [Lip12].

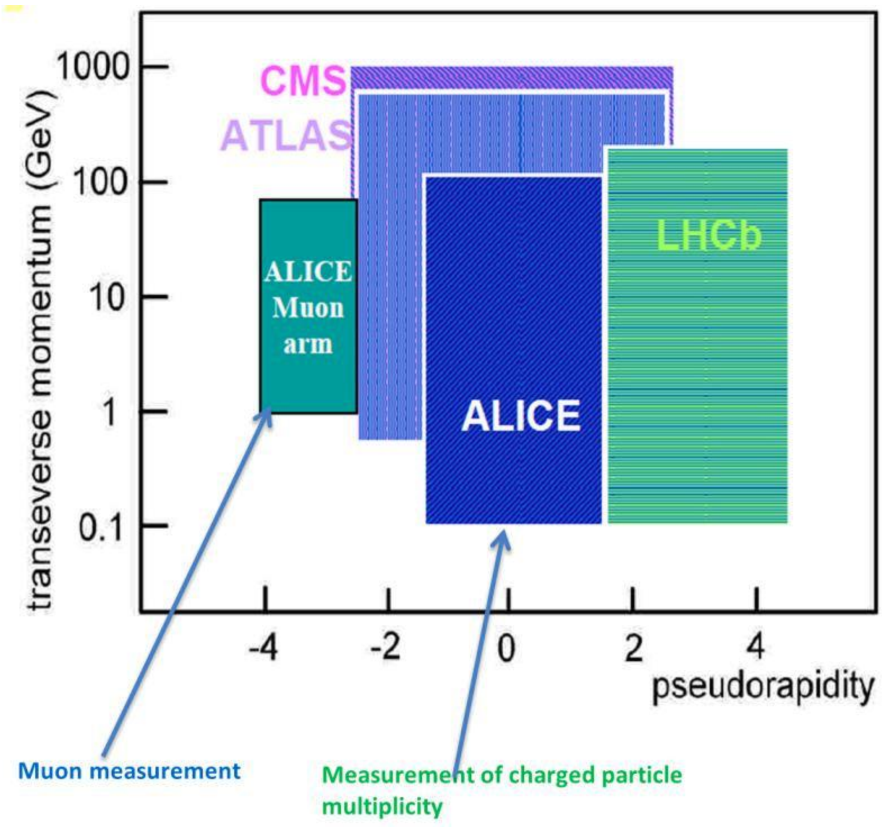

Figure 1.5: The pseudorapidity plot illustrating that ALICE is well suited to measure multiplicity and open heavy flavor, with respect to other experiments.

covered by the muon spectrometer, is complementary to the pseudorapidity region covered by the LHCb experiment. The production of heavy-flavours at the LHC probe the Bjorken-x range indicate in Figure 1.6. In particular, in the forward rapidity of ALICE, we probe Bjorken-x values as indicated in Figure 1.7. Thus, we are sensitive to quark parton distribution functions (PDFs) at high momentum transfer Q^2 (Q~$M_{b/c}$). In Figure 1.7, the x is the fraction of the beam particle momentum carried by a parton involved in hard scattering. It is given by equation 1.1

$$x_{1,2} = (M/\sqrt{s})e^{\pm y} \tag{1.1}$$

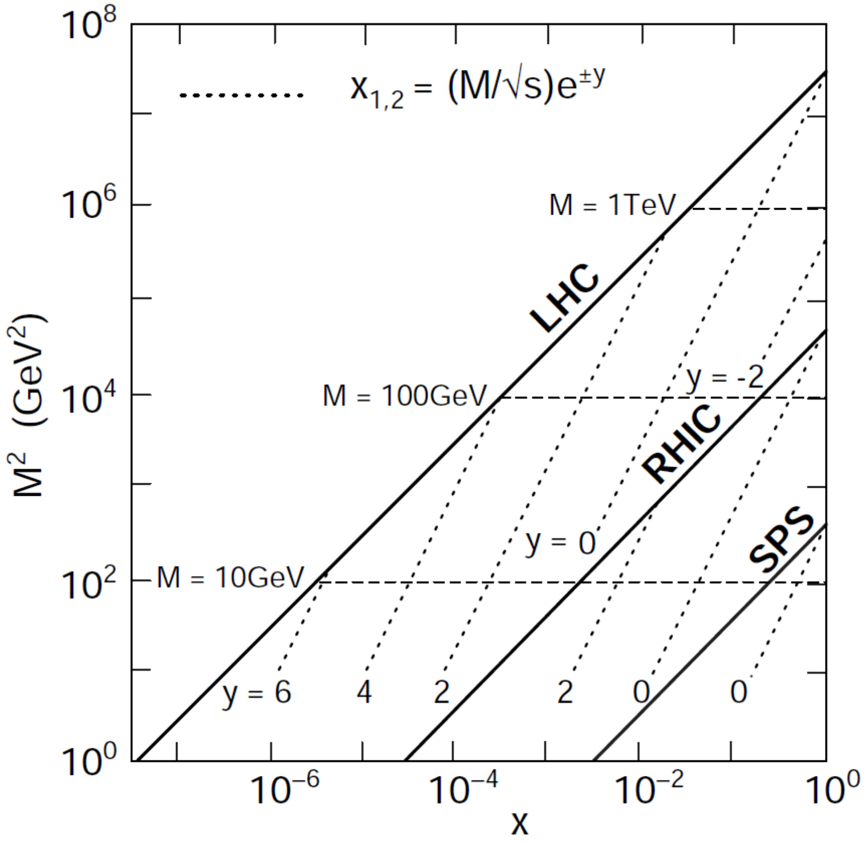

Figure 1.6: Bjorken-x as a function of M^2 for particle production in nucleon-nucleon collisions at the SPS, RHIC and LHC. The lines correspond to constant rapidity at corresponding energies [C⁺04].

where, $\sqrt{s}$ is the centre-of-mass energy for a particle of mass $M_{b/c}$, and y is the rapidity. In this regard, the ALICE detector is capable of the measurement of heavy-flavours and is a suitable instrument for studying pp collisions. From [Col12b], it is deduced that ATLAS

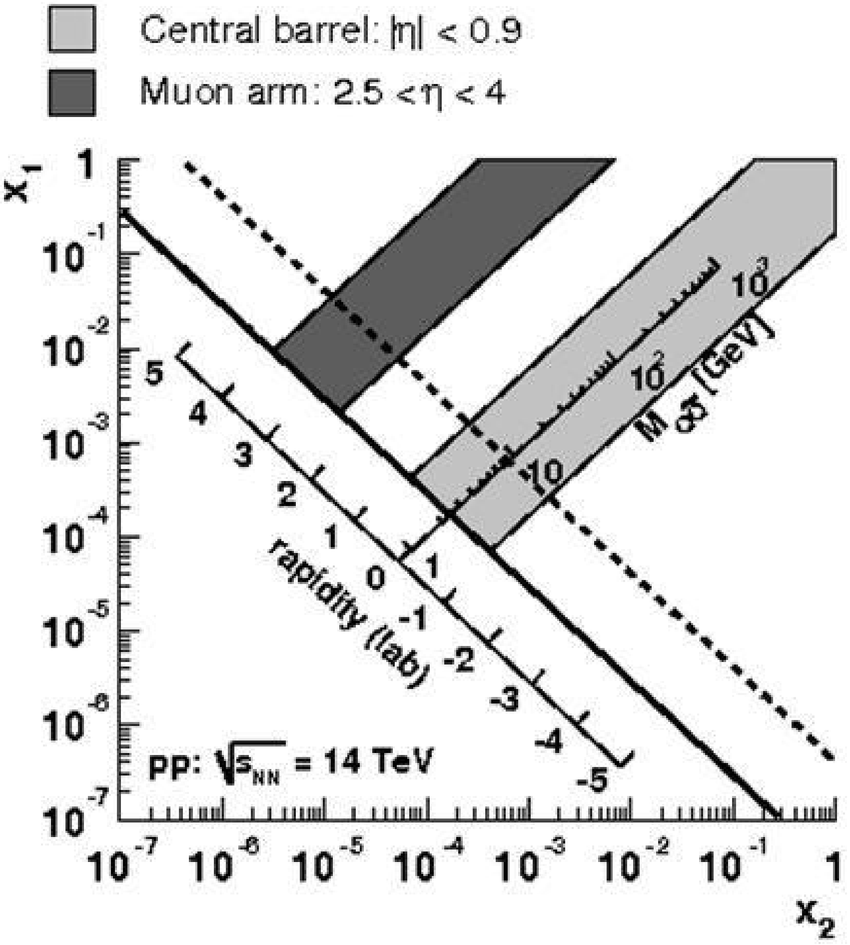

Figure 1.7: Accessible Bjorken-x range for heavy flavours in pp collisions at $\sqrt{s}$ = 14 TeV in the rapidity range that can be measured with ALICE at the LHC. [Z+12].

measurements for electrons and muons from heavy flavour in pp collisions at 7 TeV are consistent with pQCD theoretical calculations [Col12i]. In ATLAS the electrons and muons are reconstructed at midrapidity, thus, it would be complementary to measure muons from heavy-flavour production in the forward rapidity in ALICE, and compare with models.

1.4 Thesis outline

Chapter 2 consists of the theoretical background. Chapter 3 describes the ALICE experiment, with more focus on the Muon Spectrometer. Also, details of data taking conditions, as well as the ALICE online and offline framework will be given. Chapter 4 is dedicated to the analysis of the study. This includes the charged-particle multiplicity as well as the measurement of the inclusive muon p_T-differential yields, and the description of the Monte-Carlo simulation, performed in order to determine the acceptance and efficiency used to correct the muon yields. In Chapter 5, the final results will be shown and discussed. Chapter 6 gives the summary and conclusions.

CHAPTER 2

THEORETICAL BACKGROUND

This chapter is dedicated to the theoretical background applicable to high energy pp collisions. A brief description of the Standard Model of particles (QCD), as well as theoretical aspects related to the production of heavy quarks and charged particle multiplicity in these collisions.

2.1 Overview of the standard model

The Standard Model (SM) includes members of several classes of elementary particles, arranged in three families: namely, quarks, leptons and gauge bosons. As shown in Figure 2.1 the particles involved in the SM are characterized by their spin, mass, and quantum numbers (charges) which determine their interactions. Quarks and leptons (the fundamental constituents of matter) are fermions. The fermions (spin = 1/2) have identical quantum numbers and different masses. The heavier families are unstable and decay into the lightest one, which makes up most of the ordinary matter. The families of fermions are differentiated by their charges under strong and electromagnetic interactions. The up (u), down (d), charm (c), strange (s), top (t) and bottom (b) quarks are charged under the strong interactions. Of the leptons only neutrinos are not charged, while the electron (e), muon (μ), and tau (τ) are charged . The neutrinos are neutral under both the strong and the electromagnetic interactions (they feel weak interactions) and they are at least six orders of magnitudes lighter than all other SM fermions. The masses of the SM fermions span a range going from the sub-eV neutrino masses to the 1.7×10^2 GeV top mass [GL66].

Quarks have fractional charges (-1/3 or +2/3) and have an additional intrinsic property called colour charge. Quarks and leptons are held together by fundamental forces which are represented by the exchange of particles known as gauge boson: namely, photons (γ), gluons (g) and electroweak bosons which are (W+, W- and Z). Bosons have an integer intrinsic spin. The photon and the Z boson are neutral. Unlike quarks, the gluon is electrically neutral and it carries a colour charge. The standard model also includes the Higgs boson, which was recently discovered and confirmed by experiments at the LHC [Col12j, Col12a]. The Higgs boson is a spin-0 neutral particle, which gives account of the masses of particles.

Quarks and antiquarks are held into hadrons by gluons, the carriers of the strong force. The strong force is governed by the theory of Quantum chromodynamics (QCD), which suggests the existence of the strong colour charge that is associated with quarks, and gluons and is responsible for the strong interaction.

Other recent particle discovery was made by the LHCb experiment, also at the CERN LHC. They discovered the new class of particle known as the pentaquark [Col15a]. These particles represent a way to aggregate quarks in a pattern that has never been observed. The study of its properties may allow better understanding of how ordinary matter (protons and neutrons) from which we are all made, is constituted.

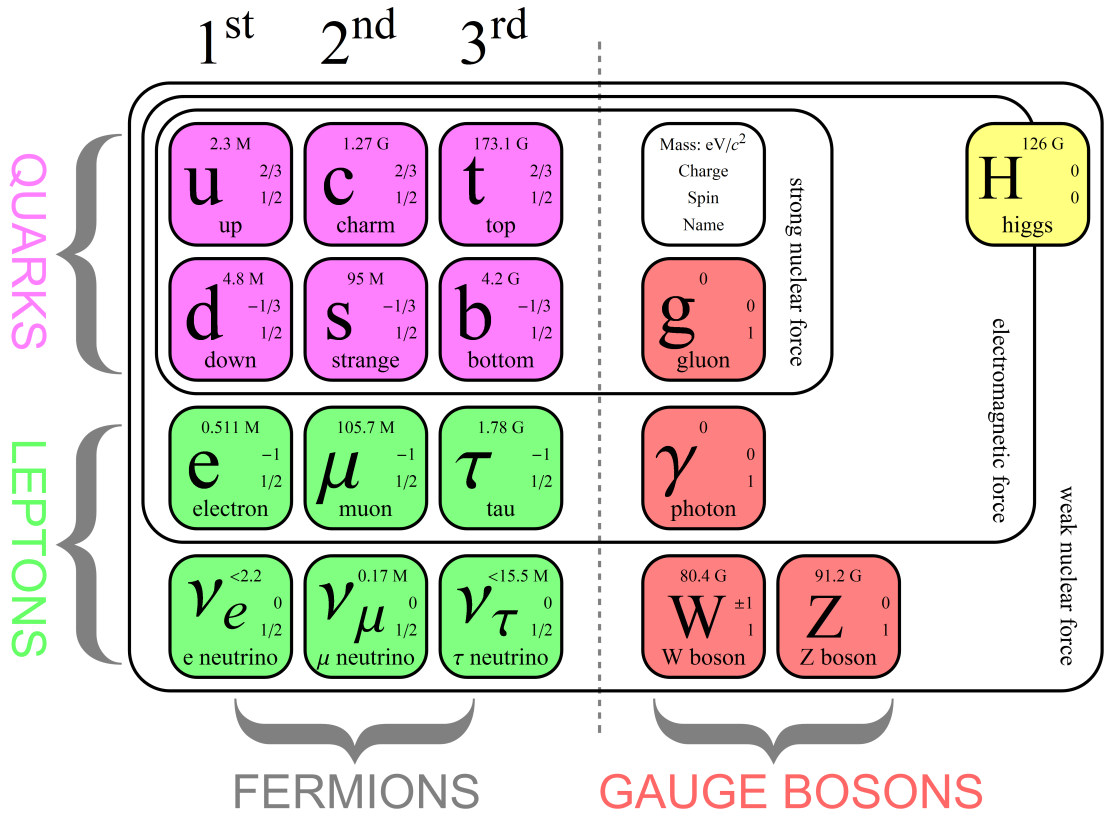

Figure 2.1: The Standard Model of Particle Physics [PI15].

2.2 Quantum Chromodynamics (QCD)

QCD is the theory of strong interactions, which describes the interactions of quarks via their colour quantum numbers. QCD is a type of quantum field theory called the non-abelian gauge theory, with symmetry SU(3) [Hal84]. The QCD Lagrangian [Shi98] controls the dynamics of the quarks and gluons. Detailed QCD calculations with the Lagrangian indicate that the potential between two heavy quarks is of the form shown in equation 2.1.

$$V(r) = \frac{-\alpha(r)}{r} + \sigma r \tag{2.1}$$

where r is the distance between the quarks, α is the coupling constant of coulomb-like term and σ is the string constant which gives the strength of the quark "confinement". For small r, the first term dominates. At larger r, the potential energy of two quarks increases with separation until enough energy is present to form a new quark-antiquark pair, which occurs if the quarks are separated. As quarks come closer to each other, the chromodynamic binding between them weakens [WD06]. On the other hand, as the distance between quarks increases, the binding force strengthens. The colour field becomes stressed and more gluons of the appropriate colour are spontenously created to strengthen the field. Above a certain threshold, pairs of quarks and anti-quarks are created. These pairs bind the quarks being separated, causing new hadrons to form. As a result, quarks are never observed individually, but always as part of a 3 quark state (baryon) or a quark-antiquark state (meson) [Vel03, Yul02]. In other words they are part of hadrons. This property is known as confinement.

Colour confinement is the physics phenomenon that postulates that colour charged particles, such as quarks, cannot be isolated, and therefore cannot be directly observed. Quarks, by default, clump together to form two types of hadrons (the mesons and the baryons composed of quark and antiquark, and three quarks respectively). The constituent quarks in a group cannot be separated from their parent hadron, and this is why quarks can never be studied or observed in any more direct way than at a hadron level. This process is known as hadronization and occurs before quarks formed in a high energy collision are able to interact in any other way.

Two different types of symmetry exist: one that acts on different colours of quarks (gauge symmetry mediated by gluons) and flavour symmetry which rotates different flavours of quarks to each other, flavour SU(3), which is an approximation of the vacuum of QCD and is not a fundamental symmetry but is an accidental consequence of small mass of the three lightest quarks (u, d and s). As the strong interaction does not discriminate between different flavours of the quark, QCD has approximate flavour symmetry (flavours may be interchanged without affecting the physics in an interaction), which is broken by differing masses of the quarks. There are additional global symmetries whose definitions require the chirality[1]. Chirality and handedness are not the same but approximately equal at high energies. Chiral symmetries involve independent transformations of two types of particles. Chiral symmetry is spontenously broken by the QCD vacuum. The QCD vaccum is characterized by infinitely many non-vanishing condensates, such as the gluon or quark con-

---

[1] discrimination between left and right-handed particles. If the spin of a particle has a positive projection on its direction of motion it is called left-handed; otherwise, it is right-handed

densates that, in turn, characterize the normal phase or confined phase of quark matter [K+11, And14]. QCD vacuum involves the screening of $q\bar{q}$ pairs and anti-screening of gluon pairs, which are coloured charged particles. As a result, the intensity of the strong interaction diminishes at short distances (high energies).

In contrary, the interaction between quarks is reduced as the distance between them reduces, and tends to zero as the distance between them reduces to zero. This means that the interaction between quarks increases as they are separated by larger distances (low energies). This phenomena is known as asymptotic freedom.

There is no analytic proof that QCD should be confining, but intuitively, confinement is due to the force-carrying gluons having colour charge [Kou11]. One can compare the electromagnetic interaction with the strong interaction. As any two electrically charged particles separate, the electric field between them decreases quickly, allowing electrons to become unbound from nuclei. But as two quarks separate, the gluon fields form narrow tubes (or strings) of colour charge, which tend to bring the quarks together as though they were some kind of rubber band. This is quite different in behaviour from electrical charges. Because of this behaviour, the colour force experienced by the quarks in the direction that holds them together, remains constant, regardless of their distance from each other. This can be explained using the coupling constant of the QCD in Figure 2.2 [Bet07]. The strong coupling constant is defined using equation 2.2.

$$\alpha_{QCD}(Q^2) = \alpha_s = \frac{4\pi}{(11-23n_f)ln\left(\frac{Q^2}{\Lambda^2_{QCD}}\right)} \tag{2.2}$$

where, Q^2 gives the scale of the interaction, α_{QCD} and α_s are the QCD coupling constants, n_f is the number of flavours and Λ^2_{QCD} is the QCD parameter determined by experiments.

For small values of Q^2 (small energies), the strong coupling constant has large values ($\alpha_s >> 1$). This explains the magnitude of the strong force and the fact that quarks are confined in neutral colour states: namely, the baryons and the mesons - colour confinement. This aspect of QCD is verified with Lattice QCD (lQCD) computations but is not mathematically proven, while the other aspect of non-pQCD [Max06] is the exploration of the

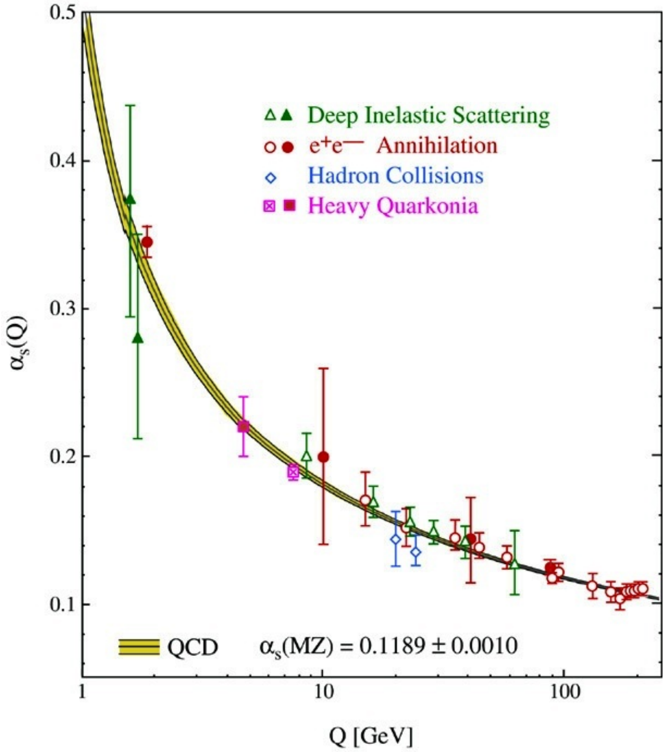

Figure 2.2: QCD coupling constant α_{QCD} [Bet07].

phase of quark matter. On the contrary, for high energies the momentum transferred is large and α_s becomes small; the quarks and gluons interact very weakly - asymptotic freedom [GW73, Pol73]. The bag model describes both confinement and asymptotic freedom by modelling hadrons as spherical bags, of radius R, within which partons (quarks and gluons) can move freely, but are prevented to escape outside R by an inward pressure due to colour confinement [BP97].

The discovery of asymptotic freedom in the strong interactions by David Gross, David Politzer and Frank Wilczek [GW73, Pol73], allowed physicists to make precise predictions of the results of many high energy experiments using the quantum field theory technique of perturbation theory. After the first evidence of gluons from PETRA experiments in 1979 [Cou04], experiments became more and more precise, resulting in the verification of pQCD at the level of a few percent, at the Large Electron-Positron (LEP) at CERN. The phase transition temperature between confinement and asymptotic freedom, has been measured by the ALICE experiment to be well above 160 MeV [A^+15b]. Below this temperature, confinement is dominant, while above it, asymptotic freedom becomes dominant.

2.3 Perturbative QCD (pQCD)

Perturbative QCD is a subfield of particle physics in which the theory of strong interactions, QCD, is studied by using the fact that the strong coupling constant α_s is small, at high energies or short distance interactions, thus allowing perturbation theory techniques to be applied. In most circumstances, making testable predictions with QCD is extremely difficult, due to the infinite number of topologically inequivalent interactions possible. Over short distances, the coupling is small enough that, this infinite number of terms can be approximated accurately by a much more manageable number of terms. Although limited in scope, this approach has resulted in the most precise tests of QCD to date.

The first and most clear test of pQCD is R measurement in e^+e^- annihilation [Bur97]. R is defined as the ratio of production rate for $e^+ + e^- \longrightarrow$ hadrons to that for $e^+ + e^- \longrightarrow \mu^+ + \mu^-$. Since only the total production rate is considered, summation over all final state hadrons cancelled the dependence on specific hadron type, and this R ratio can be calculated in pQCD strictly [Bur97].

Most of the processes cannot be calculated directly with pQCD since free quarks and gluons cannot be observed, due to colour confinement. This implies that the hadron structure has a non-perturbative nature. Fortunately, physicists developed the QCD factorization theorem, which separates the cross section into two parts: the process dependent pQCD calculable short-distance parton cross section, and the universal long-distance functions. Those universal long-distance functions can be measured with global fit to experiments. In such a way, a partly calculable prediction to particle reaction processes was obtained. This includes parton distribution functions (PDFs), fragmentation functions, multi-parton correlations functions, and so on. Several good experimental quantitative tests of pQCD at collider facilities include, the production of vector bosons, measurement of jet cross section, heavy quark production and many others.

2.4 Ultra-relativistic pp collisions

QCD is the underlying theory which explains the scattering processes (hard or soft) in high energy proton-proton collisions. For hard processes, the rates and event properties can be predicted with good precision using the perturbative theory. For soft processes, the rates and properties of the total cross section, and the underlying event, are dominated by non-pQCD effects, which are not well understood. It is very important for test of the theory and searches of new physics, to understand the rates and characteristics of predictions for hard processes, using pQCD.

Figure 2.3 illustrates the hard-scattering process for two hadrons A and B. The hard-scattering process for two incoming partons is characterized by the cross section $\hat{\sigma}$, given in equation 2.3, where the parton distribution function (PDFs), $f_{\frac{a}{A}}(x_a, \mu_F^2)$ and $f_{\frac{b}{B}}(x_b, \mu_F^2)$ describe the structure of the incoming hadrons. The PDFs $f(x, Q^2)$ for a parton, provide the probability density of finding a parton with momentum x at momentum Q^2, which defines the energy scale of the process. Figure 2.3 describes the probability to find a parton a in a hadron A with a momentum fraction x_a at the energy μ_F^2. To obtain the hadron-hadron cross section, a summation over all possible parton-parton scattering processes and an integration over the momentum has to be peformed.

The calculations of the hard-scattering process cross sections are performed in pQCD and the results depend on the strong coupling constant, α_s, and its renormalization scale μ_F, which is also the scale that separates long and short distance physics [CHS07]. Equation 2.3 can only be used to describe hard scattering events where the effective centre-of-mass energy of the interaction is far less than the centre-of-mass energy of the collider. Each interacting parton carries a certain fraction of the proton momentum which depends on its mass and rapidity (y). In Figure 2.4, as the up (u) and down (d) quarks contribute to the quantum numbers of the protons, they form the valence quarks. Therefore, they carry a large fraction of the proton momentum. This is shown in Figure 2.4, where a proton contains also gluons and other quarks that give rise to the so-called "sea" and they carry much smaller momenta. Parton momentum distributions depend on the momentum transfer in the interaction, Q^2. At large Q^2 the interacting particles see the short-distance structure of the proton and hence, have access to the "sea" of quarks and gluons inside the proton, in addition to the valence quarks. Consequently, the PDFs are shifted towards small x values, where x is the fraction of the proton momentum carried by the interacting partons, also known as the Bjorken-x [Ian14]. For small Q^2, only the valence quarks are visible and the PDFs peak at large x values. As Q^2 is very large at ultra-relativistic energies provided by the LHC, therefore there is access to more particles in a single pp collision, mostly gluons, as they dominate the small x region. Due to the high gluon density in each colliding proton, the short-distance hard scattering process occurs concurrently with multiple parton interactions (MPIs) [B+11], where two or more parton interactions occur simultaneously in a single collision.

$$\sigma = \sum_{a,b} \int dx_a . dx_b f_{\frac{a}{A}}(x_a, \mu_F^2) f_{\frac{b}{B}}(x_b, \mu_F^2) \hat{\sigma}_{ab}(x_a, x_b, \alpha_s(\mu_R^2)) \tag{2.3}$$

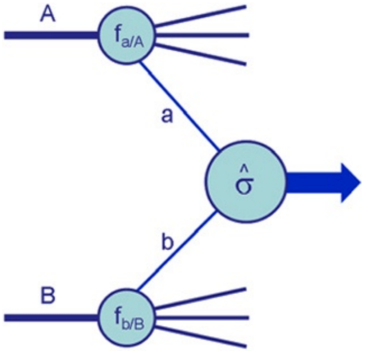

Figure 2.3: Structure of a generic hard-scattering process [C+07].

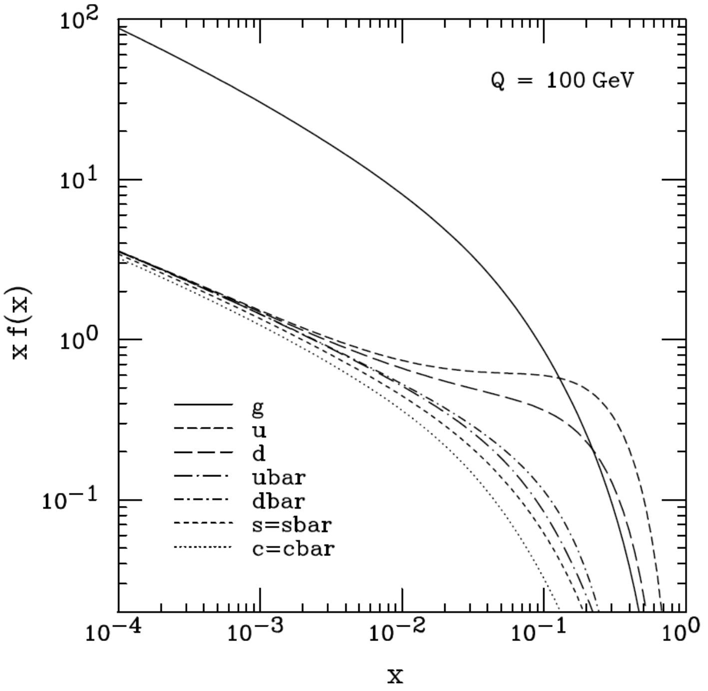

Figure 2.4: Parton distribution functions of the proton as a function of Bjorken-x [P+02].

2.5 Multi-parton interactions

Particle multiplicity is one of the basic observables in hadron and nuclear collisions. The measurement of multiplicity of charged-particle tells us about the number of charged-particles generated per event and it is a key observable for understanding multi-parton interactions (MPI - several interactions taking place at the parton level within a single proton-proton collision).

Multiple parton hard-scatterings, i.e, events in which two or more distinct hard parton interactions occur simultaneously in a single hadron-hadron collision, are possible due to the composite nature of hadrons. Generally, MPI take place in hadron-hadron collisions at high centre-of-mass energy, where several interactions can be hard (high momentum transfer processes). The effects cancel or are suppressed in sufficiently inclusive quantities but do affect final-state properties (e.g. Jets). MPIs are often split into two groups, soft and hard MPIs. In the case of hard MPI the resulting particles have a rather high p_T. Otherwise, it is called soft (low p_T process) MPI. While hard MPIs occur rather rarely, soft MPIs are very frequent processes. There can be even higher numbers of additional subprocesses which would lead to triple or even higher parton interactions (Figure 2.5). Because of gluon dominated PDFs, pp collisions at the LHC are dominated by MPIs. Most events are due to large distance collisions between the two incoming protons (a non-pertubative process). In this case the momentum transfer of the interaction is small (soft collisions) and therefore a particle scattering at large angles is suppressed. The particles produced in the final state of such interactions have large longitudinal momentum, but small transverse momentum (p_T) relative to the beam line. Due to several interactions occurring at parton level in the collision, particle production becomes dependent on the total charged-particle multiplicity. Head-on collisions may occur occasionally between two partons of the incoming protons. These are interactions at small distances, and are characterized by large momentum transfers (hard MPI). In this case, particles in the final state can be produced at large angles with respect to the beam line (high p_T), and massive particles can be created.

Multi-parton interactions are expected to be dominated by soft (small momentum transfer) processes, thus are useful to study QCD in the non- perturbative regime and to constrain phenomenological models and event generators. Such studies are also important for the understanding of backgrounds for measurements of hard (high momentum transfer) and rare interactions.

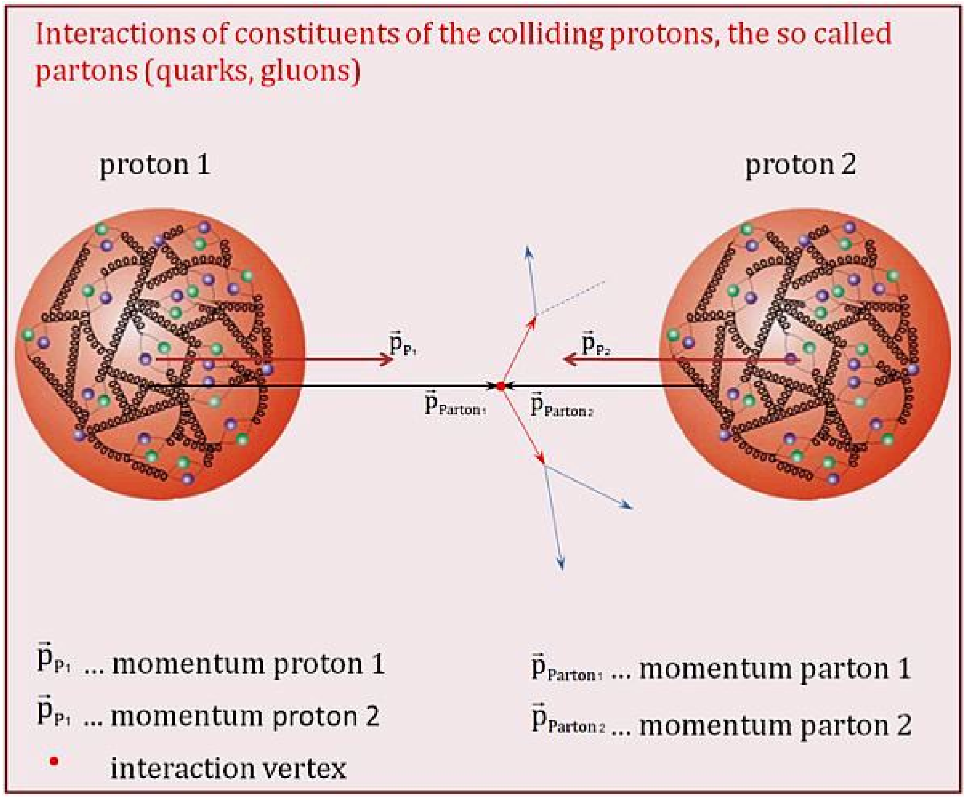

Figure 2.5: A view of multi-parton interactions [Kon15].

2.6 Heavy flavour production in pp collisions

In high energy collisions heavy flavours, charm and beauty quarks are formed in the initial stages of the collision, predominantly through gluon-gluon fusion processes, as illustrated by Feynman diagrams in Figure 2.6. Their production cross sections are significantly affected by parton dynamics in the small-x regime (high energy collisions). Heavy-quark mass acts as a long distance cut-off, so that the partonic hard-scattering process can be calculated in the framework of pQCD, down to low transverse momenta (p_T). The measurement of heavy flavour production in pp collisions provides valuable information about the mechanisms involved in the parton interaction. However, it must be noted that available theoretical models do not give a complete and accurate description of such mechanisms as non-perturbative phenomena, which have important contribution to heavy flavour production. Production cross section can be calculated with pQCD calculations, based on the factorization approach. Available calculations are done by matching the resummation of logarithms of the transverse momentum over the mass of the quark, at first-order-next-to-leading-logarithm (FONLL) [MCN98]. The results plus, next-to-leading-logarithm (NLO) / next-to-next-to-leading-logarithm (NNLO) [Vog08] and FONLL corrections are currently the basis of the heavy flavour calculations.

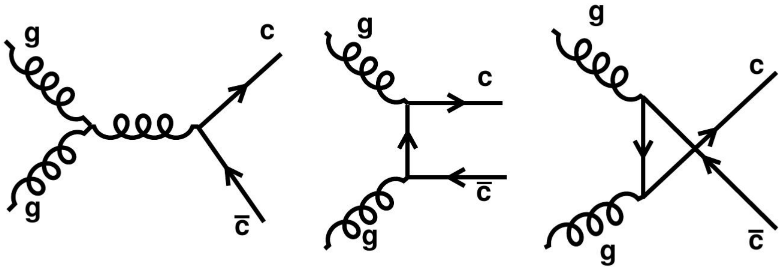

Figure 2.6: Feynman diagrams of heavy flavour production via gluon fusion, predicted to be dominant at LHC energies.

In the leading order process (LO) in hadronic collisions for heavy quark production, three mechanisms are considered, namely: flavor creation quark-antiquark annihilation ($q\bar{q} \to Q\bar{Q}$), gluon-gluon fusion ($gg \to Q\bar{Q}$), flavour excitation ($qQ \to qQ, gQ \to gQ$) and final-state gluon splitting ($g \to Q\bar{Q}$). The cross section of gluon-gluon fusion process is much higher than quark-antiquark annihilation process for high partonic energy systems. Thus, at the LHC, heavy quark production is dominated by gluon-gluon fusion processes. Heavy quarks produced via gluon fusion are back-to-back, i.e, they move in opposite directions with almost similar transverse momentum. In the flavour excitation process, the heavy quark is considered to be already present in the incoming hadron. It is excited by the exchange of a gluon with the other hadron and appears on mass-shell in the final state. Since the heavy quark is not a valence quark, it must be produced from the exchange of a gluon with the other hadron. The hard scattering in flavour excitation pair-production process, $g \to Q\bar{Q}$, must have a partonic energy virtually above m_{Q^2}, for the heavy quark to be present in the initial state. The heavy quark final states do not need to be back-to-back, as the third parton can carry away some transverse momentum.

Experimentally, the presence of hadrons containing heavy quarks is deduced by their decay products. Heavy flavours decay via weak interaction, i.e, a b-quark may decay into a c or u-quark, while a c-quark may decay into a s or d-quark. Furthermore, heavy-flavours can decay to other lighter hadrons or to leptons. In this study the production of heavy flavours is measured via the single muon decay channel.

The measurements carried out in this work are described in details in the following chapters.

CHAPTER 3

EXPERIMENTAL SETUP

In the study, data collected by the ALICE detector is used. ALICE is one of 4 major experiments located on the CERN LHC ring [CER08]. Thus, this chapter will focus on the experimental aspects, which include a brief introduction to the LHC, the description of the apparatus, online data taking, run conditions and offline framework.

3.1 The Large Hadron Collider

The Large Hadron Collider (LHC) [CER08], shown in Figure 3.1, is the world's largest and highest energy particle accelerator, located 100 m (300 ft) underground in a 27-km circumference tunnel, passing through Switzerland and France. The LHC has been designed to collide protons with protons, protons with heavy ions and heavy ions with heavy ions, primarily lead (Pb). The LHC uses some of the most powerful (superconducting) magnets and radio-frequency cavities in existence, for accelerating and focusing the beams, also for cooling down the system after the collision. The size of the tunnel, magnets, cavities and other essential elements of the machine represent the main constraints that determine the design nominal energy of 7 TeV per proton beam, making the total energy to be 14 TeV when the beams collide. The advantage of a collider over other kinds of accelerators is that when two beams collide, the energy of the collision is the sum of the energies of the two beams, $E = E_{beam_1} + E_{beam_2}$, commonly referred to as ($\sqrt{s}$ - centre-of-mass energy). A beam of the same energy that hits a fixed target would produce a collision of much less energy $E = \sqrt{E}_{beam_1}$. At the LHC, beams are brought to collisions at four interaction points, where the four large experiments ALICE [Col08a], ATLAS [Col08c], CMS [Col08d] and LHCb [Col08e] are located, see (Figure 3.1).

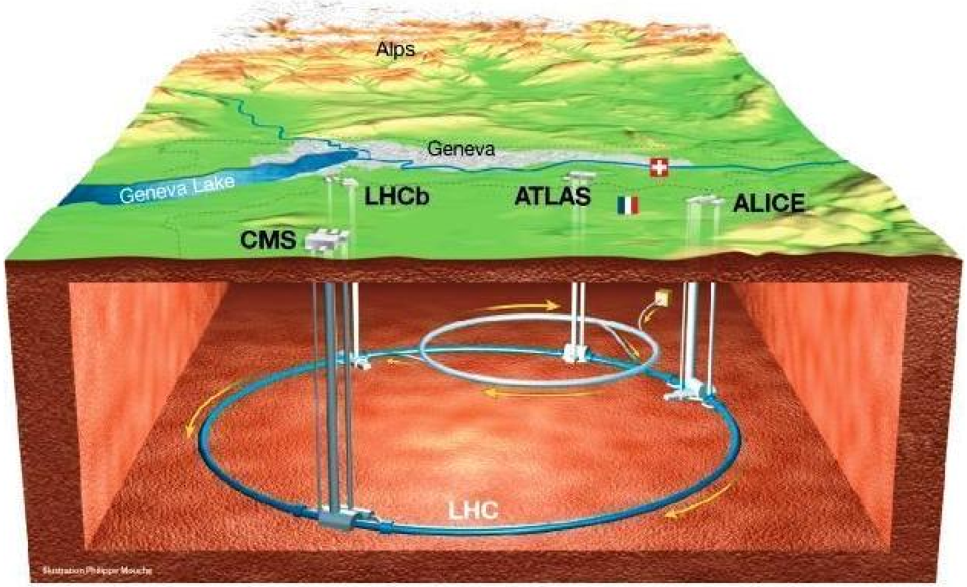

Figure 3.1: Overall view of the Large Hadron Collider [Mou14].

The LHC is supplied with protons and Pb ions from a complex system of accelerators represented in Figure 3.2. Each machine boosts the energy of a beam of particles before injecting the beam into the next machine in the sequence. The proton source is a tank of hydrogen gas, from which the hydrogen is passed through an electric field to strip off its electrons, leaving only protons to enter the accelerator. Linear Accelerator 2 (Linac 2), the first accelerator in the chain, accelerates protons to the energy of 50 MeV. The beam is then injected into the Proton Synchrotron Booster (PSB), which accelerates protons to 1.4 GeV, followed by the Proton Synchrotron (PS), which pushes the beam to 25 GeV. Protons are then sent to the Super Proton Synchrotron (SPS), where they are accelerated to 450 GeV in energy. The protons are finally transferred to the two beam pipes of the LHC, where up to now, each beam has been accelerated to nominal energy up to 6.5 TeV , i. e, centre-of-mass energy of 13 TeV. Lead ions for the LHC start from a source of vaporized lead and enter the Linear Accelerator 3 (Linac 3) before being collected and accelerated in the Low Energy Ion Ring (LEIR). They then follow the same route as protons and are eventually accelerated to a maximum of 5.02 TeV centre-of-mass energy, up to now.

At the LHC, proton-proton (pp), lead-lead ($PbPb$) and proton-lead (pPb/Pbp) are collided at each interaction point (IP) where the 4 major experiments mentioned above are located. In the following, we focus our attention on the ALICE detector located at interaction point 2 (IP2). The detector is described in details below.

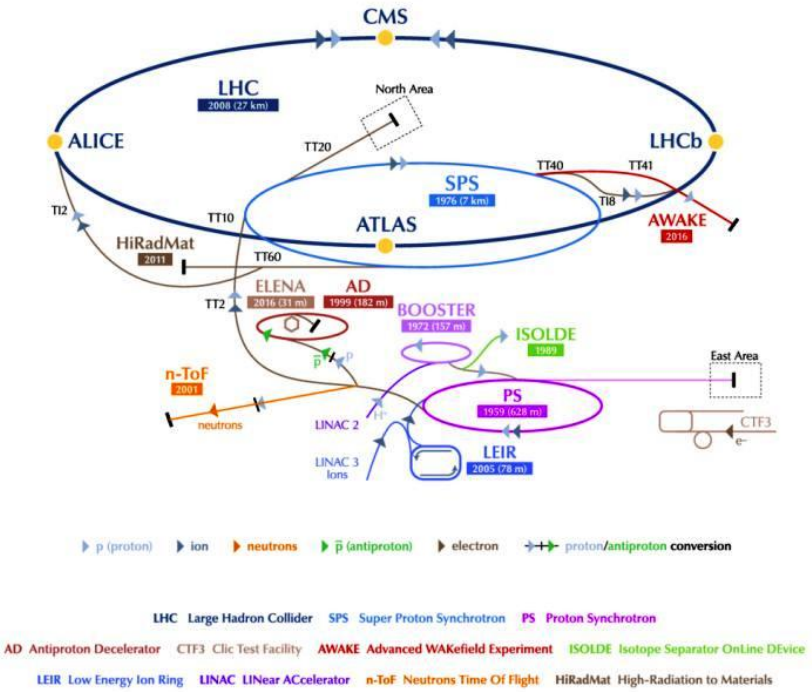

Figure 3.2: The CERN Accelerator Complex [DM16].

3.2 The ALICE experiment

ALICE stands for A Large Ion Collider Experiment [Col08a]. The detector's inclusive dimensions are $16\times16\times26\ m^3$ and has a total weight of about 1000 tons. ALICE is a heavy ion detector on the LHC ring, designed to study the properties of the strongly-interacting QCD matter known as the Quark Gluon Plasma (QGP), formed by colliding heavy ions (e.g, Pb ions) at ultra-relativistic energies. ALICE also studies pp collisions both as a comparison with $PbPb$ and pPb collisions, and in physics areas where ALICE is competitive with other LHC exper-

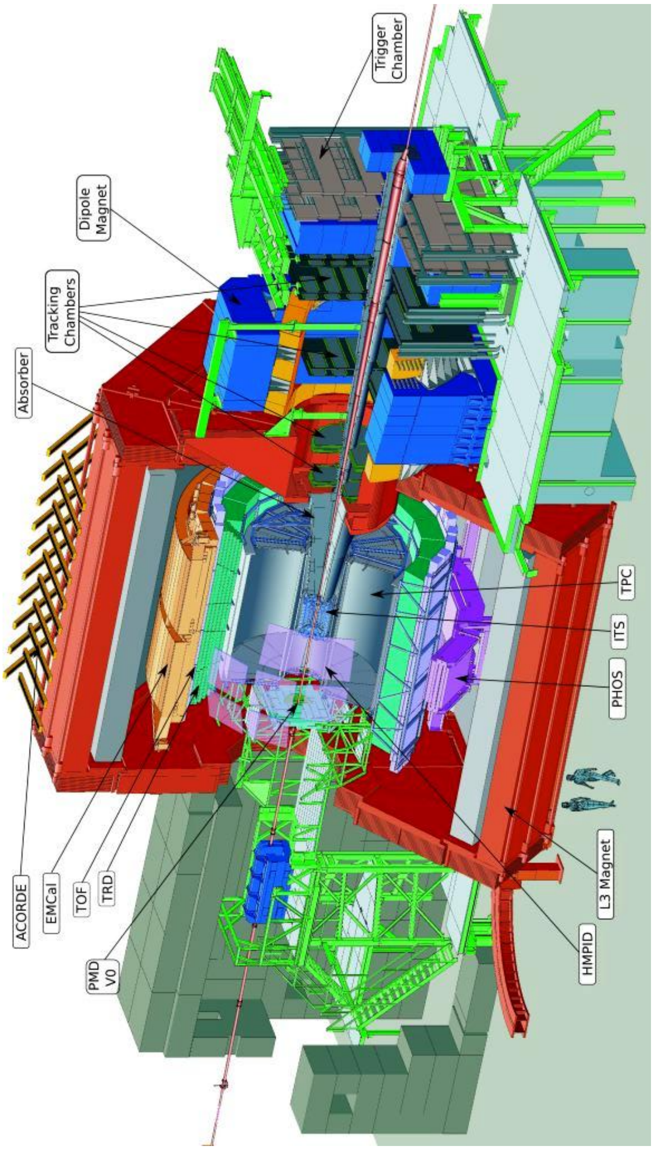

Figure 3.3: Layout of the ALICE detector [StAc13].

iments. Physicists are studying the QGP because they want to understand QCD - the theory of strong interactions, as well as deconfinement in the Standard Model. The make-up of the ALICE detector is shown in Figure 3.3. The detector is made up of three parts, namely: the central barrel detectors, the global detectors and the forward muon spectrometer. The central barrel covers the pseudo-rapidity $-0.9 < \eta < 0.9$ and this is where hadrons, electrons and photons are measured. The central barrel is provided a magnetic field of 0.5 T by the L3 solenoid magnet. The muon spectrometer is located in the forward pseudo-rapidity region ($-4 < \eta < -2.5$).

3.2.1 The ALICE coordinate system

The ALICE co-ordinate system is depicted in Figure 3.4. The IP is where the particles collide at the origin of the right handed cartesian co-ordinate system. From the IP, the z-axis is along the beam pipe, the x-axis perpendicular to the mean beam direction points to the centre of the LHC, y-axis perpendicular to the x-axis and the mean local beam direction, φ is the angle around the beam axis and θ indicates the angle from the beam axis. The ATLAS [Col08c] and CMS [Col08d] experiments are located on the *A* and *C* side, respectively.

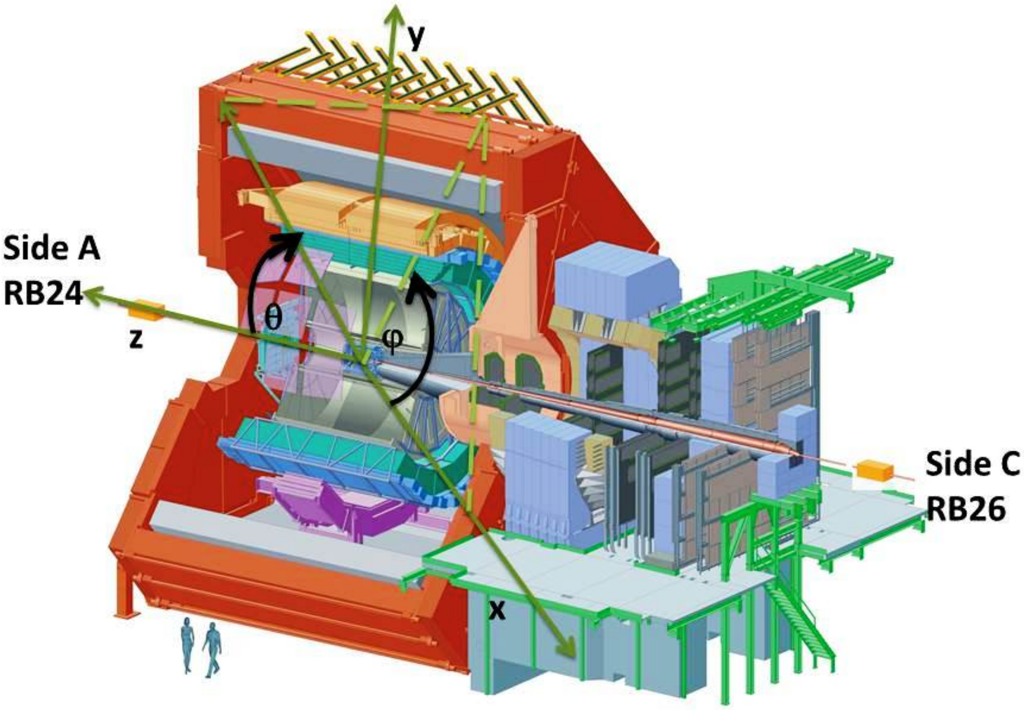

Figure 3.4: The ALICE coordinate system. [Bet03].

3.2.2 Inner Tracking System (ITS)

The ITS in Figure 3.5 consists of six cylindrical layers of silicon detectors, with a radius varying from 4 to 44 cm. Pixel, drift and strip detectors have been chosen for the two inner-most, the two intermediate and the two outer layers, respectively. The high resolution pixel detectors have extended polar-angle coverage ($\eta < 1.98$) to provide, together with the forward detectors, a continuous coverage in rapidity for charged particles multiplicity. The six layers operate, together with the central detectors, at low frequency (about 100 Hz), while the Silicon Pixel Detector (SPD) can run at higher rate (about 1 kHz) to provide the vertex information for events triggered by the Forward Muon Spectrometer. The ITS is designed to localize the primary vertex with a resolution better than 100 μm, reconstruct the secondary vertices from the decay of hyperons[1], as well as D (charm) and B (bottom) mesons, track and identify low momentum particles ($p < 100\ MeV/c$) and to complete and improve the information provided by the Time Projection Chamber (TPC). The ITS is divided into 3 subsystems; the two inner layers constitute the Silicon Pixel Detector (SPD), the two middle layers are named the Silicon Drift Detector (SDD) and finally the two outermost layers are the Silicon Strip Detector (SSD) [Col08a].

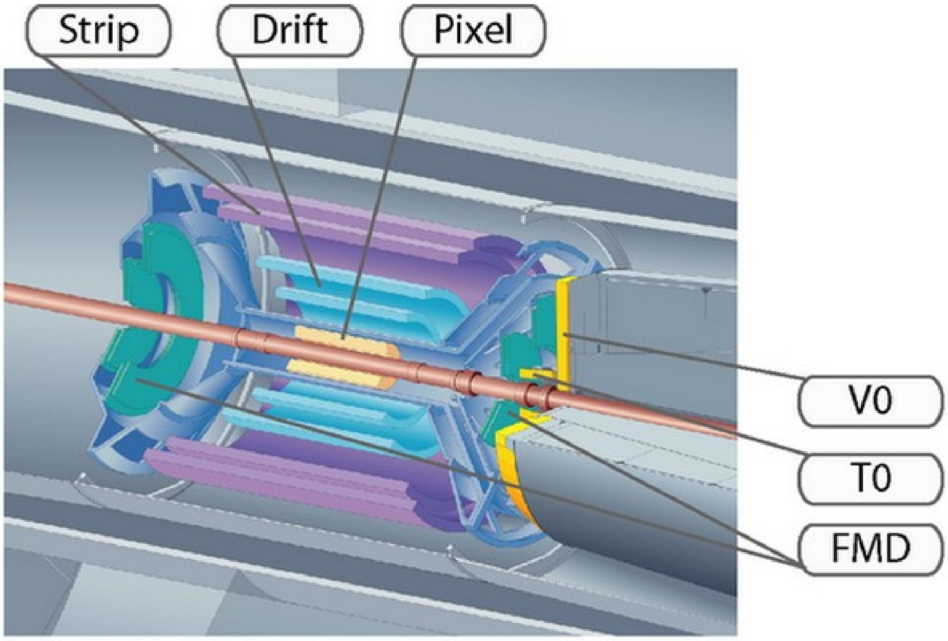

Figure 3.5: The ALICE ITS [Man12].

---

[1] hyperon is generally used for a baryon containing one or more strange (s) quarks

Silicon Pixel Detector (SPD)

The SPD layers are based on hybrid silicon pixels, consisting of sillicon detector diodes with a thickness of 200 μm. When a charged particle traverse a pixel, a digital signal is read out from that pixel. The SPD does not retain any information on the energy deposition. Thus, SPD signal is binary; either there is a hit or there is not. The signals in the two SPD layers are sufficient to form so-called tracklets [2], which can be used to measure the charged particle multiplicity in $\eta < 2.1$. Due to extreme fine segmentation of the SPD, only an occupancy of around 1 % is expected, making it extremely capable of multiplicity measurements.

Silicon Drift Detector (SDD)

The SDD works as a drift chamber, where the charged particles ionise the gas when traversing the SDD volume. The created electron drifts towards the readout, due to an electric field over the SDD. The coordinates of the particle are then directly correlated to the drift time.

Silicon Strip Detector (SSD)

The SSD utilises the energy loss from charged particles traversing strips of silicon. The SSD is capable of delivering good tracking, together with energy loss measurements. At larger distances from the interaction point (where the particle density can be lower than one track per cm^2. The double-sided microstrip detectors also allow for dE/dx[3] measurements and delivers important information for the connection of tracks from the TPC and ITS.

3.2.3 Time Projection Chamber (TPC)

The TPC is the main tracking detector of the central barrel and is optimized to provide, together with the other central-barrel detectors, charged-particle momentum measurements with good two-track separation, particle identification, and vertex determination. The phase space covered by the TPC in pseudo-rapidity is $\eta < 0.9$ for tracks with full radial track length; for reduced track length (at reduced momentum resolution), an acceptance of up to about

---

[2] Reconstruted space points in the two layers of the SPD

[3] Mean energy loss per flight path

$\eta < 1.5$ is accessible. The TPC covers the full azimuth (with the exception of the dead zones). A large p_T range is covered from low p_T of about $0.1 GeV/c$ up to $100 GeV/c$ with good momentum resolution. The TPC has a cylindrical shape; the active volume has an inner radius of about $85 cm$, an outer radius of about 250 cm, and an overall length along the beam direction of $500 cm$. The detector is made of a cylindrical field cage, filled with $90 m^3$ of Ne/ CO_2/N_2 (90/10/5), in which the primary electrons are transported over a distance of up to 2.5m on either side of the central electrode to the end plates. Multi-wire proportional, 62 chambers with cathode pad readout are mounted into 18 trapezoidal sectors at each end plate. Charged-particle tracks are reconstructed and identified with up to 159 3-dimensional space points. The TPC also provides particle identification capabilities through the measurement of the specific energy deposition dE/dx, with up to 159 samples. Using cosmic-ray muons and data taken in pp collisions, the relative dE/dx resolution was measured to be about 5.5% for tracks that cross the entire detector.

3.2.4 Transition Radiation Detector (TRD)

The Transition Radiation Detector (TRD), located radially right outside the TPC, relies on the phenomenon of transition radiation for particle identification. Transition radiation occurs when a particle crosses the boundary between two materials with different dielectric constants. The emitted radiation is linearly dependent on the γ factor[4] of the particle, thereby making it very useful at distinguishing pions and electrons at high momenta. The TRD is built up from six layers, each containing a radiator, drift chamber and read out electronics. The radiator material is responsible for creating the transition radiation photons, which are then converted in the drift chamber to electrons, being detected in the read out electronics. The information of the six layers is then combined into tracklets, which are used to identify high momentum electrons. This is used as a trigger to enhance the recorded yield of Υ's and high p_T J/Psi (J/ψ) particles. The TRD does not have full azimuthal coverage. This is a design decision in order for the HMPID and PHOS detectors (both discussed in following paragraphs), to also have areas without too much material in front of them.

---

[4] Lorentz term which defines time, length, and relativistic mass change for an object while that object is moving

3.2.5 Time of Flight (TOF)

The Time Of Flight (TOF) detector is placed just outside the TRD, and measures the flight time of particles going from the interaction point through the TOF. The momentum information, p, and the length of the trajectory, l, of the particle is known from the tracking in the ITS, TPC, and TRD. This is used together with the flight time, t, to determine the particle mass, m. The TOF consists of Multigap Resistive Plate Chambers, which are stacks of very thin structures, featuring a gas volume with a uniform high electric field. When a particle traverses the gas it immediately loses energy triggering an avalanche, which is detected at the anode of the detector. As with the TRD, the TOF does not have full azimuthal coverage, due to a desire to minimise the material in front of HMPID and PHOS.

3.2.6 High Momentum Particle Identification (HMPID)

The High Momentum Particle Identification Detector (HMPID) is a Ring Imaging Cherenkov detector (RICH), which identifies high momentum particles. It consists of a layer of radiator material, and a Multi-Wire Proportionality Chamber behind to detect Cherenkov radiation. Any particle traversing a medium with a speed higher than the speed of light in that medium, will emit Cherenkov radiation. The radiation is emitted as a shock wave at an angle with respect to the track of the particle, defined by the speed of the particle. This Cherenkov angle, θ. The emitted Cherenkov radiation is read out as a ring on the read-out plane. The ring radius is used to determine the velocity of the particle. This information is then used together with momentum information from for instance the TPC, to determine the mass of the particle.

3.2.7 Photon Spectrometer (PHOS)

The PHOton Spectrometer (PHOS) is an electromagnetic calorimeter, composed of lead-tungsten crystals. It is located in the bottom part of ALICE outside the TOF. Charged particles are rejected by multi-wire proportional chambers in front of the PHOS. The PHOS detects photons, pion (π^0), and The charmed eta (η) mesons. The measurements are used for analysing the initial temperature of the colliding system through direct single photons and/or di-photons, as well as probing deconfinement through jet quenching (the jet quenching phenomenon is explained in [Wie10]) of high p_T π^0's and investigating signals of restoration of chiral symmetry.

3.2.8 Electromagnetic Calorimeter (EMCal)

The EMCal improves jet quenching measurements and the jet energy resolution. It is also capable of measuring high-p_T photons, neutral hadrons and electrons. In addition, it allows for a fast trigger on high-energy jets. The EMCal has been designed as a layered Pb-scintillator sampling calorimeter.

3.2.9 Photon Multiplicity Detector (PMD)

The Distribution of Photons in the forward pseudo-rapidity region of $2.3 \leqslant \eta \leqslant 3.7$ is measured by the PMD. These measurements also provide estimations of transverse electromagnetic energy and the reaction plane on an event-by-event basis. The measurement of photon multiplicity gives important information in terms of limiting fragmentation, order of phase transition, the equation of state of matter and the formation of disoriented chiral condensates. The PMD consists of two high granularity gas proportional chambers, with a three radiation length converter in-between. The granularity of the PMD was optimised given the requirements of low occupancy, and high efficiency and purity of photon detection, on an event-by-event basis, at the maximum predicted charge particle multiplicity density ($\mathrm{dNch}/\mathrm{d}\eta = 8000$).

3.2.10 Foward Multiplicity Detector (FMD)

The FMD provides charged-particle multiplicity information in the pseudo-rapidity range $-3.4 < \eta < -1.7$ and $1.7 < \eta < 5.0$. The overlap between the FMD and the ITS layer provides redundancy and cross-checks of measurements between subdetectors and ensures continuous coverage for a distribution of vertices along the $z-axis$. High radial detector segmentation allows for the study of multiplicity fluctuations on an event-by-event basis, while azimuthal segmentation allows for the determination of the reaction plane for each event and the analysis of flow within the $FMD\prime$s pseudo-rapidity coverage.

3.2.11 TZERO (T0) detector

The T0 detector is designed to determine the collision time with high precision and to determine the collision vertex. $T0$ consists of two units, one on each side of the interaction point. It is the coincidence between signals in both sides that is used for both vertex and time determination. It covers the pseudorapidity range of $-3.28 < \eta < -2.97$ and $4.61 < \eta < 4.92$ on the A and C side of ALICE respectively. In 2012 during data taking the $T0$ detector was used to measure the number of particles produced in the collision and their spatial distribution together with the $V0$.

3.2.12 VZERO (V0) detector

The $V0$ detector covers a pseudo-rapidity range of $-3.7 < \eta < -1.7$ and $2.8 < \eta < 5.1$ on the A and C side of ALICE respectively. It is a triggering detector, i.e. it triggers after a certain amount of energy has been deposited onto it. This is related to the centrality of the collision. $V0$ measures the number of particles produced in the collision (interaction rate) and their spatial distribution. It also provides a background rejection capability for the muon spectrometer and rejection of beam-gas events where the energy deposited on each side of the V0 detector is not symmetric.

3.2.13 Zero Degree Calorimeter (ZDC)

The two ZDC detectors are positioned on each side of the interaction point, about 116 meters away from it. Counted as part of the ZDC system, are also two electromagnetic calorimeters (ZEM). These are placed on either side of the beam pipe, but only 7 meters away from the interaction point on the opposite side of the muon absorber. The ZDC is a hadron calorimeter made up of a very dense material, with quartz fibre going through it. The measurement is preformed by the two calorimeters, one for neutrons called ZN and another for protons called ZP. At a distance from the interaction point protons are separated well from neutrons by the magnets in the beam line. The measurement is accompanied by an electromagnetic calorimeter called ZEM.

3.2.14 The Foward Muon Spectrometer

The goal of the muon spectrometer, shown in Figure 3.6, is to study open heavy flavour, quarkonia, weak bosons and low-mass vector meson production via their muonic decay channels in a wide range of transverse momentum. The spectrometer has a total length of 17 m and covers the polar angular range $171^{\circ} \leqslant \theta \leqslant 178^{\circ}$ with respect to the ALICE reference frame. The muon spectrometer is designed to detect muons in this interval, a compromise between acceptance and detector cost, corresponds to the pseudo-rapidity range of $-4.0 < \eta < -2.5$. It is the most important detector for our study, as we are studying muons from heavy quark decays. The components of the muon spectrometer are discussed in details in the following paragraphs.

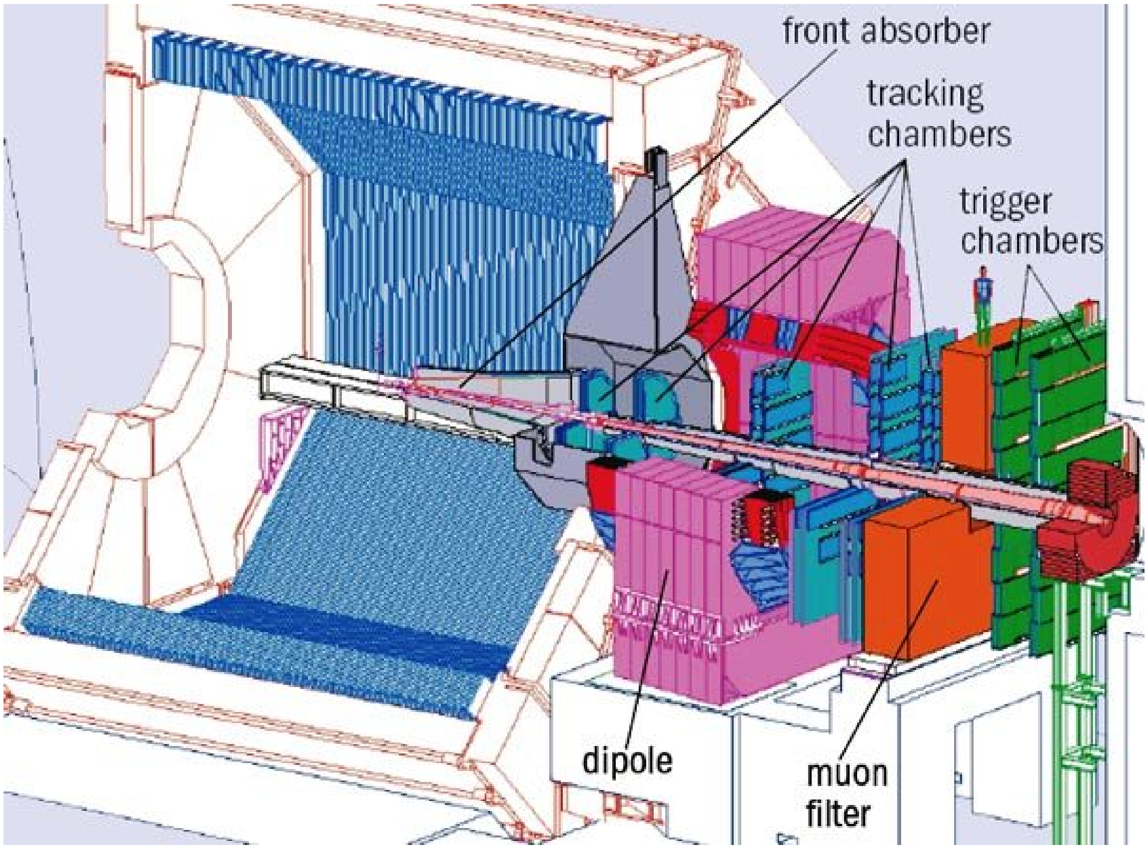

Figure 3.6: ALICE Muon Spectrometer [Col08a].

The Absorber

The front absorber shown in Figure 3.7 has the double task of attenuating the forward flux of charged particles by at least two orders of magnitude and of decreasing the background of muons from the decay of pions and kaons by limiting the free path for primary π/K. This can be achieved by minimizing the distance between the absorber and the vertex. Muons from hadronic weak decay are optimally suppressed by placing the front absorber as close as possible to the interaction point. The distance from the IP is, however, limited to 90 cm since physics performances of the ALICE central barrel should not be deteriorated by the presence of any absorber.

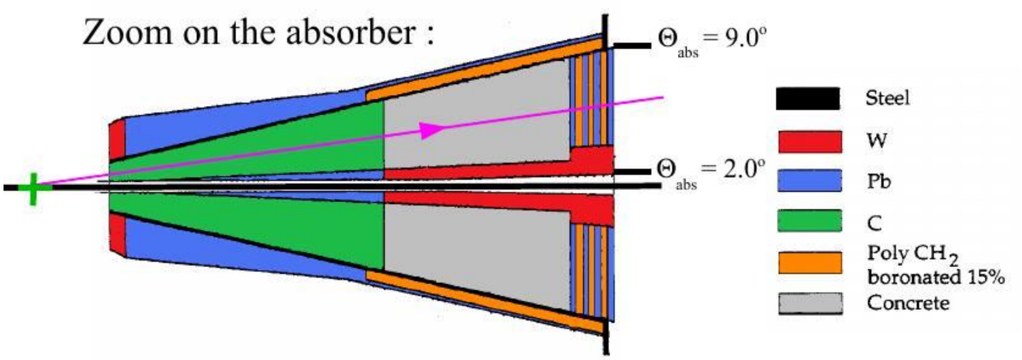

Figure 3.7: The front Absorber [Col08a].

Dipole Magnet

The muon spectrometer is equipped with a warm dipole magnet Figure 3.8 which provides a maximum central field of 0.7 T and an integral field of 3 Tm. The general concept of the magnet is based on a window frame return yoke, fabricated from low carbon steel sheets. The saddle-type excitation coils are water-cooled with demineralized water, whose inlet temperature can vary between 15 and 25 °C. Its overall dimensions are 5 m in length, 7.1 m width and 9 m height, with a total weight of about 890 tons. The dipole has an angular acceptance of $171^\circ \leqslant \theta \leqslant 178^\circ$ and is designed to provide a horizontal magnetic field perpendicular to the beam axis, whose polarity can be reverted within a short time.

Figure 3.8: ALICE dipole magnet [CER05].

The tracking system

The design of the tracking chambers shown in (Figures 3.9 and 3.10) was driven by two main constraints: to achieve the spatial resolution of 100 μm necessary for an invariant mass resolution of 100 MeV/c^2 at the upsilon (Υ) mass and to operate in a maximum hit density of about $5 \times 10^{-2}\ cm^{-2}$, the expected rate in central $PbPb$ collisions. Less stringent criteria are required for the resolution along the non-bending plane (parallel to the magnetic field), which has to be better than about 2 mm to allow efficient track finding. An additional constraint is imposed by the large area (about 100 m^2) covered by the tracking system.

They are arranged in five stations; two are placed before, one inside and two after the dipole magnet. Each station is made of two chamber planes. Each chamber has two cathode planes, which are both read out to provide two-dimensional hit information. The first station is located right behind the absorber to measure the exit points of the muons as precisely as possible. To keep the occupancy[5] at about 5%, a fine-granularity segmentation of the readout pads is needed.

Multiple scattering of the muons in the chamber is minimized by using composite material, such as carbon fibres, resulting in a thickness of about $0.03X_0$. Although based on

---

[5] the number of particles traversing a detector cell per event

standard Multi-Wire Proportional Chamber (MWPC) design, the individual chambers have been adapted to meet the particular constraints on the different tracking stations. For the stations, slat architecture was chosen .The slats and quadrants overlap to avoid dead zones in the detector.

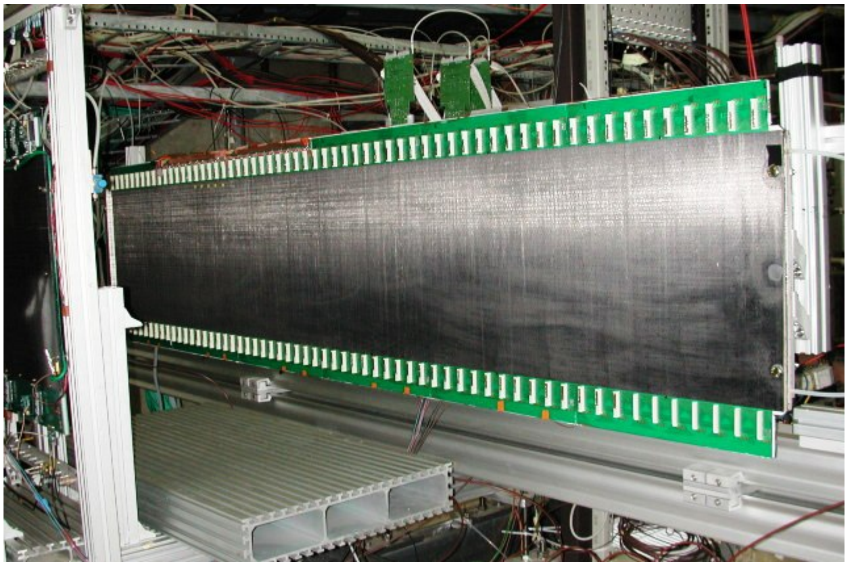

Figure 3.9: An example of the tracking chamber slat of the Muon Spectrometer [Cic02].

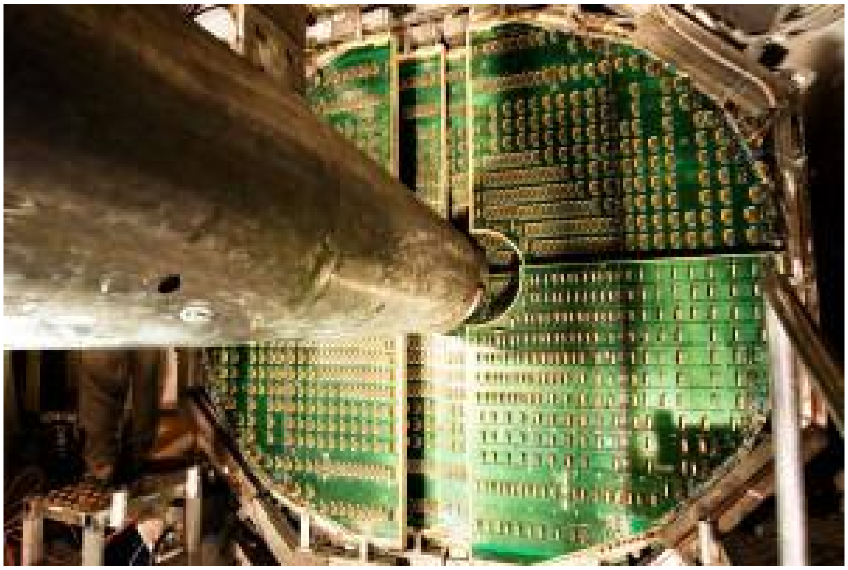

Figure 3.10: The small chambers [Mul08].

The Trigger system

The trigger system of the ALICE Muon Spectrometer consists of two trigger stations (MT1 and MT2) located at about 16 m from the interaction point and 1 m apart from each other, placed behind the iron muon filter. Each station is constituted by two planes of 18 Resistive Plate Chambers (RPCs) (schematic representation shown in Figure 3.11) that are large area detectors, made up of high resistivity ($4 \times 10^7 \Omega m$) bakelite electrodes separated by 2 mm wide gas gap. The surface of the bakelite foils on the gap side is painted with linseed oil, while the external surface is painted with graphite, with one layer connected to the high voltage and the other to the ground.

The signal is picked up by read-out strips connected to the Front-End Electronics (FEE), which basically consists of a leading-edge discriminator stage followed by a shaper. The strips are placed on both sides of the chambers, in order to provide a bi-dimensional information. The horizontal strips (aligned with the x axis in the ALICE reference system) measure the bending deviation due to the dipole magnetic field, while vertical strips (aligned with the y axis) measure the non-bending direction. The two layers of read-out pads are therefore called "bending" and "non-bending" planes respectively.

The signals coming from the FEE, consisting in the x and y fired strip patterns of the four detection planes, are sent to the local trigger electronics. The whole system is divided in 234 detection areas, each of them associated with a local trigger board. The local board density reflects the strip segmentation which is finer in the region close to the beam pipe, where a higher particle multiplicity is expected. In particular, moving from the beam pipe outwards, the strip pitch is about 1, 2 and 4 cm in the bending plane and about 2 and 4 cm in the non-bending plane. The main aims of the local electronics are to perform the local trigger algorithm and deliver the trigger decision on single tracks, and to backup strip patterns and trigger decision in a pipeline memory which is read-out on occurrence of an ALICE trigger sequence.

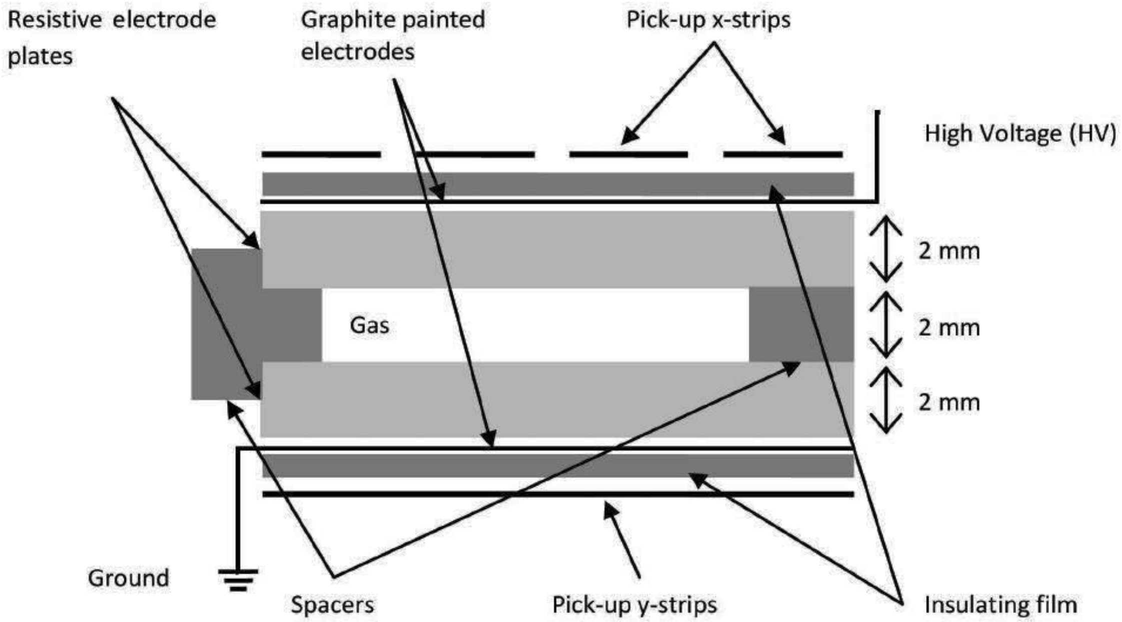

Figure 3.11: Schematic illustration of the resistive plate chamber. [Col08a].

3.2.15 Geometry monitoring system.

The alignment of the spectrometer tracking chambers is very important for achieving the required invariant-mass resolution of 100 MeV/c^2 at the Υ mass. Runs without magnetic field are carried out at the beginning of each data taking period in order to align the ten tracking chambers with straight muon tracks; as a result, determining the initial geometry of the system. Displacements and deformations of the tracking chambers with respect to the initial geometry (due to different reasons, including switching on the magnetic field) are measured and recorded during data taking by the Geometry Monitoring System (GMS). The requirement is to monitor the position of all the tracking chambers with a resolution better than 40 μm.

3.3 ALICE Online Data Taking

3.3.1 Online Framework

As shown in Figure 3.12 the ALICE analysis framework consists of the Online System which is responsible for analysis during data taking in a form of triggers. This includes five online systems: Trigger, Data Acquisition, High-Level Trigger, Detector Control System and Experiment Control System. The functions of these systems are the following:

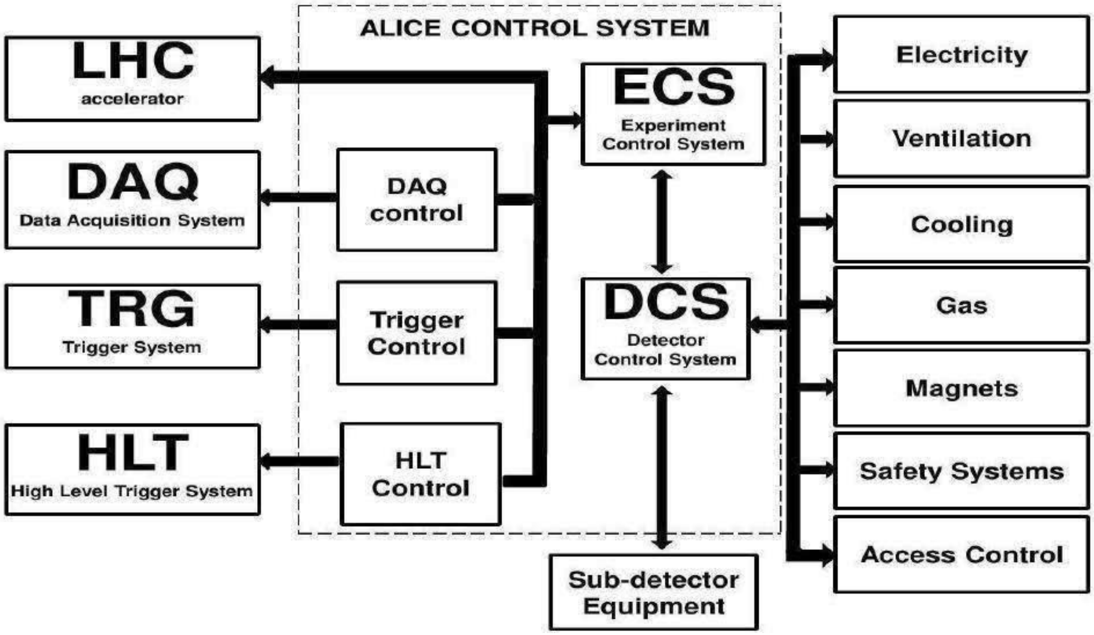

Figure 3.12: The ALICE Experiment Control System [Col04].

The Central Trigger Processor (CTP)

The ALICE CTP is designed to select events that have a variety of different features at rates which can be reduced in size to suit physics requirements and the limitation imposed by the bandwidth of the Data Acquisition (DAQ) system, and the High-Level Trigger (HLT). The challenge for the ALICE trigger is to make the best use of the component detectors, which are busy for widely different periods following a valid trigger, and to perform trigger selections in a way which is optimised for several different running modes: ion (Pb-Pb and several lighter species, pA,and pp), varying by almost two orders of magnitude in counting rate.

The ALICE trigger system is located in the experimental cavern and has a centralised layout: the CTP, the detector interface or Local Trigger Unit (LTU), and the Trigger Timing and Control partitions are all installed in adjacent racks. The trigger is divided into three levels (L0, L1 and L2). Up to 24 detectors from the ALICE experiment can be dynamically partitioned into 6 independent clusters (group of read out detectors). The LTU works as a uniform interface between the CTP and the detector readout electronics. In the standalone mode of operation, the LTU fully matches the CTP protocol.

Data-Acquisition system (DAQ)

The ALICE Data-Acquisition system (DAQ), shown in Figure 3.13, handles the data flow from the sub-detector electronics to the archiving on tape. A first layer of computers, the Local Data Concentrators (LDCs), reads out the event fragments from the optical Detector Data Links (DDLs). The DDLs are point to point links running at maximum 6Gb/s, and up to twelve of them can be connected to the same LDC. Several LDCs may be needed to collect the data from a single sub-detector. A typical data rate from the detectors to the LDCs can go above 13 GB/s.

The event fragments, aggregated in sub-events, are then transferred to a second layer of computers, the Global Data Collectors (GDCs), in charge of performing the event building. The same GDC receives all the fragments of a given event, and assembles them in a full event, which is then recorded to a Transient Data Storage (TDS) before being migrated to the Permanent Data Storage (PDS), and published via the Grid [Col12g].

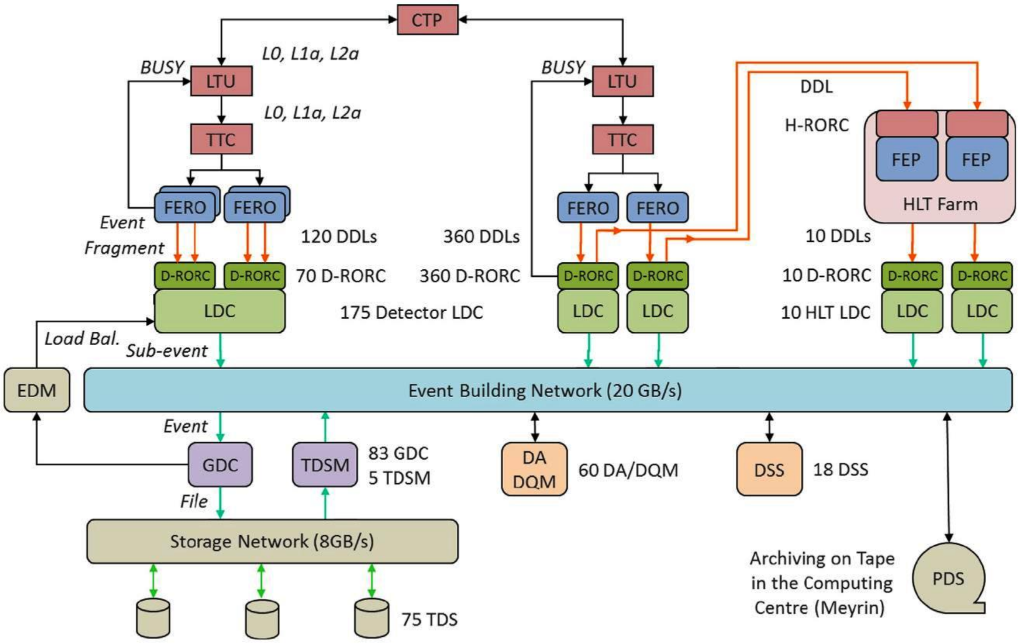

Figure 3.13: The Architecture of the ALICE DAQ and the interface of the HLT [C^{+}14].

High-Level Trigger

The High-Level Trigger, Figure 3.14, combines and processes the full information from all major detectors of ALICE in a large computer cluster. Its task is to select the relevant part of the huge amount of incoming data and to reduce the data volume, by well over one order of magnitude, in order to fit the available storage bandwidth while preserving the physics information of interest. This is achieved by a combination of different techniques which require a detailed online event reconstruction:

- Trigger: selecting interesting events based on detailed online analysis of its physics observables.
- Selection: selecting the Regions of Interests (interesting part of single events).
- Compression: reducing the event size by advanced data compression without any loss of the contained physics [Col08b].

Experiment Control System (ECS)

The Experiment Control System (ECS) coordinates the operations controlled by the ’online systems’. It permits independent concurrent activities of the experiment by different operators, and coordinates the functions of the ’online systems’ for all the detectors and within every partition[6]. The components of the ECS receive status information from the ’online systems’ and send commands to them through interfaces, based on Finite State Machines (FSM). The implementation of these interfaces is based on the SMI++ package [FG06]. The interfaces between the ECS; and the ’online systems’ contain access control mechanisms that manage the rights granted to the ECS: the ’online systems’ can either be under the control of the ECS or be operated as independent systems. In the second case, the ’online systems’ provide status information to the ECS, but do not receive commands from it [C$^+$14].

---

[6] A group of particle detectors.

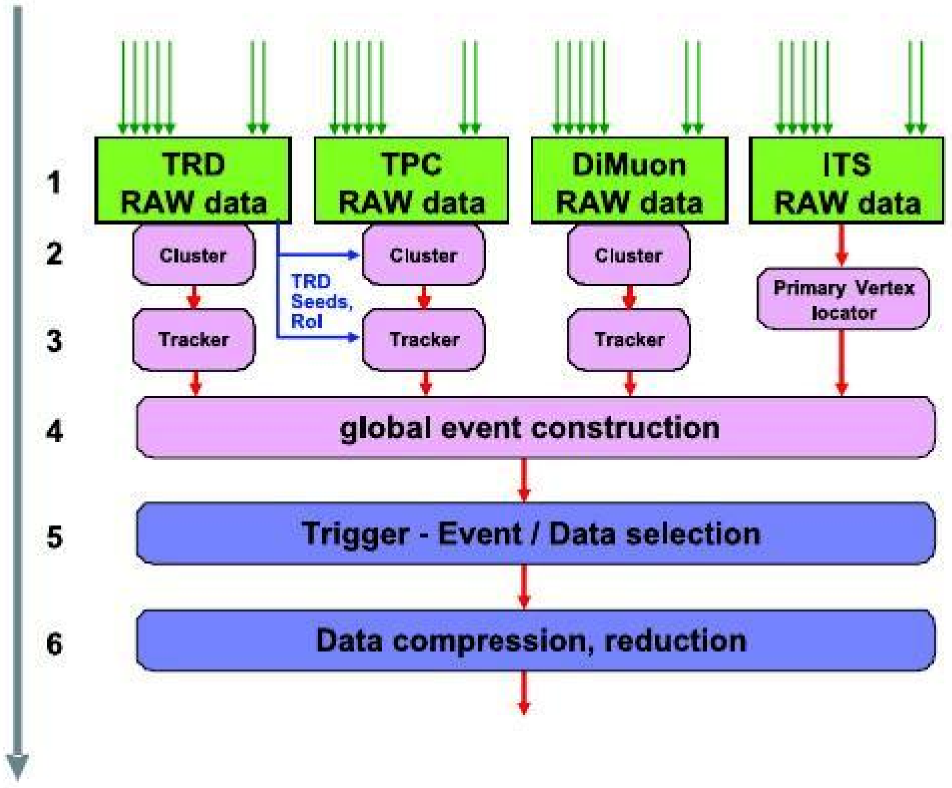

Figure 3.14: The six architectural layers of the HLT [Col08a].

Detector Control System (DCS)

The main task of the ALICE Control System is to ensure safe and correct operation of the ALICE experiment. It provides remote control and monitoring of all experimental equipment in such a way that the ALICE experiment can be operated from a single workplace, the ALICE Control Centre at the LHC Point 2 (P2), through a unique set of operator panels. The DCS monitors safety and environment variables, e.g, Tempereature, Pressure, Humidity, Radiation, RAdiation Monitoring System for the Environment and Safety (RAMSES) and magnetic Field. The system provides optimal operational conditions so that the data taken with the experiment is of the highest quality. The ALICE control system was designed to reduce the downtime of the experiment and hence contribute to a high running efficiency. It also maximises the number of channels operational at any time, and measures and stores all parameters necessary for efficient analysis of the physics data.

Figure 3.15 shows the layout of the DCS monitoring tool where information about the detector Safety Matrix (On the top right of the figure mentioned), magnets, level 3 Alarms: CERN Safety Alarms Monitor (CSAM), Detector Safety System (DSS), the ALICE Safety Permits as well as the status of the LHC mode. The different colors "green", "blue", "red", "yellow/orange" indicate the detector FSM state. The color "green" and READY state indicates that the detector is ready to take data, i.e, the high voltages (HV) are fully biased. For example, for muon chambers (MCH) the optimal HV value for the "READY" state is 1600 - 1620 Volts. The blue colour is associated with detector FSM states. During data taking both the dipole and solenoid magnets must be ON, the polarity is either positive or negative (depending on the physics of interests in that particular period) and the magnetic field is 683 Tm (6 kA) and 452 Tm (30 kA).

It is essential to have a way of communicating the LHC operations to the experiments. For any operations that the LHC partakes, it has to warn and get permissions from the experiments. In particular, this is mostly important in the case of ALICE, as the injection point for beam 1 is very close to P2 where ALICE is located. Thus, when the LHC wants to inject the beams or ramp the magnet, ALICE has to make sure that it is "safe" to do so before granting permission. This is communicated through ALICE Permits. The LHC status panel reflects the status of the beam, which is communicated to the experiments via the $handshake$. This will be discussed in detail under run conditions.

3.4 LHC conditions

Experimental run conditions are determined by LHC conditions, e.g, operation modes as well as the automatic filling scheme (AFS). Two operation modes exist for the LHC: the accelerator mode and beam mode [B$^+$14]. The accelerator mode provides a summary of the LHC machine state while the beam modes provide a description of the accelerator cycle. In its operation, the LHC follows a strict sequence to enable its transition to the next step. The following discussion will be focused on the LHC conditions.

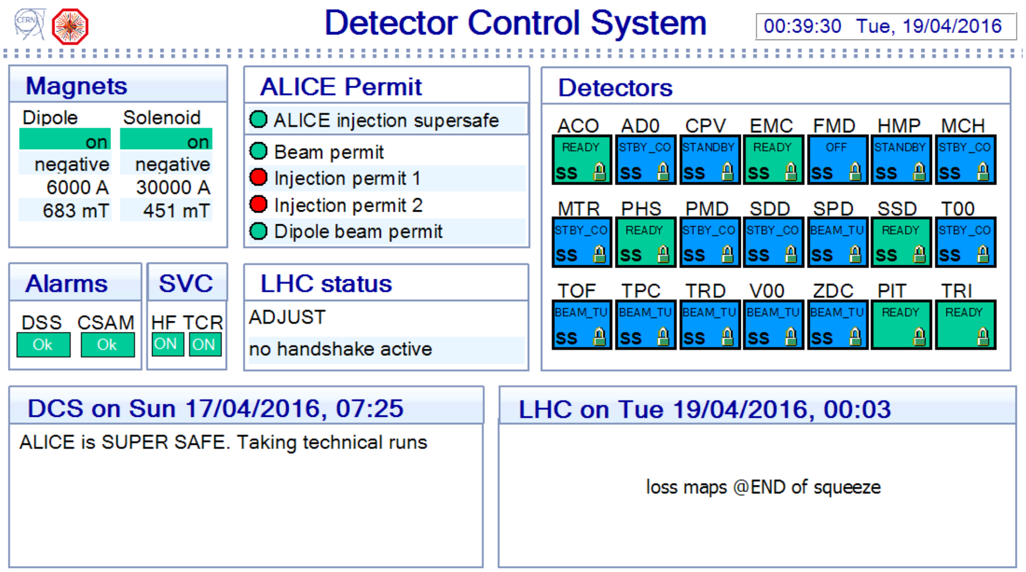

Detector Control System

00:39:30 Tue, 19/04/2016

Magnets

Dipole	Solenoid
on	on
negative	negative
6000 A	30000 A
683 mT	451 mT

ALICE Permit

- ● ALICE injection supersafe
- ● Beam permit
- ● Injection permit 1
- ● Injection permit 2
- ● Dipole beam permit

Detectors

ACO	AD0	CPV	EMC	FMD	HMP	MCH
READY SS	STBY_CO SS	STANDBY SS	READY SS	OFF SS	STANDBY SS	STBY_CO SS
MTR	**PHS**	**PMD**	**SDD**	**SPD**	**SSD**	**T00**
STBY_CO SS	READY SS	STBY_CO SS	STBY_CO SS	BEAM_TU SS	READY SS	STBY_CO SS
TOF	**TPC**	**TRD**	**V00**	**ZDC**	**PIT**	**TRI**
BEAM_TU SS	BEAM_TU SS	BEAM_TU SS	BEAM_TU SS	BEAM_TU SS	READY	READY

Alarms

DSS	CSAM
Ok	Ok

SVC

HF	TCR
ON	ON

LHC status

ADJUST

no handshake active

DCS on Sun 17/04/2016, 07:25

ALICE is SUPER SAFE. Taking technical runs

LHC on Tue 19/04/2016, 00:03

loss maps @END of squeeze

Figure 3.15: An example of the ALICE DCS monitor [Col16b].

3.4.1 LHC operations

The handshake is a way the LHC communicates it's operational activities with the experiments. The different phases of the beam are depicted in Figure 3.16 and are described briefly as follows:

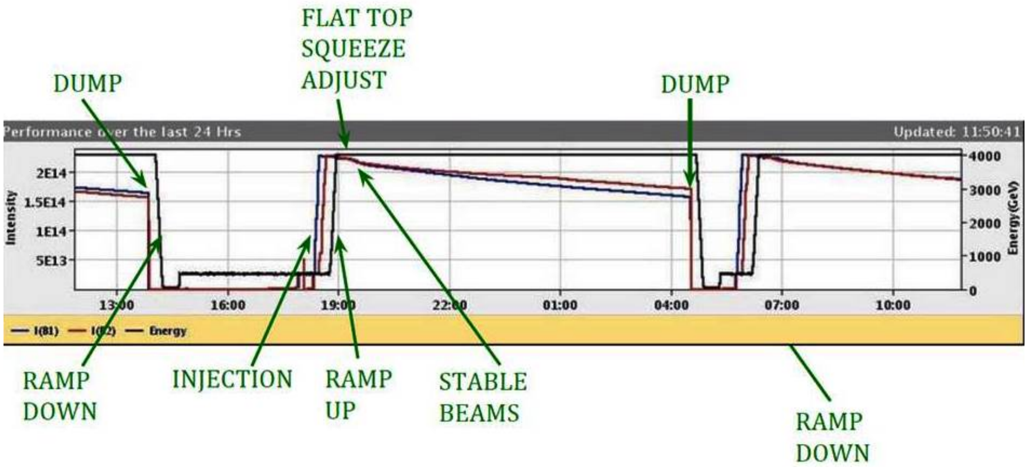

Figure 3.16: Depiction of the LHC beam modes [Lea16].

SETUP

In this mode, the beam is in the transfer lines. There is no beam in the LHC ring.

INJECTION PROBE BEAM

The beam is injected in either ring 1 or ring 2 or has a safe beam circulating. Checks are done for the different accelerator sub-systems before injecting higher intensities. The aim is to establish a circulating safe beam, with a given life time.

INJECTION SETUP BEAM

During the INJECTION PROBE BEAM, measurements are made with very limited precision. In order to make more precise measurements before filling for physics, a SETUP BEAM is used. This beam is the representative of the physics beam to follow, just with fewer bunches to stay below the damage threshold.

INJECTION PHYSICS BEAM

This is the stage where the LHC machine has been optimized and has a circulating beam with a suitable lifetime and it is ready to accept higher intensities needed for physics. When this mode is reached, a pilot beam is injected, since the accelerator will be empty.

PREPARE RAMP AND RAMP

When injection is complete the LHC machine prepares for energy ramping.

FLAT TOP

When energy ramp is finished. Pre-squeeze checks are done. Calibration runs are performed in preparation for data taking. At this stage the ALICE CTP clock should be synchronized with the LHC clock. This ensures that the optimal energy reached can be maintained consistently for the required period of the collisions. For example, at this point the Muon Chambers (MCH) take a pedestal run - noise calibrations for the FEE, which is done at HV equal to or below 1200 V.

SQUEEZE AND ADJUST

In the SQUEEZE mode, the beams are focused by adjusting the emittance[7] to ensure collisions, which raises the intensity of the beam.

After the SQUEEZE mode, the path of the beam is adjusted; this is done by focusing the two beams to enable collisions (ADJUST).

STABLE BEAMS

Stable conditions with collisions in the experiments, which means that backgrounds and life time is under control. Small adjustment of beam parameters are permitted. In case of slow degradation all the experiments are warned and the ADJUST mode is entered when all the experiments have confirmed they are ready.

UNSTABLE BEAMS

Emergency mode entered from stable beams in case of sudden beam degradation. The UNSTABLE BEAMS mode may be entered without prior warning to the experiments. UNSTABLE BEAMS mode can be entered from ADJUST only if the accelerator mode is MD. This transition has been requested for Roman Pots calibration or special machine protection tests. In this case, a special key has to be turned in the control room of the experiment to disable, temporarily, the protection interlock, and has to be put back in position after the tests are finished.

3.4.2 LHC Automatic Filling Scheme (AFS)

Each period of data taking has a separate bunch [8] filling scheme [9] which depends on the luminosity[10] and the cross section required for the physics of interest for each experiment.

---

[7] the smallest opening you can squeeze the beam through. Increasing the energy of the beam reduces the emittance

[8] A beam of squeezed groups of particles, in this case protons

[9] Trains of proton bunches injected at regular intervals into the LHC ring.

[10] The ratio of the number of events detected (N) in a certain time (t) to the interaction cross-section (σ). It is given by $L = \frac{1}{\sigma}\frac{dN}{dt}$.

Bunch filling schemes allow the tuning of the luminosity to meet the requirements of experiments. Several LHC filling patterns exist [COL03]. Of these only a certain number are considered as "baseline" filling schemes, corresponding to specific LHC modes of operation. There are four filling schemes for protons and two for heavy ions. The particularities of a scheme determines the number of bunches in each LHC ring. For each scheme the characteristic of a bunch, e.g. intensity and emittance are varied based on the limits imposed by the the LHC and it's injector chains. For the purpose of this study we constrain our discussion to those pertaining to protons.

The 25 ns filling scheme is the principal scheme for high luminosity operation. The beam is arranged in the form of 39 batches of 72 bunches. The bunches in each batch are spaced at 25 ns. Between the batches are gaps to allow for the SPS and LHC kicker rise times. This makes a total of 2808 bunches per LHC ring. There are 3564 bunch positions separated by 25ns in the circumference of an LHC ring.

A typical filling scheme contains information about the number of bunches in the LHC ring, their position in the orbit and the number of bunches expected to collide at each interaction point, with a typical format:

<spacing> < Nb > b < IP1/5 > < IP2 > < IP8 > < code >

- < spacing > = Single, or 2025ns, or 525ns, or 75ns, or 50ns, or 25ns, etc. This refers to the characteristic bunch spacing, given in time units, in the main injector batches used for the given filling scheme. Single means that single bunches are injected into the LHC.

- < Nb > = total number of bunches per beam for the given filling scheme, (normally, identical for both beams). If a probe bunch is kept (i.e. not overinjected), it is not counted in the total number. The presence of a non-overinjected probe bunch is encoded in the suffix < code >.

- < IP1/5 > = expected number of colliding bunch pairs in IP1 and IP5 for the given filling scheme. IP1 and IP5 are where ATLAS and CMS detectors are located in the LHC ring respectively.

- < IP2 > = expected number of colliding bunch pairs in IP2 for the given filling scheme. IP2 is where ALICE is located.

- < IP8 > = expected number of colliding bunch pairs in IP8 for the given filling scheme. IP8 is where LHCb is located.

- < code > = a free suffix to encode variants of a filling scheme.

The experiments are interested in the bunch patterns in terms of the colliding and non-colliding proton bunches. Slowly in the period of 2010 - 2012, more and more bunches were injected in the LHC ring. In the periods of interest to this study, the filling scheme, in terms of bunches colliding at each IP, and the total number of bunches present was for example:

50ns_1374_1368_0_1262_144bpi12inj

This means that the bunches were spaced by $50ns$; there were 1374 bunches present in the LHC, 1368 collided at Points 1 and 5 (ATLAS and CMS), 1262 at the Point 8 (LHCb) and the 0 (zero) colliding bunches at Point 2 (ALICE) means that the LHC delivered what is known as main-satellite collisions in ALICE. This is because the ALICE experiment is optimized for heavy-ion collisions, therefore cannot handle instantaneous luminosities above $10^{29}\ cm^{2}\ s^{-1}$ for pp collisions [Col12b]. As shown in Figure 3.17 this is partly solved by allowing collisions between high intensity proton bunches (main bunch) and low intensity ones (satellite bunches). These collisions are called main-satellite collisions.

3.4.3 ALICE run conditions in pp collisions at 8 TeV

Experiments take physics data when the LHC announces "Stable Beams". That means the ALICE detector must be ready to collect data at this stage, which means that ALICE subsystems (FEE) must be conditioned or calibrated before-hand. In ALICE, detector calibrations are done between pre-ramp and adjust modes.

Based on the active filling scheme given above ($50ns$_1374_1368_0_1262) ALICE collected pp data in 2012 utilizing different trigger classes and clusters[11]. The trigger classes

---

[11] Group of detectors read together in the CTP.

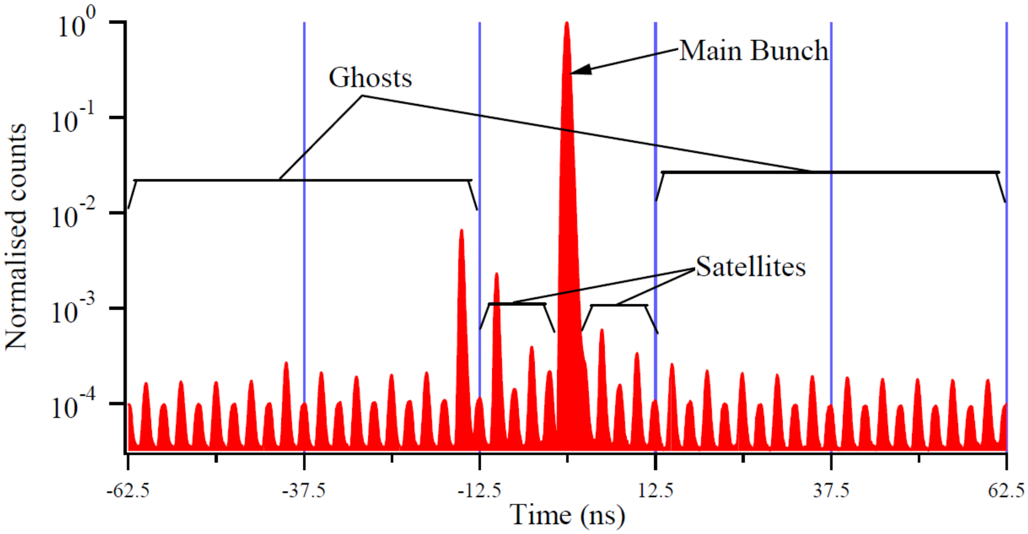

Figure 3.17: Profile showing the definition of main, satellites and ghost bunches [J+12].

describe the beam interactions for the physics of interest in that period. For this study we are interested in data samples collected during the 2012 LHC data taking period in pp collisions at 8 TeV triggered by the T0 detector, for minimum bias events and triggered by the muon trigger system, using the trigger classes:

CINT8-S-NOPF-ALLNOTRD and CMSH8-S-NOPF-MUON.

CINT8 refers to the T0 interaction trigger, that is, minimum bias (MB) trigger which is a coincidence of the T0-A and T0-C with the SPD and measures the minimum bias events. CMSH8 refers to the muon trigger for high-p_T single-muon measurement, which in addition to the T0-A and T0-C, includes the muon trigger. The p_T threshold for the two triggers is greater or equal to 1 GeV/c and 4.2 GeV/c respectively. The *S* denotes satellite collisions, NOPF means there is no-past-future-protection in the central trigger and ALLNOTRD shows the trigger cluster to be read if trigger conditions are satisfied. In ALICE the data taking conditions for pp collisions in 2012 satisfied the criteria given in Table 3.1.

3.5 Offline Framework

The primary task of the ALICE offline project, illustrated schematically in Figure 3.18, is to reconstruct and analyze data coming from real or simulated data. This can be done by

Table 3.1: Data taking conditions for pp collisions in 2012.

Beam Type	pp
Beam Mode	STABLE BEAMS
Beam Energy	4 TeV
Beta Star	3 m
Interacting bunches	0
L3 Magnet Current	-30 kA
Dipole Magnet Current	-6 kA
Partition	Physics

means of a program based on the object oriented techniques on a software called AliROOT. This software environment was developed in 1998, and it is based on the ROOT framework.

ROOT is a modular scientific software framework. It provides all the functionalities needed to deal with big data processing, statistical analysis, visualisation and storage. It is mainly written in C++ with other languages such as Python [BR97].

3.5.1 Simulation Framework

The main task of the Simulation Framework shown in Figure 3.19 is to provide flexible infrastructure and tools for the development, validation and usage of Monte Carlo simulation applications. The aim is to facilitate interaction between experiments and simulation toolkits developers and for eliminating duplication of work and divergence. The simulation consists of several work packages addressing particular areas of detector simulation, such as the geometry description exhange mechanisms, geometry persistency, Python interfacing, Monte Carlo truth handling, as well as generalized interface to different simulation toolkits for application physics validation studies [RES05b].

Particle transport

When particles are propagated through the detector material, they can interact with matter, decay and create additional particles. These new particles have to be propagated through the detector as well. Consequently, the total number of particles after the transport process is significantly larger than the number of particles created in the initial generation step. During this process, all interactions of particles with sensitive detector parts are recorded as hits

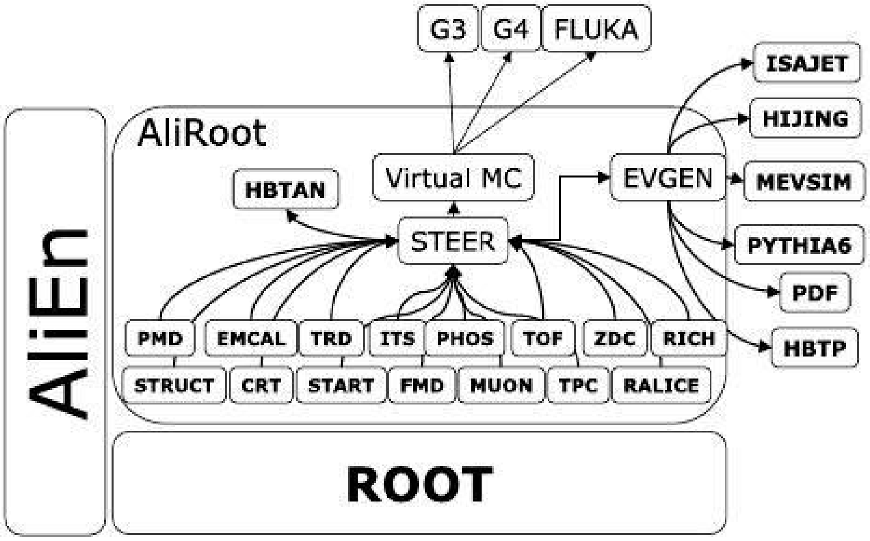

Figure 3.18: Data processing framework [Col08a].

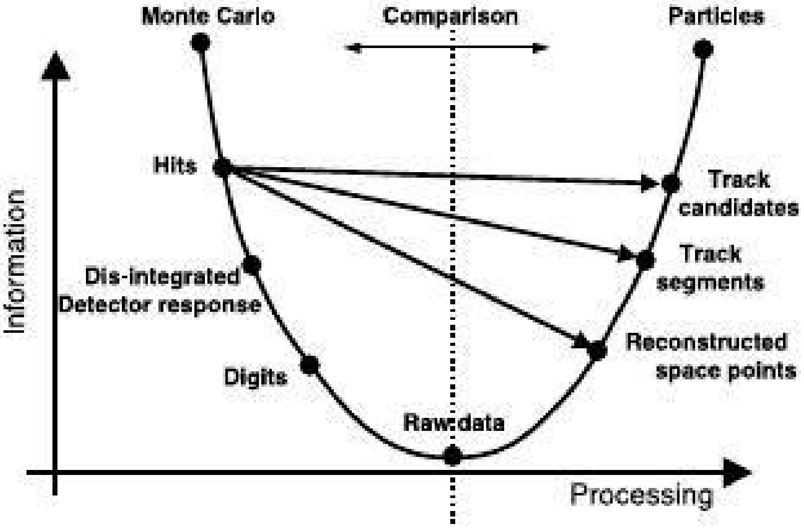

Figure 3.19: A schematic view of the AliROOT framework [Col08a].

that contain the position, time and energy deposit of the respective interaction. The track references are stored, mainly needed for the debugging of the reconstruction algorithms. Programs that perform the transportation of particles and interfaced with AliRoot [Col05] are GEANT3 [B^+87] and FLUKA [RES05a].

Digitization

If a particle produces a signal in a detector element (hit), objects are created that consist of the sum of the deposited energy by all hits, so that there is only one digit. The energy in this digit is transformed into Analogue-to-Digital Converter (ADC) amplitude units. The corresponding digital output of the detector is stored as a summable digit, taking into account the detector's response function. The electronic noise is added and digits whose energy does not pass the required energy threshold are eliminated. Summable digits allow events to be merged without duplication of electronic noise. In the last step, the data is stored in the specific hardware format of the detector (raw data). At this stage the raw data corresponds to the signals that would be produced by an interaction of the same kind within the detector.

Raw data

Raw data corresponds to the signals produced by an interaction within the detector. The subsequent reconstruction is the same for simulated and real events. It consists of the following steps.

Cluster finding

Particles that interact with the detector usually leave a signal in several adjacent detecting elements or in several time bins of the detector. At this level the signals are combined to form clusters. This permits the position or time of the traversing particle to be determined and reduces the effect of random noise. Overlapping signals from several particles in a single cluster are unfolded. This step is performed for each subdetector where, due to the different nature of the subdetectors, the implementations vary significantly.

Track reconstruction

Track reconstruction in the ALICE Muon Spectrometer, ITS, TPC and Transition Radiation Detector (TRD) is based on the Kalman filter approach. The initial approximations for the track parameters for primary particles are constructed using pairs of space points taken at two outer TPC pad rows, separated by a few pad rows and the primary vertex. The seeds for the secondary tracks are created without using the primary vertex, since such a constraint would unnecessarily reduce the strange particle decay finding efficiency. The additional space points used for these seeds are then searched along the straight line segment connecting the pairs of points taken at those two outer TPC pad rows.

Once the track seeds are created, they are sorted according to the estimate of their p_T. Then they are extended from one pad row to another in the TPC and from one layer to another in the ITS, towards the primary vertex. Every time a space point is found within a prolongation path defined by the current estimate of the covariance matrix, the track parameters and the covariance matrix are updated using the Kalman filter. For each tracking step, the estimates of the track parameters and the covariance matrix are also corrected for the mean energy loss and Coulomb multiple scattering in the traversed material. The decision on the particle mass to be used for these corrections is based on the dE/dx information given by the TPC, when available. If the information is missing or not conclusive, a pion mass is assumed. Only five particle hypotheses are considered: electrons, muons, pions, kaons and protons.

Once all the tracks are followed down to the Distance of Closest Approach (DCA) to the collision vertex, they are then propagated outwards, through the ITS, TPC and TRD. During this tracking phase, the track length and five TOF hypotheses per track (corresponding to the electron, muon, pion, kaon and proton masses) are calculated. This information is later used for the TOF PID procedure. When possible, tracks are matched with the hits reconstructed in the TOF detector and other ALICE detectors residing outside the TRD in radial direction [Bel14].

Among the track finding algorithm in single detectors, is the SPD finding. The event vertex and the tracklets are reconstructed by forming straight lines out of a cluster, in each of the two SPD layers. The event vertex is reconstructed where most of these lines intersect as shown in Figure 3.20. A tracklet is identified by drawing a line joining two hits, deposited by the charged particle on the two layers of the SPD, extrapolated to the interaction vertex, as shown in Figure 3.20. As illustrated in Figure 3.21 a tracklet is represented by (η, φ and $\Delta\varphi$), the quality parameter of the tracklet and the primary vertex position, because tracklets originate by constructing from the vertex.

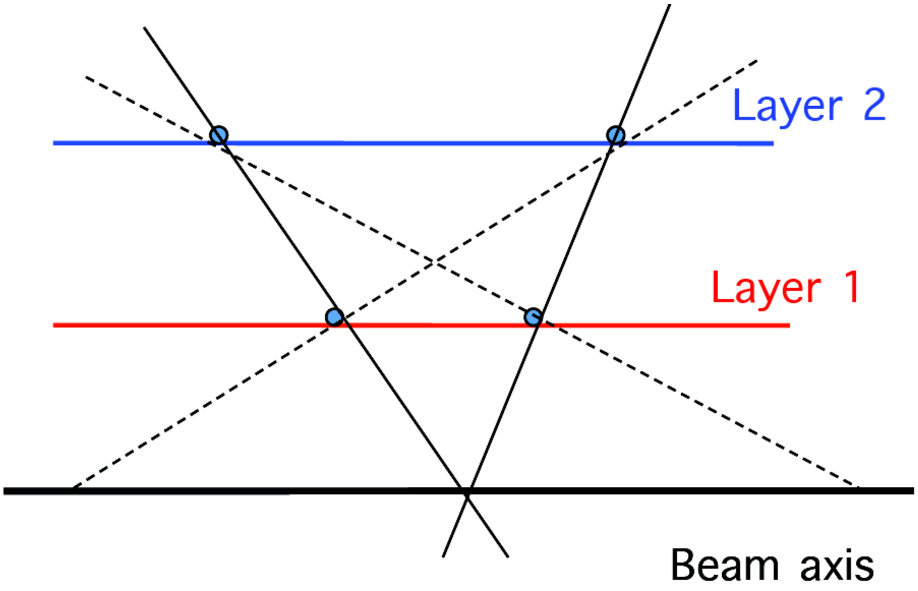

Figure 3.20: A schematic view of the vertex reconstruction [Mil10].

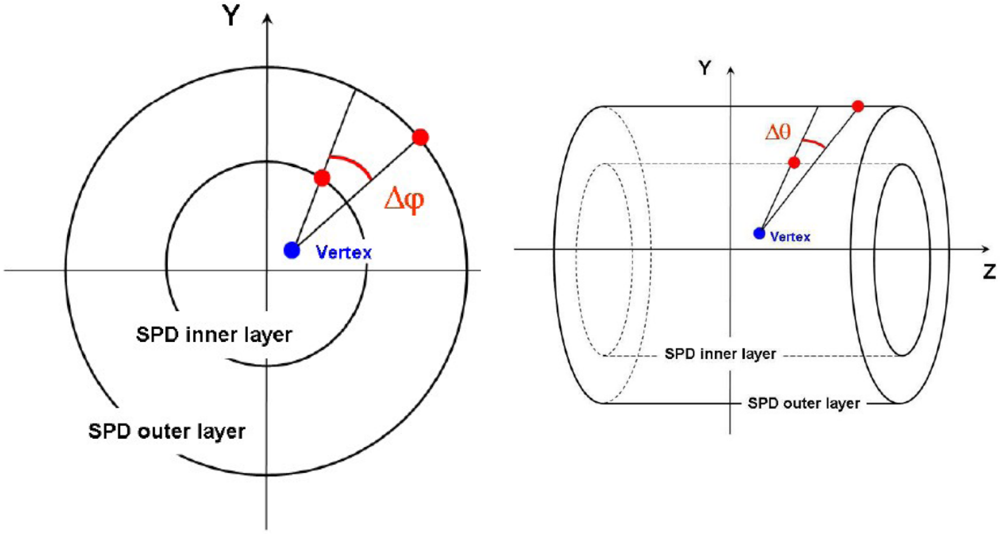

Figure 3.21: Tracklet from SPD clusters, with the primary vertex within a fiducial window in θ and ϕ [San11].

Primary and secondary vertex reconstruction

The reconstruction begins with cluster finding in all of the ALICE central detectors (ITS, TPC, TRD, TOF, HMPID and PHOS). Using the clusters reconstructed at the two pixel layers of the ITS, the position of the primary vertex is estimated and the track finding starts.

In order to reconstruct secondary vertices, the primary vertex has to be reconstructed. Primary vertex reconstruction is performed by combining the opposite-sign tracks and performing fits to determine the probability that these tracks originated from a common vertex. The reconstructed vertex with the largest total p_T is considered the primary vertex. For example, particles like pions (π^+) and protons (π^-) from the K-Short meson (K_s^0) decay, $K_s^0 \leftarrow \pi^+ + \pi^-$. If the closest approach and the topology of the two tracks is consistent with a decay, the pair is accepted as a potential secondary vertex.

The output of the reconstruction is called Event-Summary Data (ESD) and contains only high-level information, such as, the position of the event vertex, parameters of reconstructed charged particles together with their PID information, positions of secondary vertex candidates, parameters of particles reconstructed in the calorimeters and integrated signals of some subdetectors.

The data analyzed in this study is based on the Analysis Object Data (AOD), produced by filtering Event Summary Data (ESD), this means the physics selection is applied. The physics selection task selects collision candidates (physics events) from data, performs an offline validation of online triggers and rejects background (beam gas) based on the content of the Event Summary Data (ESD).

3.6 ALICE Grid

ALICE data is analysed using special software. Both data and software are available on the ALICE GRID i.e. MonALISA Repository for ALICE [B+08]. Figure 3.22 gives a view of the ALICE grid structure. Access to the GRID requires a certificate which is obtained via an authorised administrator of the Virtual Organisation (VO) subscribed to ALICE. For the analysis ALICE approved software, ALIROOT [ALI11], is accessible via ALIEN (ALICE Environment) plug-in. It is based on the ROOT framework, hence it is dependent on specific versions of

ROOT and GEANT packages. The software is supported on LINUX (UBUNTU, SL) and other Open Source operating systems. In this work data was analyzed using ALIROOT.

The grid works in such a way that users send job requests from one of the many entry points into the system. A job request can be storage, processing capacity, or availability of analysis software. The grid determines the identity of the user, checks the person's identity and searches for available sites that can provide the resources requested. The ALICE computing model of the experiment is based on a multi-tier architecture shown in Figure 3.23. The Tier-0 is the computing centre at CERN, the site hosting the experiment. Its computing centre has a special role; it records all original data to permanent storage and performs the initial processing of the data to provide rapid feedback to the operation. The processed data is then sent to other computing centres for analysis. Tier-0 also provides analysis capacity for local users. The Tier-1 consists of eleven large computing centres around the world. They receive data directly from CERN and provide additional permanent storage and the computing resources for reprocessing of the data, required at a later stage in the analysis. The centres are also responsible for the collection of simulated events produced at higher Tier centres. Tier-2 consists of even a large number of computing centres (about a hundred) whose role is to provide the greater part of computing resources for simulation and analysis. Typically, they are associated with large disk storage to provide temporary storage of data that is required for analysis. A Tier-3 centre consists of a large number of smaller computing centres at various universities and laboratories, whose main role is to provide analysis capacity for local users.

Figure 3.22: A view of the ALICE Grid [Sin16].

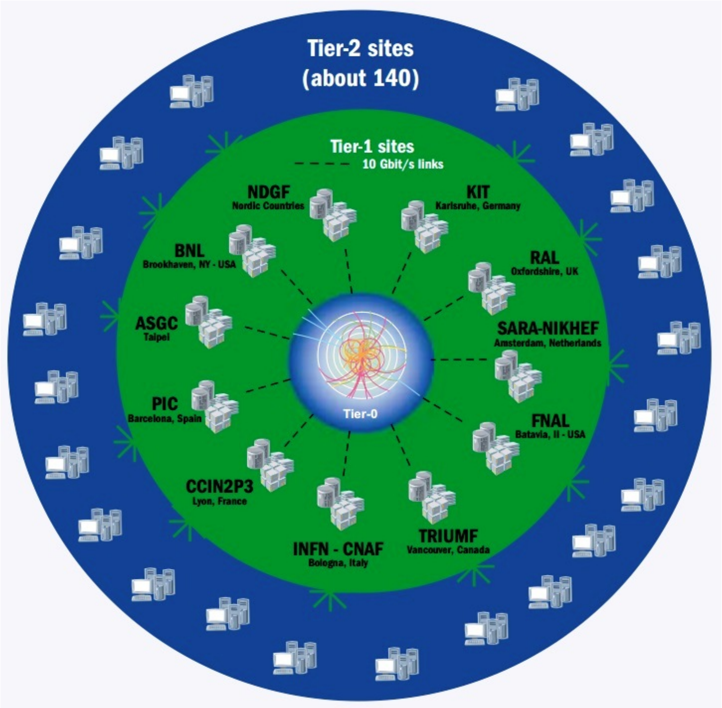

Figure 3.23: The GRID Tiers [CER15].

CHAPTER 4

DATA ANALYSIS

The aim of the analysis discussed in this chapter is to investigate the correlation of the production of single muons from heavy-flavour decays with charged-particle multiplicity. The data analyzed in this study was collected in 2012 in pp collisions at 8 TeV at the LHC. The two periods of interest are periods LHC12h and LHC12i. The data sample includes 270 runs triggered by the T0 detector, taken from muon_calo_pass2 reconstruction. Only minimum bias events (MB) as well as high p_T single muon events (CMSH) are taken into account. They correspond to an integrated luminosity of 2.4 pb^{-1} [Das14].

In the analysis the method used in [A⁺15b] is followed and is depicted by a flow chart given in Figure 4.1. Further details are given below. Also, details of Monte Carlo simulation performed in this study are discussed in this chapter.

4.1 Data Sample

The runlists given in Appendix A.1 used during the analysis passed the ALICE Quality Assurance (QA). This means that these runs satisfied the following conditions: duration of a run should be at least be 10 minutes long and it should contain at least 5000 sub-events. The run must have been taken during stable beams, with proton-proton bunches colliding at the interaction point of ALICE, at centre-of-mass energy of 8 TeV. The trigger cluster or class should contain the Muon Trigger while the readout should include both the Muon

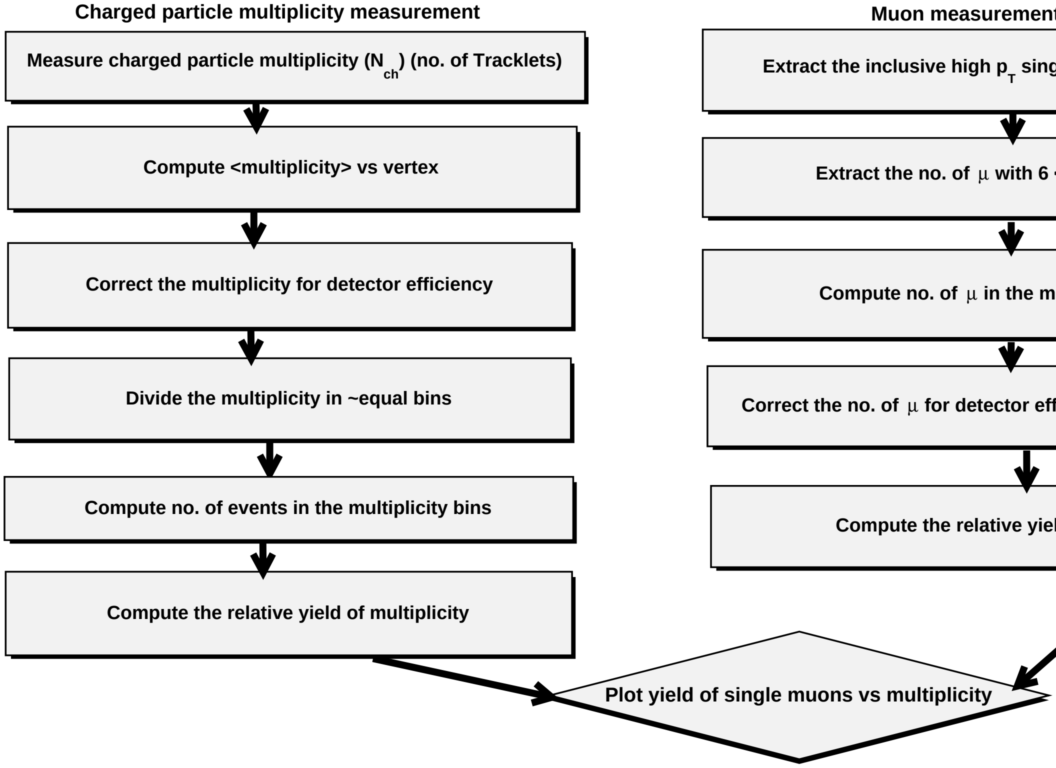

Figure 4.1: A flowchart representation of the analysis Strategy.

Trigger and Tracker stations, as well as the V0, T0 and SPD. The runs were taken from the Run Condition Table from MonALISA Repository [B+08].

4.2 Event selection Cuts

It is important to ensure that the data sample contains events of interest. As mentioned before, the interest is in high p_T single muons and MB events for the measurements of charged particle multiplicity. Below we discuss the cuts applied during the event selection.

4.2.1 Physics selection

All events passed the physics selection cut which is used to reject background and poor quality events and helps to keep beam-induced backgrounds at a minimum during the creation of AODs. In this analysis, the physics selection included stricter event selection by computing the timing of a signal that passes the triggers, to ensure that the event passed occurred at the vertex of ALICE, through the T0 detector.

4.2.2 Trigger selection

The sample is composed of T0-triggered MB events and high p_T single muons. The p_T threshold for the two triggers is greater or equal to 1 GeV/c and 4.2 GeV/c respectively.

4.2.3 Reconstructed Vertex

Only events coming from the primary vertex Z_V, and inside the SPD vertex $|Z_V^{SPD}| < 10$ cm were considered. Also, the requirement was that all considered events should contain at least a charged particle and the number of contributing tracklets ($N_{contributors}$) to the reconstructed SPD vertex is required to be greater than zero. In this way, events without any charged particles are rejected. The resolution of the SPD should be better than 0.25 cm, to ensure accurate estimation of the charged particles measured per event. In addition, since the primary vertex is more accurate in estimating the vertex position, a cut was applied which requires that the difference between the primary vertex and the SPD vertex of each accepted event be less than 0.5 cm. Events with more than one reconstructed tracklet are tagged by means of "vertexer tracks" and the "vertexer: Z" (explained below). Applying these cuts further improves the measurement by rejecting events with one tracklet. The distribution of events (MB and CMSH) as a function of the vertex position are shown in Figure 4.2. A summary of the cuts applied in the vertex selection are listed

- $\eta < 1.0$ → To minimize the loss of events.
- Title does not contain "vertexer: Z" → The "vertexer : Z" is a label tagged on events with more than one reconstructed tracklet.
- $N_{contributors} > 0$ → eliminates zero multiplicity tracklets
- $|Z_V - Z_V^{SPD}| < 0.5cm$ → Difference between primary vertex and SPD vertex, since the primary vertex is more accurate in estimating the vertex position, a cut is applied

which requires that the difference between the primary vertex and the SPD vertex of each accepted event be less than 0.5 cm.

- $\sigma Z_V^{SPD} < 0.25 cm \rightarrow$ To ensure accurate estimation of the charged particles measured per event Resolution of the SPD vertex.
- $|Z_V^{SPD}| < 10 cm \rightarrow$ Vertex position from the interaction point where events of the analysis are selected.

4.3 Charged-particle multiplicity Measurements

Multiplicity is the number of charged particles produced per event, and it is a key observable for understanding multi-parton interactions (MPI). In this study, the measurement of the multiplicity charged primary particles, reconstructed in the Silicon Pixel Detector (SPD), extending the pseudorapidity to $|\eta|< 1.0$ and vertex position $|Z_V^{SPD}| < 10$ cm to minimize loss of events. This was done by extracting the multiplicity as a function of primary vertex. The multiplicity is obtained by estimating the number of tracklets in the two layers of the SPD detector, then compute the average number of tracklets at each vertex position, thereby producing a 2D plot. This is done to see if the average number of tracklets varies with the vertex position, so that if there is a variation, then we correct for the SPD vertex dependence.

In the first step the raw multiplicity distributions is extracted - number of events as a function of $N_{tracklets}$. The measured raw number of events as a function of number of tracklets (multiplicity distributions), shown in Figure 4.3, compares the MB and CMSH triggered events, in the acceptance of the SPD. Both MB and CMSH follow the same shape (trend). Also, from the figure, it is clear that CMSH selects a higher number of reconstructed tracklets (multiplicity) than MB events. This is because CMSH select high p_T muons ($p_T \geqslant 4 GeV/c$), which includes all single muons from hard scattering processes (decays of heavy flavours), W and Z bosons, which allows access to many parton-parton interactions leading to the production of more charged particles.

To account for the variation of the SPD efficiency per run during data taking, we consider the configuration of the SPD. These changes are investigated per run for both period

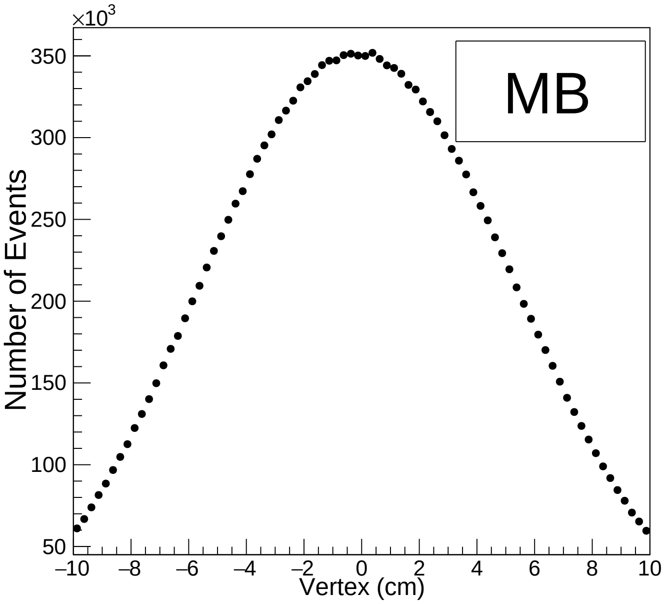

(a)

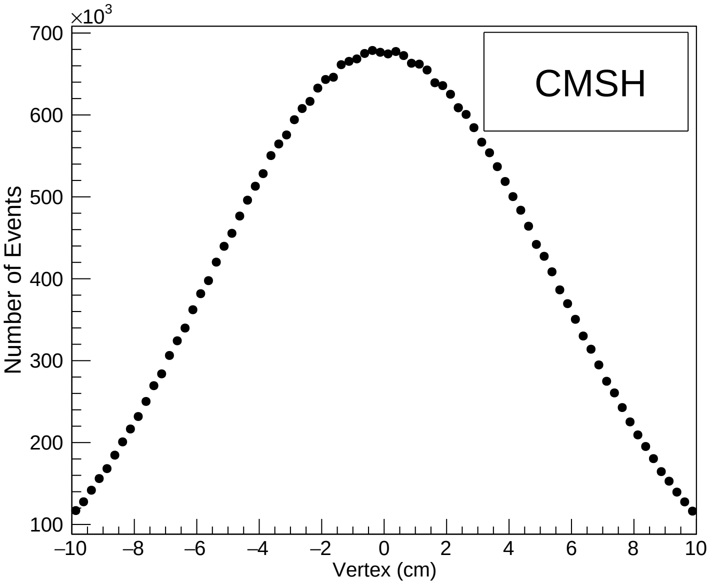

(b)

Figure 4.2: The distribution of events as a function of the vertex position for MB and CMSH triggered events in the periods of interest.

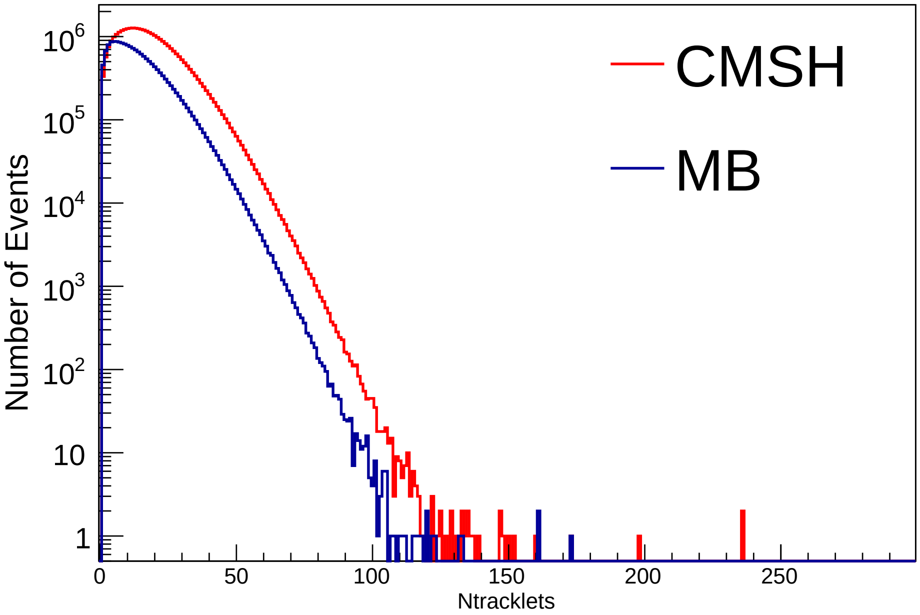

Figure 4.3: The comparison of measured raw multiplicity distributions obtained for minimum bias (MB) and high p_T single muon (CMSH) triggered events.

LHC12h and LHC12i. Figure 4.4 shows the number of active modules in the outer and inner layers of the SPD as a function of the run numbers. Overall, the total number of active modules for the inner and outer layer of the SPD is 80 and 160, respectively. Of those, about 8 were missing for the inner layer and 10 were missing for the outer layer, during periods LHC12h and LHC12i. Also, the number of active modules in the inner layer of SPD is the same for all the runs while it is not the case with the outer layer. The runs with the same SPD configuration are then grouped in sub-periods and analyzed separately to make sure that the acceptance and efficiency of the SPD is the same. Table 4.1 shows the final five sub-periods used to build the data sample in this case.

The measurement of the multiplicity of charged particles is accomplished by considering MB triggered events, as this gives an accurate account of the events and all the charged particles, as it includes the SPD. The event selection cuts discussed in section 4.2 were then applied and implemented in an analysis task (AliAnalysisTaskPtCMSH.cxx), as shown in the Appendix A.2.1.

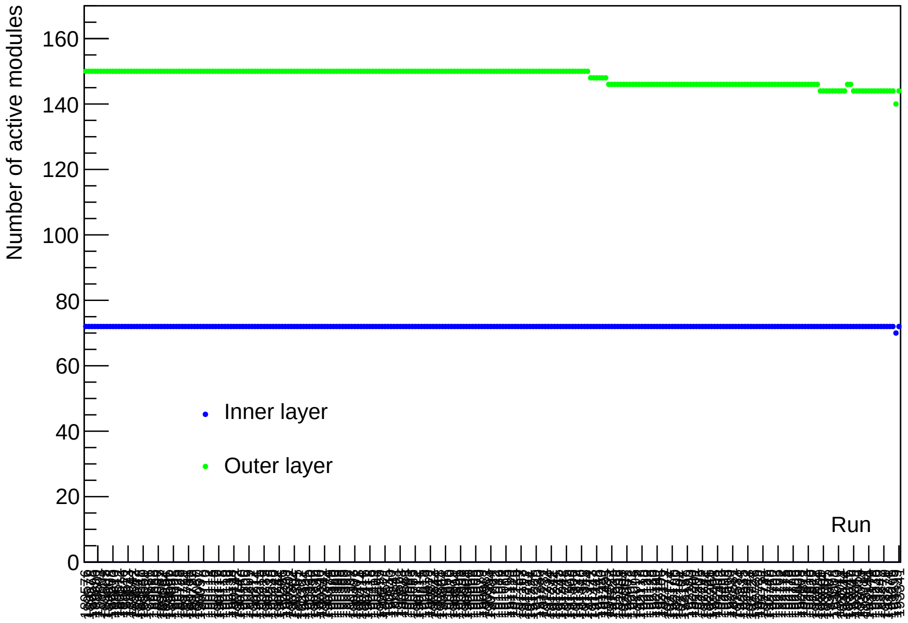

Figure 4.4: Active SPD module given as a function of the run number.

Table 4.1: Table showing Summary of the resulting 6 sub periods obtained from the number of active modules in the outer and inner layers of SPD conditions in pp runs considered in periods LHC12h and LHC12i.

Number of Active Modules (Inner Layer)	Number of Active Modules (Outer Layer)	Runs in LHC12i	Runs in LHC12h
70	140	1	0
72	144	24	0
72	146	20	52
72	148	0	6
72	150	0	167

To ascertain if there is a variation in the charged particle multiplicity with the SPD acceptance and if there is a need to make corrections for this, a 2D spectra is produce for the number of tracklets as a function of SPD vertex position, as shown in Figure 4.5. According to the figure the highest number of tracklets is concentrated in the vertex region -8 cm < vertex < 4 cm, for both MB and CMSH. In both cases, the distribution of the number of tracklets as function of vertex is not homogeneous. The average number of tracklets is computed and plotted as a function of the vertex; henceforth referred to as a tracklet profile. The raw tracklet profiles for each sub-period are then merged together. As seen in Figure 4.7 and Figure 4.6 the average multiplicity as a function of the SPD vertex does not follow a flat shape as expected. This is due to variations observed in Figure 4.4. It is a result of problems in the SPD cooling system during data taking in 2012, which compromised the efficiency of the SPD. Therefore, the measured raw multiplicity distributions must be corrected for the SPD efficiency. The tracklet profiles are used for correction.

Table 4.2: Summary of the number of events before and after event and track selection.

Period	Trigger Class Name	Number of events	
		Before cuts	After cuts
LHC12h	CMSH8-S-NOPF-MUON	31721194	24640123
	CINT8-S-NOPF-ALLNOTRD	17706128	16205979
LHC12i	CMSH8-S-NOPF-MUON	9378580	7247411
	CINT8-S-NOPF-ALLNOTRD	2550854	2237208
Total:	CMSH8-S-NOPF-MUON	41099774	31887534
	CINT8-S-NOPF-ALLNOTRD	20256982	18443187

Table 4.2 shows the summary of the number of events obtained before and after the event and track selection in this study. About *8%* MB events and about *22%* CMSH events are rejected after event and track selection is applied.

4.3.1 Multiplicity Correction

In order to correct for the SPD variations observed in Figure 4.6, equation 4.1 and equation 4.2 are used, whereby $N_{tr}(Z)$ is the raw number of tracklets (raw multiplicity) and $< N_{tr}(Z) >$ is the average raw number of tracklets at each vertex position, $< N_{tr}(Z_O) >$ is the reference value for the average multiplicity at maximum position as illustrated by the red dotted line in Figure 4.7; where, in this case, the reference value is 15.8 corresponding to the vertex position of about 6 cm. ΔN is used as the mean of a Poissonian distribution to generate ΔN_{rand}, and $N_{tr}^{corr}(Z)$ is the number of corrected tracklet or multiplicity.

$$\Delta N = N_{tr}(Z)\frac{< N_{tr}(Z_O) > - < N_{tr}(Z) >}{< N_{tr}(Z) >} \tag{4.1}$$

$$N_{tr}^{corr}(Z) = N_{tr}(Z) + \Delta N_{rand} \tag{4.2}$$

In Figure 4.8 the corrected number of tracklets are plotted as as function of the SPD vertex position where it is observed that the highest number of tracklets are homogeneously

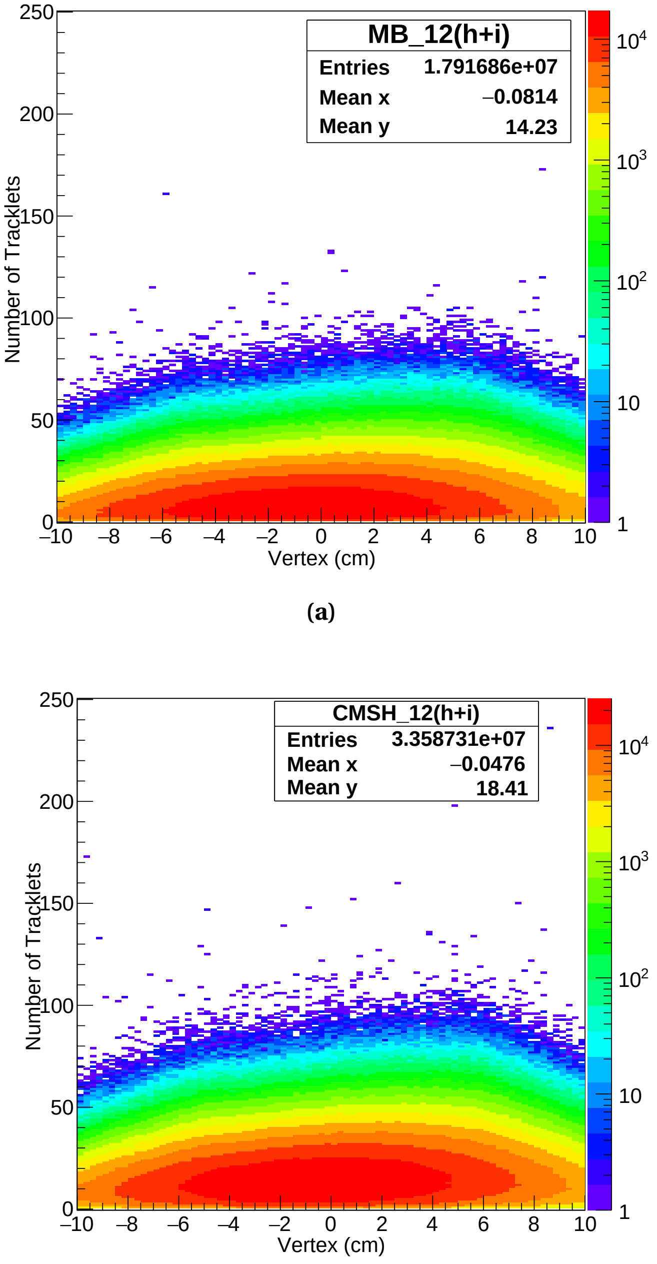

(a)

(b)

Figure 4.5: The raw number of tracklets as a function of vertex for MB and CMSH events. The colours represent the concentration of events as shown in the scale on the right-hand side of each figure where red represents high number of events.

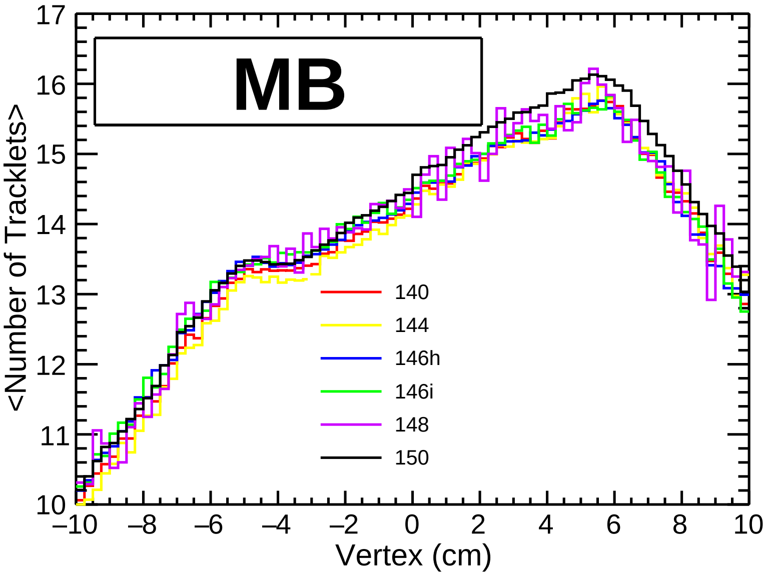

(a)

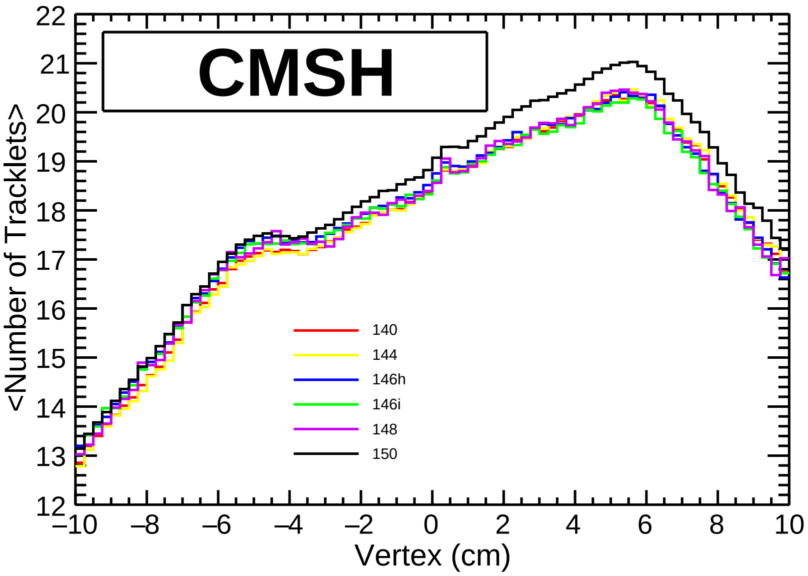

(b)

Figure 4.6: Comparison of the tracklet profiles for subperiods discussed in Table 4.1.

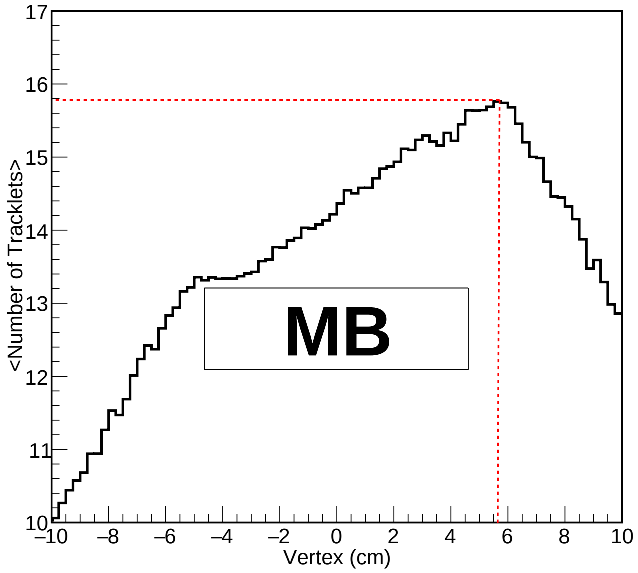

(a)

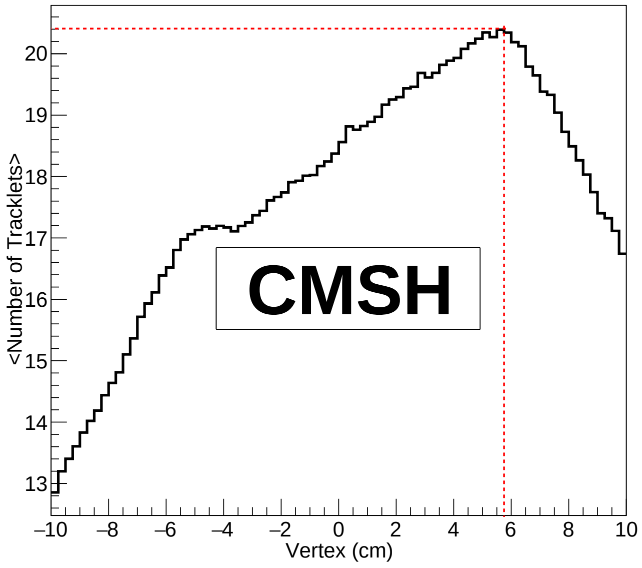

(b)

Figure 4.7: The merged raw tracklet profiles for the 5 subperiods . The red line illustrates the reference value of the average number of tracklets, $< N_{tr}(Z_O)$, and its vertex position used for the correction, as described in detail in the text.

distributed in the vertex region -5 cm < vertex < 5 cm. The corresponding corrected tracklet profiles are shown in Figure 4.9 and they are flat and constant at a value of 15.8 (for the average number of tracklets), as compared to Figures 4.6. Figure 4.10 shows the tracklet profile resulting from merging the 5 sub-periods in Figure 4.9. Here it is clear that there is little difference between the maximum and minimum values. For example, for MB the maximum and minimum values are 16 and 15.98, while for CMSH the values are 21 and 20.5 respectively.

This corrected multiplicity is not the actual produced charged particle multiplicity since it still needs to be corrected for the detector efficiency, to account and ensure that no charged particles are missed. The produced charged-particle multiplicity can be represented by equation 4.3 where "α" represents the missing normalization factor obtained from Monte Carlo simulation [Mar15] and is representative of the SPD efficiency. Therefore, the relative multiplicity is considered. The relative multiplicity at each bin is computed in equation 4.4.

$$N_{producedtracklets} = \alpha \times N_{correctedtracklets} \tag{4.3}$$

$$N_{tracklets} = <N>^{i}_{tracklets} / <N>^{tot}_{tracklets} \tag{4.4}$$

From the corrected multiplicity distributions shown in Figure 4.11, we then divide the multiplicity in such a way that the number of events in each bin is almost equal. The number of events in each multiplicity bin interval is computed and given in Table 4.4.

Table 4.3: Table showing how the corrected multiplicity is divided into equal multiplicity bins.

Multiplicity Intervals	Number of MB Events	$<N_{tracklets}>^{i}$
1-7	4.63×10^{6}	4.34
8-10	2.19×10^{6}	8.99
11-13	2.02×10^{6}	11.98
14-17	2.33×10^{6}	15.44
18-22	2.27×10^{6}	19.87
23-27	1.61×10^{6}	24.85
28-34	1.39×10^{6}	30.65
35-300	1.31×10^{6}	42.99
1-300	1.77×10^{7}	15.99

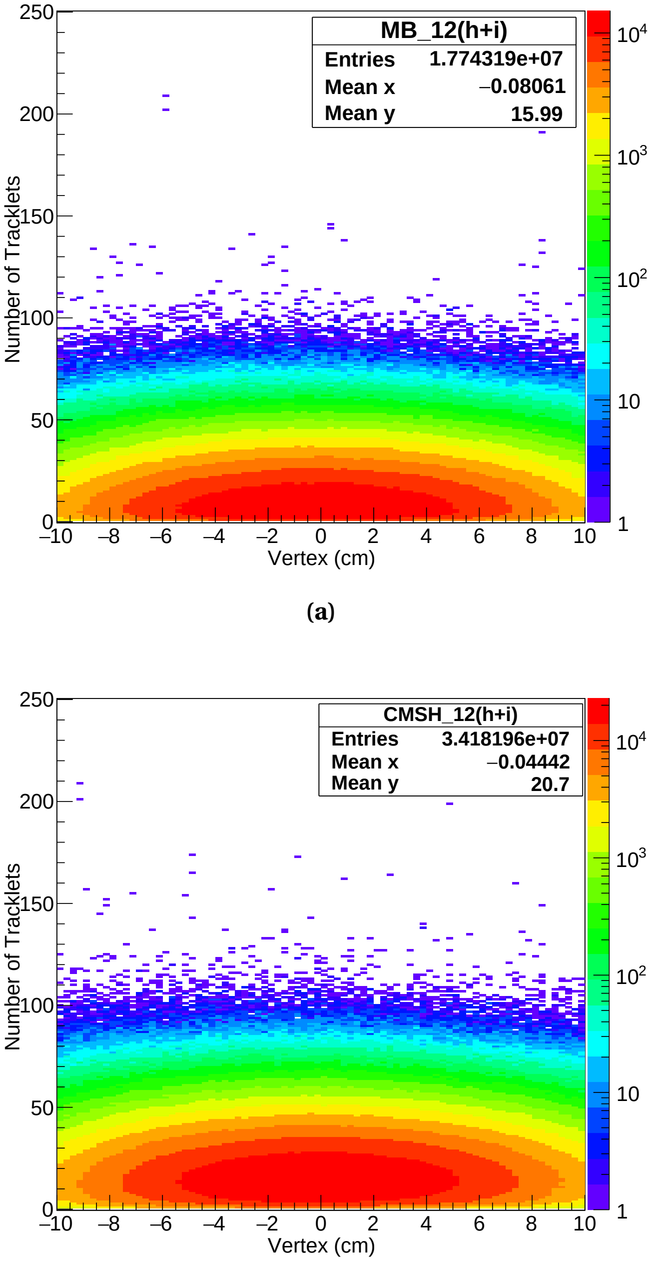

(a)

(b)

Figure 4.8: The corrected number of tracklets as a function of vertex for MB and CMSH events. The colours represent the concentration of events as shown in the scale on the right-hand side of each figure where red represents high number of events.

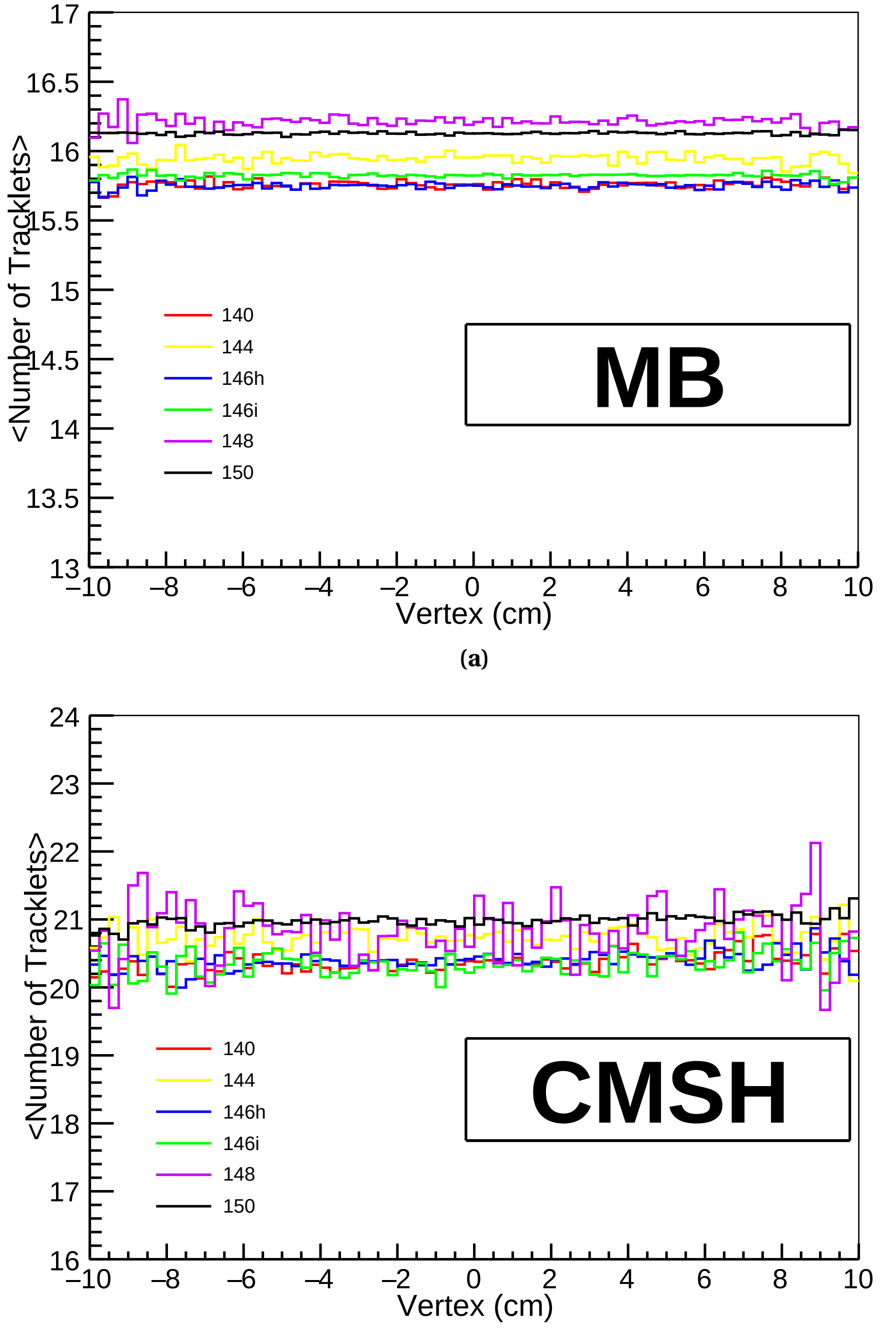

(a)

(b)

Figure 4.9: Corrected tracklet profiles for different sub-periods of interest in this study.

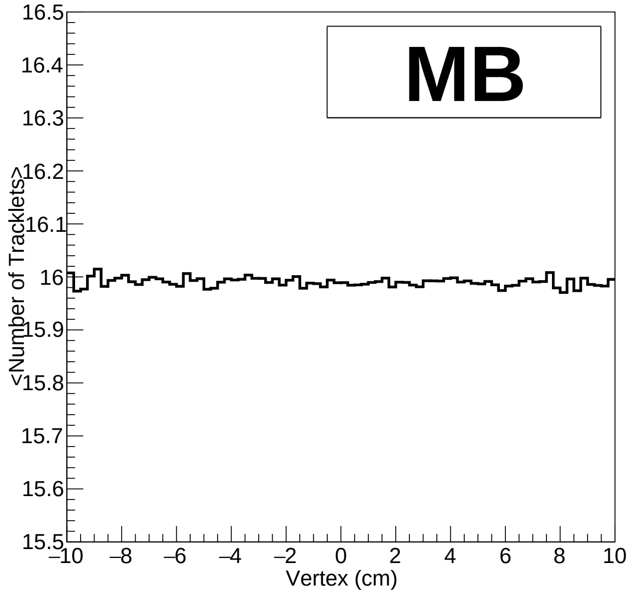

(a)

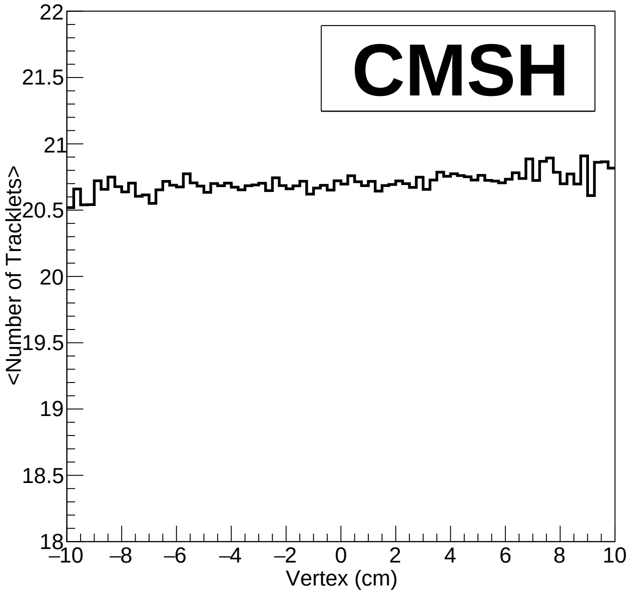

(b)

Figure 4.10: The merged corrected tracklet profiles for the 5 subperiods.

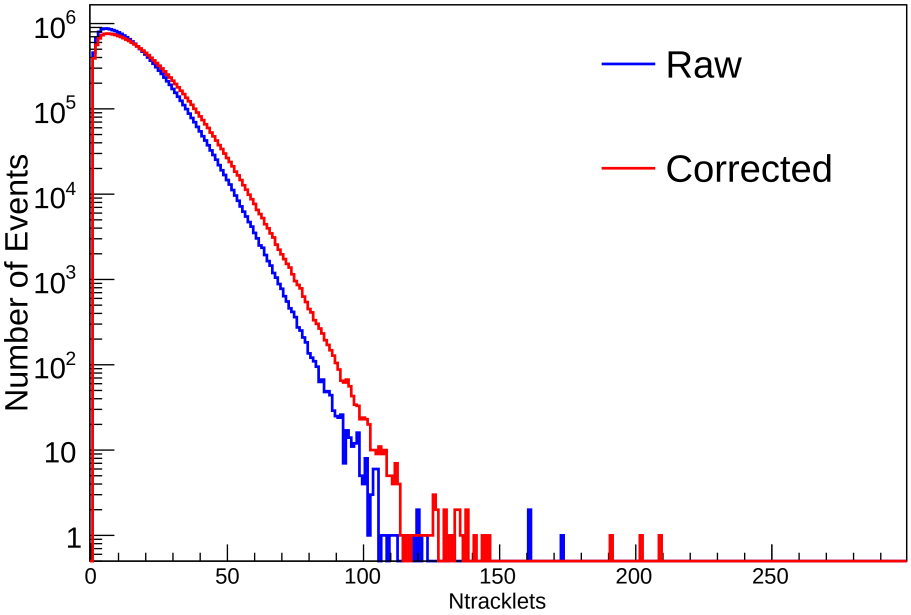

Figure 4.11: Raw and Corrected multiplicity distributions.

The results of the computed relative multiplicity are presented in the next chapter. The following discussion is about the extraction of the single muons.

4.4 Single Muon Measurement

In ALICE muons are measured in the Muon Spectrometer located at forward rapidity. As mentioned earlier, the single muon high p_T trigger CMSH8-S-NOPF-MUON is used to select muons of interest in this study. Track cuts are used to reduce various kinds of background in the measurement of muons. The following cuts are applied.

Geometrical cuts

This cut takes into account the geometrical acceptance of the Spectrometer , i. e, the pseudorapidity (η) and the exit polar angle with respect to the front absorber (θ_{abs}). Thus, in this analysis the tracks are reconstructed in the region $-4 < \eta^{\mu} < -2.5$ to eliminate all muon tracks outside the spectrometer and $2^{\circ} < \theta_{abs} < 9^{\circ}$, whereby θ_{abs} is the track polar angle measured at the end of the absorber. This cut removes muons that emerge at small angles that have crossed the thick beam shield and consequently suffered multiple scattering in the absorber.

Trigger matching cut

In order to remove punch through hadron (muons from the decay of primary and secondary pions(π) and Kaons(K), that are absorbed in the iron wall), it is essential to apply a trigger matching cut. This cut requires that each muon track reconstructed in the tracking chambers should match the track in the trigger chambers. All muons selected in this case passed the p_T greater than or equal to 4.2 GeV/c.

Correlation of the momentum and the distance of closest approach: pxDCA cut

The distance of closest approach (DCA), is the distance between the interaction vertex and the extrapolated muon track in the plane containing the vertex, and is perpendicular to the beam direction. Owing to the multiple scattering in the front absorber, the DCA distribution of tracks coming from the interaction vertex can be described by a Gaussian function, whose width depends on the absorber material and is proportional to $1/p$, where p is the muon momentum. This $p \times DCA$ cut, which is the correlation of momentum and distance of closest approach, eliminates muons that are not coming from the interaction point. The $p \times DCA$ is set at 5 or 6 times the standard deviation, depending on run conditions for data being analyzed.

Muons are selected in the region $6 < p_T < 20$ GeV/c because in this region muons from the decay of heavy quarks are expected to dominate.

In order to select single muons of interest in this study, i.e, muons from the decays of heavy-flavour, we take into account all single muons contributing to the total inclusive muon p_T-differential distribution. The inclusive single muon p_T distribution consists of hadronic muons (muons from the decay of pions and kaons), heavy flavour muons (muons from charm and beauty decays) and those from $W^{\pm}$ and Z bosons. Figure 4.12, taken from the performance study of Z Conesa Del Valle [CDV+07] shows the inclusive p_T distributions obtained from PYTHIA simulations where most of these components dominate the p_T spectra. Although not shown in Figure 4.12 however, hadronic muons dominate $p_T < 6$ GeV/c while as can be seen in Figure 4.12, heavy-flavour muons ($\mu^{\pm} \leftarrow b, \mu^{\pm} \leftarrow c \leftarrow b, \mu^{\pm} \leftarrow c$) are dominant in the region $6 < p_T <$20 GeV/c while W and Z bosons dominate the high p_T region above 30 GeV/c.

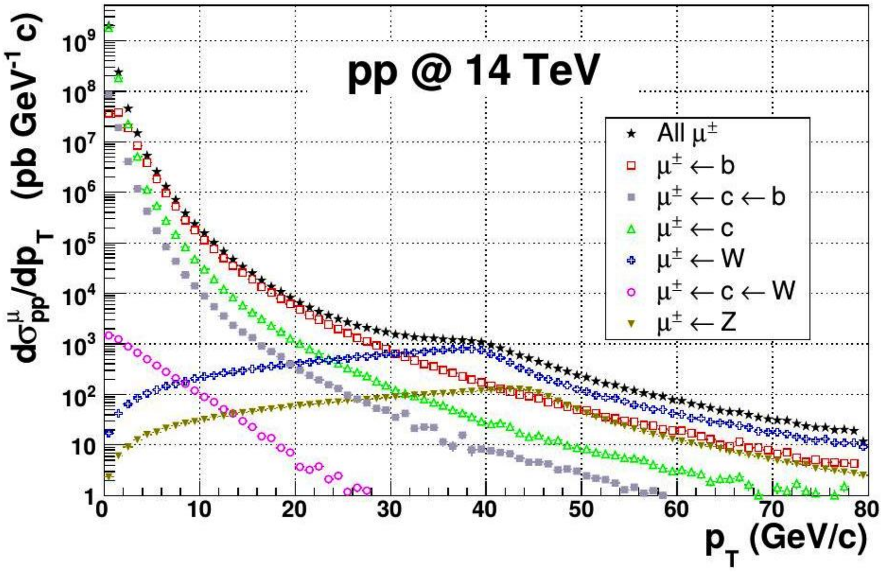

Figure 4.12: The inclusive single muon p_T spectrum [CDV+07].

The inclusive single muon p_T spectrum shown in Figure 4.13, was obtained from measurements with ALICE in $-4 < \eta < -2.5$ in pp data collected in 2012, during LHC runs. The distribution was then extracted.

Using the multiplicity bins discussed in section 4.3.1, the number of single muons from charm (c) and beauty (c) decays was extracted in the region $6 < p_T < 20$ GeV/c from the inclusive single muon p_T distribution shown in Figure 4.13. Table 4.4 shows the number of single muons in the region $6 < p_T < 20$ GeV/c extracted in the multiplicity bin intervals.

The measured number of muons depend on the performance of the detector during a data taking period. The performance of the detector is influenced by the detector acceptance (A) and efficiency (ϵ), which includes the tracking and trigger efficiency as well as the alignment due to variations of positions of detector elements (see, section 3.2.15). Therefore, it is necessary to correct the measured number of muons for acceptance and efficiency ($A \times \epsilon$). The correction factor for $A \times \epsilon$ is obtained by performing Monte Carlo simulations.

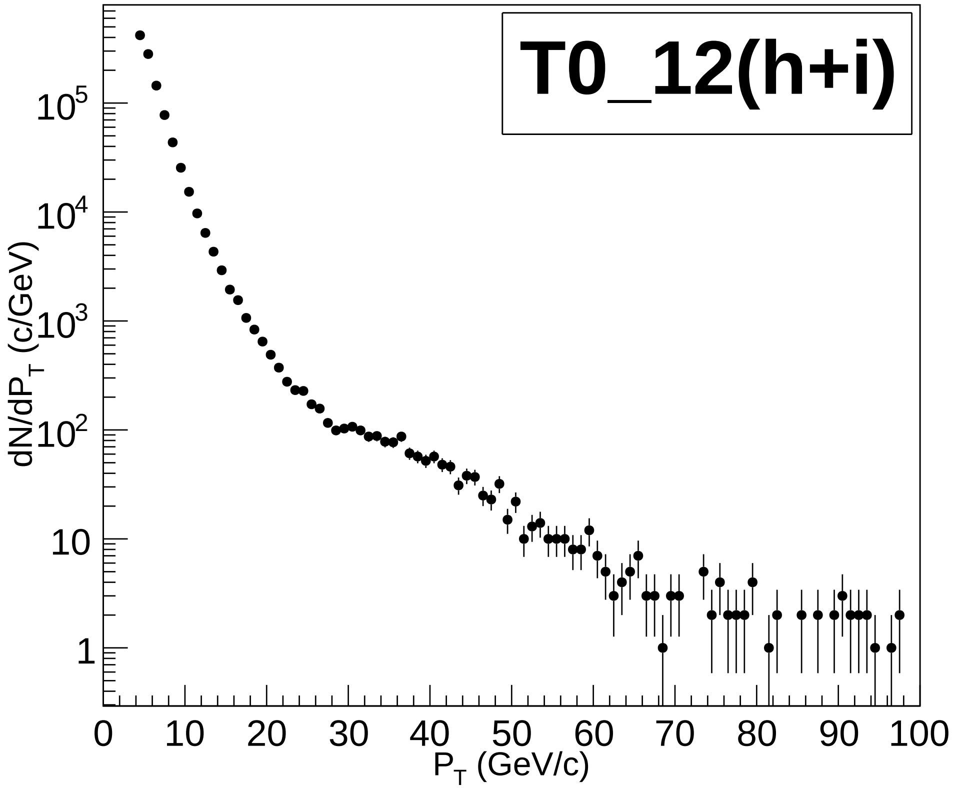

Figure 4.13: The inclusive single muon p_T spectrum extracted after implementing the standard muon cuts discussed in section 4.4. The error bars represent the statical errors.

Table 4.4: Table showing the number of single muons (μ) with $6 < p_T < 20$ GeV/c extracted from the inclusive p_T spectrum at the given multiplicity bin.

Multiplicity Intervals	Number of CMSH Events	Number of μ (N^{μ}) ($6 < p_T < 20$ GeV/c)
1-7	4.86×10^6	18431
8-10	3.16×10^6	19334
11-13	3.38×10^6	24961
14-17	4.50×10^6	39420
18-22	5.11×10^6	52842
23-27	4.17×10^6	49372
28-34	4.12×10^6	54387
35-300	4.86×10^6	77686
1-300	3.42×10^7	336433

4.4.1 Monte Carlo simulations using FONLL

In Monte Carlo based simulations, a random value is chosen for each of the tasks. This is based on the range of estimates. The model is calculated based on the selected random value. The result of the model is recorded and the process repeated. A Monte Carlo simulation calculates the model hundreds or thousands of times, each time it uses a different randomly selected value. When the simulation is finished, there is a large number of results obtained from the model, each is based on random input values. These results can be used to describe the probability of reaching various results in the model.

General-purpose Monte Carlo generators like (PYTHIA [S+06], POWHEG [S+07], HERWIG [K+13] etc.) supply fully unique simulations of high-energy hadron-hadron collisions. They play a crucial role in QCD modeling, (especially great for aspects beyond fixed-order perturbative QCD) in data analysis, whereby they are used *together with detector simulation to provide a realistic estimate of the detector response to collision events*; and in the planning of new experiments, where they are used to estimate signals and backgrounds in high-energy processes.

The aim of the simulation in this study is to evaluate the acceptance × efficiency ($A \times \epsilon$) of the muon spectrometer during the period of data taking considered in this study. From the simulations the shape of the p_T and eta (η) distributions of the differential cross sections are obtained by simulating the production cross section of c and b quarks. The first part of the simulation involves calculations of differential cross sections for muons from charm and beauty decays, using the Fixed-Order-Next-To-Leading-Log (FONLL) [MCN98] as it is readily available online. In FONLL, non-perturbative fragmentation into heavy hadrons and their subsequent decays into other final states (leptons, quarkonia, etc) can also be included. Inputs are set on FONLL and submitted. The run time may be as long as a few minutes in this case, since the aim is to produce a differential cross section signal for c and b in pp collision, by considering the production $p + p \rightarrow \text{charm} + \text{X}$ and $p + p \rightarrow \text{beauty} + \text{X}$, the parton distribution function (PDF) CTEQ6.6 [N+08] for the heavy quark decay channels:

$$b \rightarrow \mu + x \; (BR^{1} - 10.86\%) \tag{4.5}$$

$$b \rightarrow (70\% D^{0} + 30\% D^{+}) \rightarrow \mu + x \tag{4.6}$$

$$70\% D^{0} + 30\% D^{+} \rightarrow \mu + x \; (BR - 10.33\%) \tag{4.7}$$

Figures 4.14 shows the results from differential cross sections calculation with FONLL for $0 < p_T < 40$ (GeV/c) and pseudo-rapidity: $-6 < \eta < 6$, where the black points represent the sum of all contributing processes. The fitting procedure for the sum of the cross sections was then implemented for both p_T and η using the fit functions, given in equations 4.8 and 4.9, to obtain parameters p_0 up to p_7 . These functions were chosen because they give a good fit for the sum in the p_T and η range of interest, see Figure 4.15. The parameters were then used as inputs in ALIROOT for generating and reconstructing the muon tracks , ultimately used to obtain $A \times \epsilon$. In order to reproduce the p_T and η distribution macros sim.C and reco.C (shown in Appendix A.3) were used. The generated p_T spectra represents an ideal case, i. e, 100% efficient muon spectrometer. The reconstructed p_T spectra represents the real case as it includes the configuration (e.g. alignment, High Voltage (HV) value, etc.) of the muon spectrometer during data taking in 2012. This information is available in the Offline Calibration Data Base (OCDB) [R.G14].

$$p0 \times 10^{x(p1(1-10^{xp2})+p3)} \times \frac{1}{x^{p4}}(p5 + xp6 + x^{2}p7) \tag{4.8}$$

$$p0 + xp1 + x^{2}p2 + x^{4}p3 + x^{6}p4 + x^{8}p5 \tag{4.9}$$

---

[1] Branching Ratio

4.4.2 Acceptance and efficiency ($A \times \epsilon$) corrections

The results (differential cross sections for muons produced from the decay of charm and beauty in pp collisions at 8 TeV), obtained from the simulations are shown in Figure 4.15. Only 20% of the muon events were selected and simulate on a run by run basis, to take care of the fluctuations in the detector configuration, which might vary run to run.

The $A \times \epsilon$ for combined periods LHC12h and LHC12i was obtained using equation 4.10, which takes into account the generated (ideal) p_T distribution (black points) and reconstructed (realistic) p_T distribution (open points), given in Figure 4.16. The acceptance × efficiency distributions given as functions of p_T and η are shown in Figures 4.17 and 4.18. As shown in the region of interest (6-20 GeV/c), and illustrated by the blue dotted lines in Figure 4.17, the average value obtained for the $A \times \epsilon$ is about 69.17 %.

$$A \times \epsilon = \frac{p_T^{Reconstructed}}{p_T^{Generated}} \tag{4.10}$$

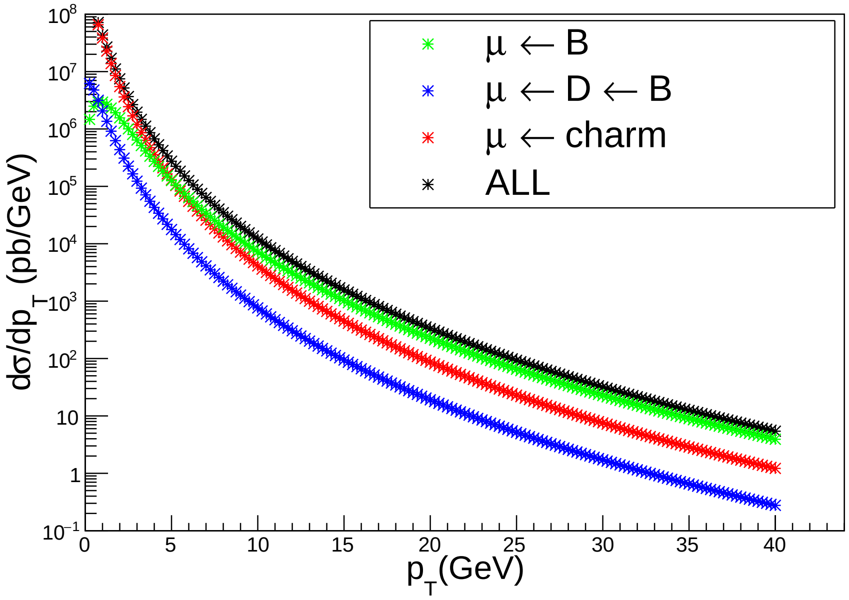

(a)

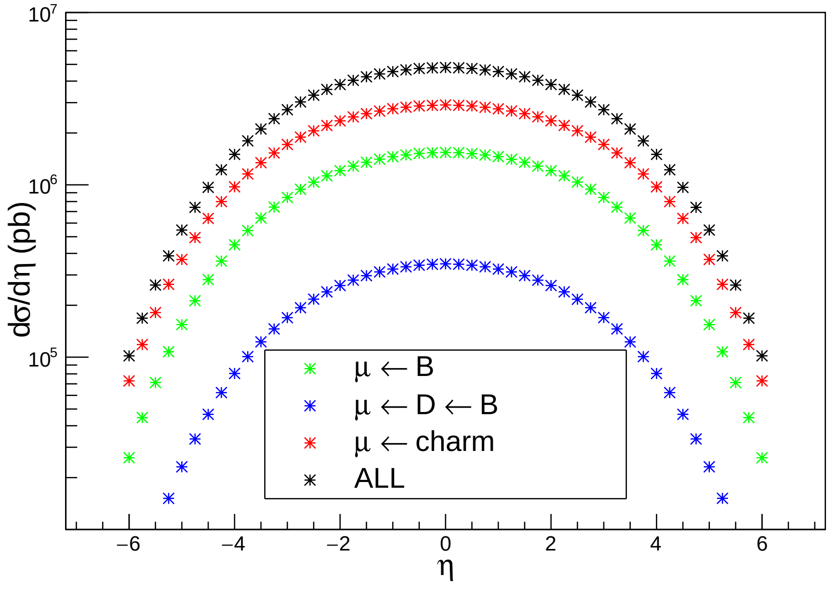

(b)

Figure 4.14: Differential production cross-sections for muons produced from charm and beauty quarks as a function of (a) p_T and (b) pseudo-rapidity (η) for p-p collisions at 8TeV obtained from calculations with FONLL [MCN98] event generator.

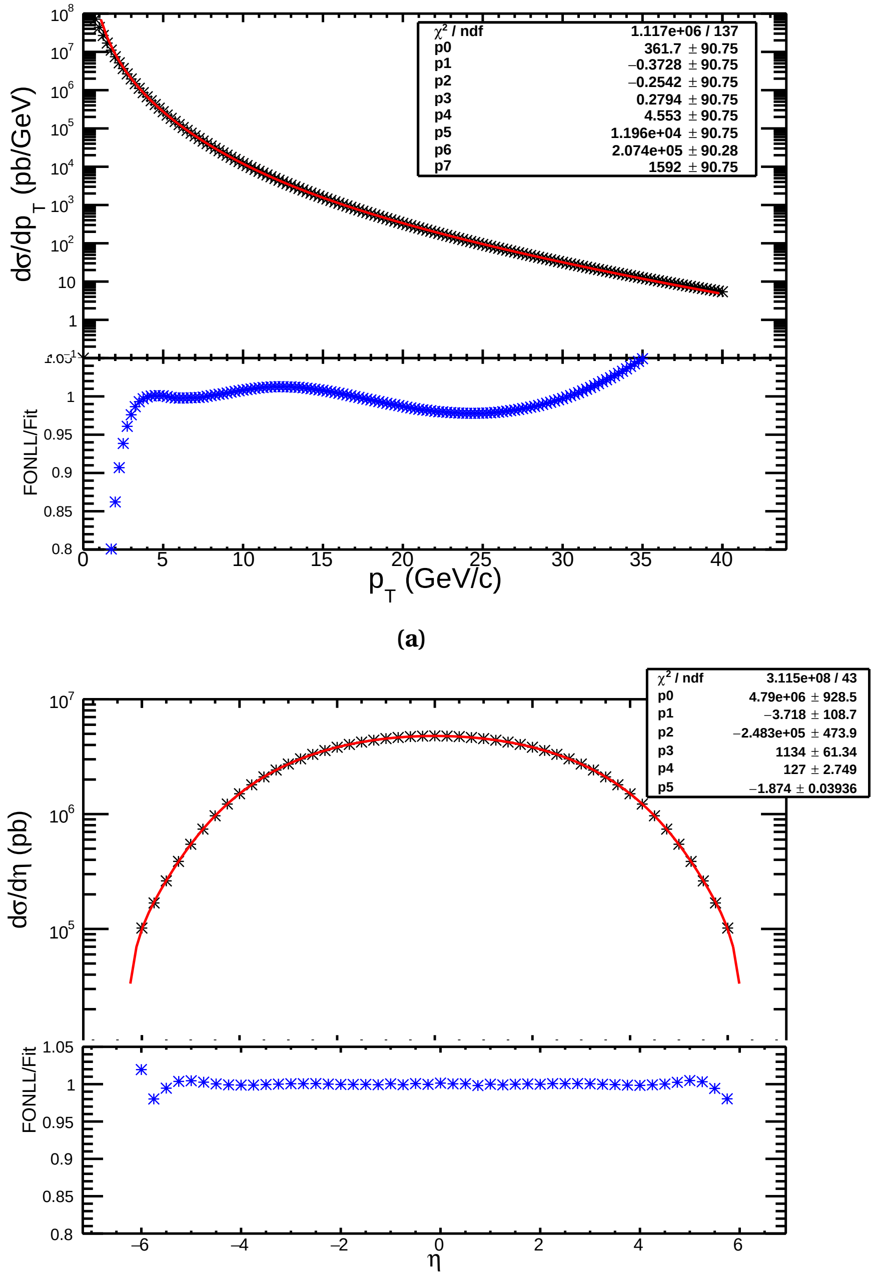

(a)

(b)

Figure 4.15: The sum of the differential p_T and η-distributions (in black) with fit functions (in red). In both cases the top figure shows the sum of all differential cross sections fitted with the function given in equation 4.8 and 4.9. The bottom part for each figure shows the ratio of the sum (in black) of the differential cross sections to the fit function.

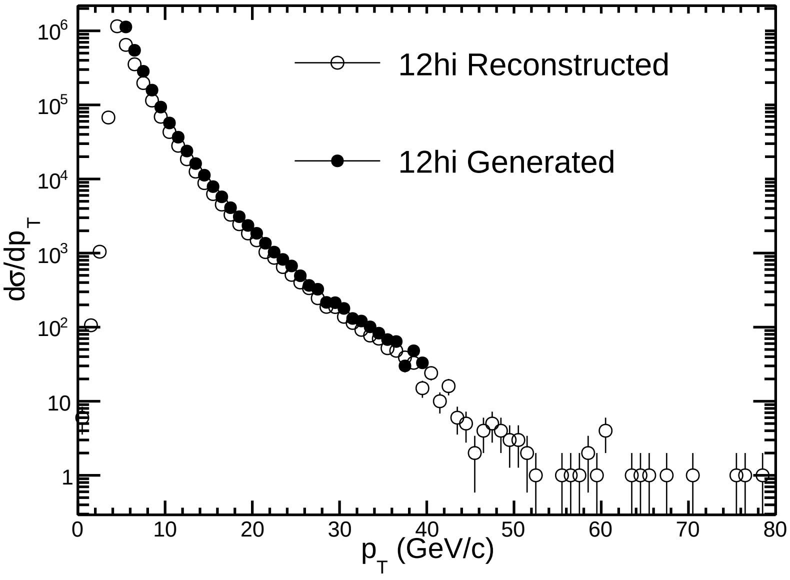

Figure 4.16: The generated and reconstructed p_T distributions for periods LHC12h and LHC12i the vertical bars represent statistical errors.

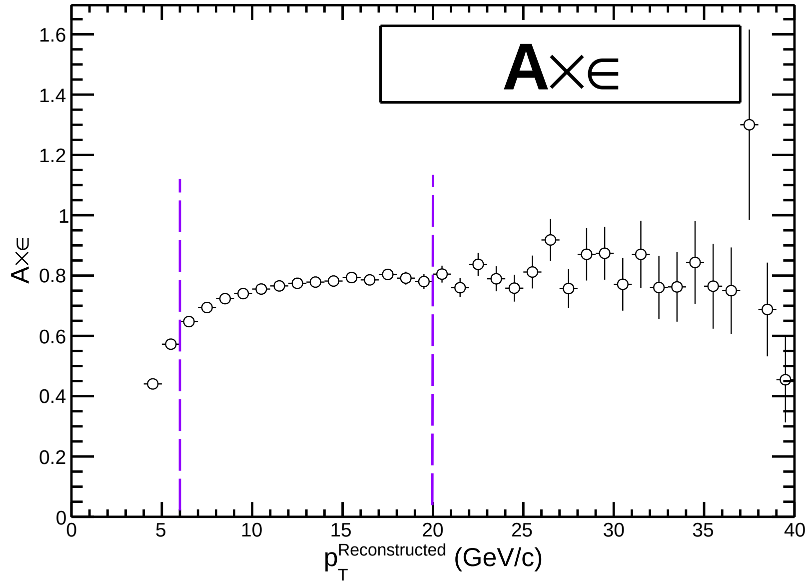

Figure 4.17: The A×ϵ of the muon spectrometer for combined periods LHC12h and LHC12i in CMSH events. The vertical bars represent statistical errors.

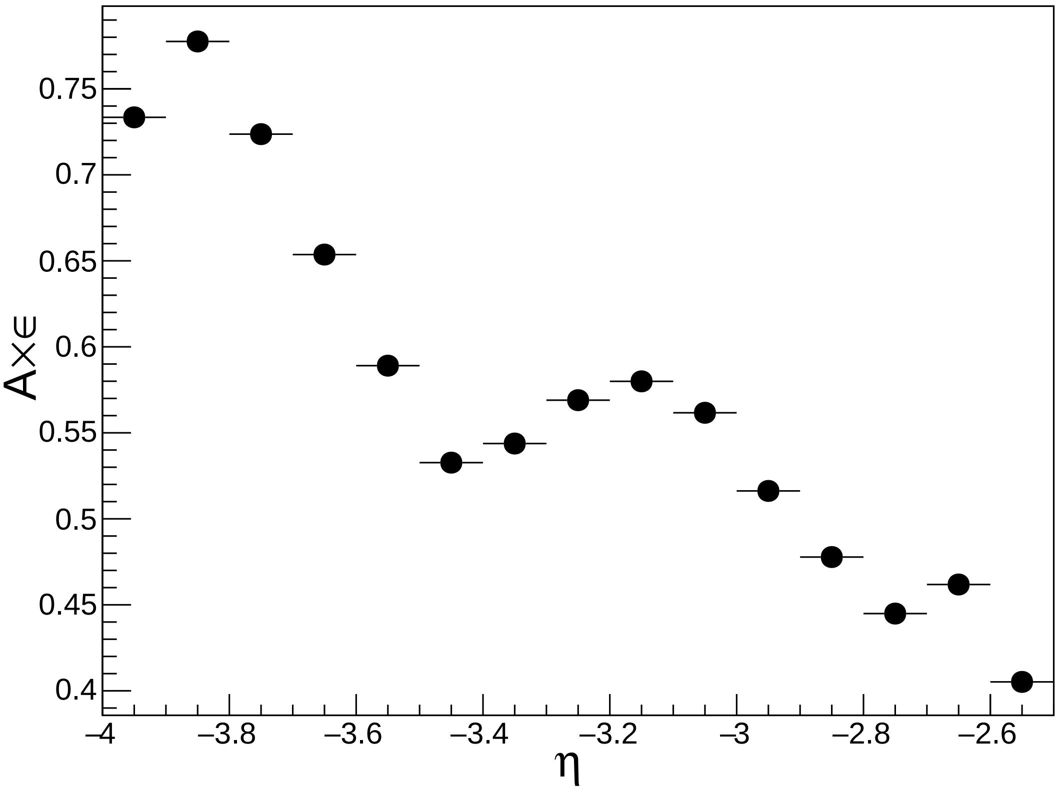

Figure 4.18: The A×ϵ of the muon spectrometer for combined periods LHC12h and LHC12i in CMSH events, $-4 < \eta^{\mu} < -2.5$. The error bars represent statistical errors.

4.5 Muon measurement correction

The efficiency value obtained above is used to correct the number of measured muons, i. e, the actual number of muons produced per events. This is done in the following way:

$$corrected\ number\ of\ muons = \frac{number\ of\ measured\ muons}{A \times \epsilon} \tag{4.11}$$

The number of muons per event are then extracted at a given multiplicity bin interval discussed in Section 4.4. The corrected number of muons is shown in Table 4.5. The final results are discussed in detail in the following chapter.

Table 4.5: The corrected number of muons in the region $6 < p_T < 20$ GeV/c.

Multiplicity Intervals	Number of μ (N^{μ}) ($6 < p_T < 20$ GeV/c)	Corrected Number of μ (N_{μ}^{i})
1-7	18431	26646
8-10	19334	27951
11-13	24961	36086
14-17	39420	56990
18-22	52842	76394
23-27	49372	71378
28-34	54387	78628
35-300	77686	112312
1-300	336433	486386

CHAPTER 5

RESULTS: YIELD OF SINGLE MUONS FROM HEAVY FLAVOUR DECAY VS MULTIPLICITY

The main purpose of this thesis is to investigate the correlation of the yield of muons from the decays of heavy flavours (charm and beauty), with the charged-particle multiplicity. This chapter gives a summary and discussion of the results obtained in the analysis described in Chapter 4. It must be noted that all results shown in this chapter include only statistical uncertainty.

5.1 Charged particle multiplicity

In chapter 4 the raw multiplicity of charged particles was measured (see Figure 4.3), using the number of reconstructed tracklets in the optimized region of the SPD. This raw multiplicity was plotted as a function of the vertex position (Figure 4.5), which in turn, was used to compute the average charged particle multiplicity, to see if corrections for SPD acceptance are necessary, i.e, extraction of the tracklet profiles (Figure 4.6 and Figure 4.7). The corrected tracklet profiles and multiplicity distribution is then shown in Figure 4.9 and 4.11. Since the corrected multiplicity does not represent the "true" multiplicity therefore, the charged-particle multiplicity, normalized to the average multiplicity is obtained. This relative multiplicity, computed using equation 5.1, was sliced into 8 bin intervals. The relative multiplicity at the i_{th} bin is given by;

$$rel.N^{i}_{tracklets} = \frac{<N>^{i}_{tracklets}}{<N>^{Tot}_{tracklets}} \tag{5.1}$$

Table 5.1: Average number of tracklets per multiplicity bin and the relative multiplicity.

Multiplicity Intervals	$<N_{tracklets}>^{i}$	$\frac{<N_{tracklets}>^{i}}{<N_{tracklets}>^{Tot}}$
1-7	4.34	0.27
8-10	8.99	0.56
11-13	11.98	0.75
14-17	15.44	0.97
18-22	19.87	1.24
23-27	24.85	1.55
28-34	30.65	1.92
35-300	42.99	2.69
1-300	15.99	1

5.2 Heavy-flavour Muons

The inclusive yield of single muons from charm and beauty decays per given multiplicity bin interval as well as the total yield, are defined as the number of muons per minimum bias (MB) events. This is shown in equation 5.2 and 5.3, where N^{i}_{μ} is the number of muons in the i_{th} bin, N^{μ} is the number of muons in the region $6 < p_T < 20$ GeV/c. $A \times \epsilon$ is the acceptance × efficiency of the muon spectrometer obtained in subsection 4.4.1. N^{tot}_{μ} is the total number of muons. The number of events is extracted as discussed in Chapter 4, section 4.4 and the results are shown in column three in Table 5.2. The self-normalized yield is computed from the yield of heavy flavour muons in each multiplicity bin, defined in equation 5.4, where Y^{i} is the yield computed at the i_{th} bin (each multiplicity bin interval), Y^{tot} is the total yield, N^{i}_{CMSH} is the number of CMSH events, and the total number of CMSH events is N^{tot}_{CMSH}.

$$Y^{i} = \frac{N^{i}_{\mu}}{N^{i}_{CMSH} \times (A \times \epsilon)_{i} \times f_{i}} \tag{5.2}$$

$$Y^{tot} = \frac{N^{tot}_{\mu}}{(A \times \epsilon)_{tot} \times N^{tot}_{CMSH} \times f_{tot}} \tag{5.3}$$

$$Y = \frac{Y^i}{Y^{tot}} = \frac{N^i_\mu}{N^{tot}_\mu} \times \frac{N^{tot}_{CMSH}}{N^i_{CMSH}} \tag{5.4}$$

Table 5.2: The number of events and yield of high p_T single muons in the region $6 < p_T < 20$ GeV/c.

Multiplicity Intervals	Number of CMSH Events	Corrected Number of μ (N^i_μ)	Relative Yield(Y)
1-7	4.86×10^6	26646	0.39
8-10	3.16×10^6	27951	0.62
11-13	3.38×10^6	36086	0.75
14-17	4.50×10^6	56990	0.89
18-22	5.11×10^6	76394	1.05
23-27	4.17×10^6	71378	1.20
28-34	4.12×10^6	78628	1.34
35-300	4.86×10^6	112312	1.62
1-300	3.42×10^7	486386	1.00

Note that $A\times\epsilon$ is the same in each multiplicity bin thus the value of $A\times\epsilon$ used in equation 5.4 is equal to 0,6917. The total yield is determined by taking the ratio of the yield to the total yield in each bin. The results are tabulated in Table 5.2. Therefore, the total number of CMSH events (N^{tot}_{CMSH}) and the number of muons (N^{tot}_μ) in the region $6 < p_T < 20$ GeV/c are, $N^{tot}_{CMSH} = 3.42 \times 10^7$ and $N^{tot}_\mu = 486386$, respectively. The relative yield of single muons shown in Table 5.2 are plotted as a function of relative multipicity given in Table 4.4.

5.3 Correlation of the yield of single muons from heavy flavour decay with charged particle multiplicity

The preliminary results obtained in this study are shown in Figure 5.1. It must be noted that these results include only statistical uncertainties. They do not include systematic uncertainties (signal extraction, background subtraction, alignment affects, pile-up, etc.) as this part has not been done and thus did not form part of this study. Figure 5.1 shows that the inclusive yield of single muons from charm and beauty (heavy flavour) decays measured in the forward rapidity of ALICE increases with the charged particle multiplicity.

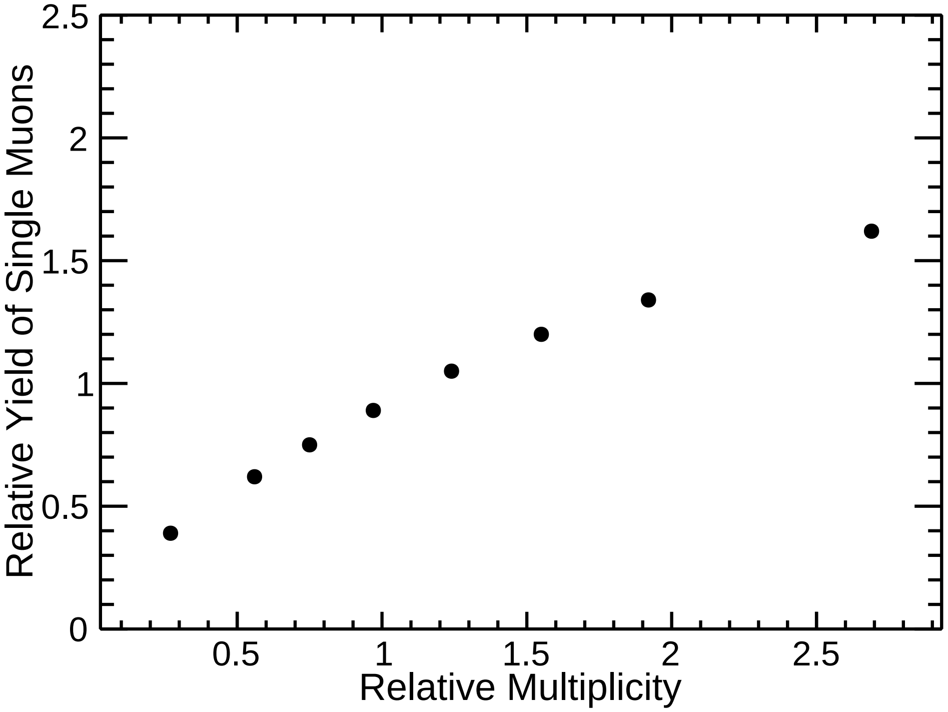

Figure 5.1: The inclusive yield of single muons from charm and beauty (heavy flavour) decays as a function of charged particle multiplicity.

As discussed in Chapter 1 and 2, the multiplicity of charged particles is a direct measure of the number of partonic interactions in pp events. Therefore, it is logical to tentatively attribute the increase observed in Figure 5.1 to multi-parton interactions (MPIs). The high p_T muons of interest in this study, are those produced in the region $6 < p_T < 20$ GeV/c; a region in which single muons from the decay of heavy flavours (c and b) are dominant (assuming the contribution of W bosons is negligible below $p_T \leqslant 20$ GeV/c) [CDV+07]. Therefore, if MPIs affect hard processes, then the yield of heavy flavour decay muons should scale with the number of partonic collisions, and the observed correlation will be a direct consequence.

CHAPTER 6

SUMMARY AND CONCLUSION

The purpose was to study the production of single muons produced from heavy flavour decays, as a function of charged-particle multiplicity in pp collisions, at 8 TeV in ALICE. This was demonstrated in Chapter 1, where we showed that ALICE, due to its pseudorapidity coverage with respect to other LHC experiments, is capable of measuring heavy flavours and charged-particle multiplicity in pp collisions, at LHC energies. The measurements were accomplished by following the analysis strategy described in previous studies [Col12c, Col15b], where it was observed that the yield of heavy quarks (J/Ψ and D mesons) increases linearly with multiplicity.

In Chapter 2 the relevant theoretical background (QCD), particularly for high-energy pp collisions, was provided. The chapter highlighted the importance of multi-parton interaction, as well as heavy-flavour production.

Chapter 3 gave an overview of the ALICE experiment, with an emphasis on the Muon Spectrometer, which covers the forward pseudo-rapidity range of -4.0 < η < -2.5. The details of the run conditions are also given; the online and offline framework used during data taking and analysis. This was followed by a concise description of the measurement of charged-particle multiplicity in the optimized region of the SPD, at $|\eta|$ <1.0 and $|Z_V^{SPD}|$ < 10 cm, as well as measurement of muons in the forward rapidity.

Chapter 4 discussed the selection criteria employed to select events and tracks of interest it also provided details of the analysis strategy followed in the measurent of the multiplicity of charged-particles, using the SPD, by using the number of tracklets as an estimator of the multiplicity. Then the yield of single muons, measured at forward rapidity -4 < η < -2 in the region 6 < p_T < 20 GeV/c, was extracted per multiplicity bin intervals. The number of muons has been corrected for the detector acceptance and efficiency.

In Chapter 5, the preliminary results obtained in the analysis were presented and shown in Figure 5.1. These preliminary results show that the yield of heavy flavour muons increases with increasing charged-particle multiplicity. This is indicative of a strong dependency of the production of heavy-flavours to the multiplicity of charged particles. The result, despite being preliminary, supports the trend that was also observed in [Col12c, Col15b].

The result presented in this thesis do not include systematic uncertainties (such as, signal extraction, background subtraction, alignment effects and pile-up studies). Background studies relevant to this study are those concerning hadronic, as well as electroweak boson contributions in the inclusive p_T-differential yield, for single muons at forward rapidity. Therefore, as an outlook to this study, it is highly recommended to conduct thorough studies of the systematic uncertainties, for the final results. Also, it would be interesting to compare data from this study with those obtained from the analysis of data collected during high multiplicity runs in pp collisions, at 13 TeV by ALICE, in RUN 2 of the LHC in 2015.

BIBLIOGRAPHY

[A$^+$74] J. J. Aubert et al. Experimental observation of a heavy particle j. *Phys. Rev. Lett.*, 33:1404–1406, Dec 1974.

[A$^+$15a] G. Aad et al. Combined Measurement of the Higgs Boson Mass in pp Collisions at $\sqrt{s} = 7$ and 8 TeV with the ATLAS and CMS Experiments. *Phys. Rev. Lett.*, 114:191803, May 2015.

[A$^+$15b] L. Aphecetche et al. Forward J/Ψ yield and mean p_T as a function of the charged particle multiplicity at midrapidity in p-Pb and Pb-p collisions at at $\sqrt{s} = 5.02$ TeV. *Analysis Note*, December 2015.

[ALI11] The ALICE Offline Bible . `http://aliweb.cern.ch/Offline/AliRoot/Manual.html`, 2011. [Online; accessed 29-January-2016].

[And14] Jens Oluf Andersen. Thermal QCD in extreme conditions. `https://www.ntnu.edu/physics/theoretical/thermqcd`, 2014. [Online; accessed 27-January-2016].

[ATL10] Track-based underlying event measurements in pp collisions at sqrts = 900 GeV and 7 TeV with the ATLAS Detector at the LHC. 2010.

[B$^+$87] R. Brun et al. GEANT3. *CERN-DD-EE-84-1*, 1987.

[B$^+$08] S Bagnasco et al. Alien: Alice environment on the grid. *Journal of Physics: Conference Series*, 119(6):062012, 2008.

[B$^+$11] P. Bartalini et al. Multi-Parton Interactions at the LHC. 2011.

[B$^+$13] Adam Bzdak et al. Initial-state geometry and the role of hydrodynamics in proton-proton, proton-nucleus, and deuteron-nucleus collisions. *Phys. Rev. C*, 87:064906, Jun 2013.

[B^+14] X. Buffat et al. Coherent beam-beam mode in the LHC. In *Proceedings, ICFA Mini-Workshop on Beam-Beam Effects in Hadron Colliders (BB2013)*, pages 227–230, 2014. [,227(2014)].

[Bal11] Renu Bala. Study of D-mesons using hadronic decay channels with the ALICE detector. *Nucl. Phys. Proc. Suppl.*, 210-211:33–36, 2011.

[Bel14] Iouri Belikov. Event reconstruction and particle identification in the ALICE experiment at the LHC. *EPJ Web Conf.*, 70:00029, 2014.

[Bet03] L. Betev. Definition of the ALICE Coordinate System and Basic Rules for Sub-detector Components Numbering. *ALICE-INT-2003-038*, Oct 2003.

[Bet07] Siegfried Bethke. Experimental tests of asymptotic freedom. *Prog. Part. Nucl. Phys.*, 58:351–386, 2007.

[BP97] V. Barger and R. Phillips. *Collider Physics*. Frontiers in physics. Addison-Wesley Publishing Company. ISBN 0-201-14945-1, 1997.

[BR97] R. Brun and F. Rademakers. ROOT: An object oriented data analysis framework. *Nucl. Instrum. Meth.*, A389:81–86, 1997.

[Bur97] P.N. Burrows. PRECISE TESTS OF QCD IN e^+e^- ANNIHILATION. *SLAG-PUB-7434*, March 1997.

[C^+04] P Cortese et al. ALICE: Physics performance report, volume I. *J. Phys.*, G30:1517–1763, 2004.

[C^+07] J M Campbell et al. Hard interactions of quarks and gluons: a primer for lhc physics. *Reports on Progress in Physics*, 70(1):89, 2007.

[C^+12] Serguei Chatrchyan et al. Measurement of the underlying event activity in pp collisions at $\sqrt{s} = 0.9$ and 7 TeV with the novel jet-area/median approach. *JHEP*, 08:130, 2012.

[C^+14] F. Carena et al. The ALICE data acquisition system. *Nucl. Instrum. Meth.*, A741:130–162, 2014.

[CDV$^+$07] Zaida Conesa Del Valle et al. *Performance of the ALICE Muon Spectrometer: Weak Boson Production and Measurement in Heavy-ion Collisions at LHC.* PhD thesis, SUBATECH, Nantes., Nantes, 2007. Presented on 12 Jul 2007.

[CER05] CERN. ALICE at full power. `https://cds.cern.ch/record/816158`, Jan 2005. Cover article.

[CER08] CERN. LHC Machine. *Journal of Instrumentation*, 3(08):S08001, 2008.

[CER15] CERN. Worldwide LHC Computing Grid . `http://wlcg-public.web.cern.ch/tier-centres`, 2015. [Online; accessed 25-January-2016].

[CHS07] John M. Campbell, J. W. Huston, and W. J. Stirling. Hard Interactions of Quarks and Gluons: A Primer for LHC Physics. *Rept. Prog. Phys.*, 70:89, 2007.

[Cic02] C. Cicalo. ALICE Dimuon: Slat chamber prototype under test at PS. `http://cds.cern.ch/record/790000`, Aug 2002. [ALICE Collection.].

[Col82] UA1 Collaboration. Transverse momentum spectra for charged particles at the cern proton-antiproton collider. *Physics Letters B*, 118(1):167 – 172, 1982.

[Col89] UA5 Collaboration. Charged Particle Multiplicity Distributions at 200-GeV and 900-GeV Center-Of-Mass Energy. *Z. Phys.*, C43:357, 1989.

[COL03] Paul COLLIER. Standard Filling Schemes for Various LHC Operation Modes. *LCH-OP-0003 rev 1.0*, Dec 2003.

[Col04] The ALICE Collaboration. *ALICE trigger data-acquisition high-level trigger and control system: Technical Design Report.* Technical Design Report ALICE. CERN, Geneva, 2004.

[Col05] The ALICE Collaboration. Comparison of SPD beam test data with the simulation models in AliRoot. 2005.

[Col08a] The ALICE Collaboration. The ALICE experiment at the CERN Large Hadron Collider. *Journal of Instrumentation*, 3(08):S08002, 2008.

[Col08b] The ALICE Collaboration. The ALICE High Level Trigger . `http://aliceinfo.cern.ch/Public/en/Chapter2/Chap2_HLT.html`, 2008. [Online; accessed 30-January-2016].

[Col08c] The ATLAS Collaboration. The ATLAS Experiment at the CERN Large Hadron Collider. *Journal of Instrumentation*, 3(08):S08003, 2008.

[Col08d] The CMS Collaboration. The CMS experiment at the CERN LHC. *Journal of Instrumentation*, 3(08):S08004, 2008.

[Col08e] The LHCb Collaboration. The LHCb Detector at the LHC. *Journal of Instrumentation*, 3(08):S08005, 2008.

[Col10a] CMS Collaboration. Transverse momentum and pseudorapidity distributions of charged hadrons in pp collisions at $\sqrt{s} = 0.9$ and 2.36 TeV. *JHEP*, 02:041, 2010.

[Col10b] The ALICE Collaboration. Charged-particle multiplicity density at midrapidity in central pb-pb collisions at $\sqrt{s_{NN}} = 2.76$ tev. *Phys. Rev. Lett.*, 105:252301, Dec 2010.

[Col10c] The ALICE Collaboration. Charged-particle multiplicity measurement in proton-proton collisions at $\sqrt{s} = 7$ TeV with ALICE at LHC. *Eur. Phys. J.*, C68:345–354, 2010.

[Col10d] The ALICE Collaboration. Transverse momentum spectra of charged particles in proton-proton collisions at $\sqrt{s} = 900$ GeV with ALICE at the LHC. *Phys. Lett.*, B693:53–68, 2010.

[Col10e] The ATLAS Collaboration. Central charged-particle multiplicities in pp interactions with $|\eta| < 0.8$ and $p_T > 0.5$ and 1 GeV measured with the ATLAS detector at the LHC. Technical Report ATLAS-CONF-2010-101, CERN, Geneva, Dec 2010.

[Col11a] CMS Collaboration. Charged particle multiplicities in pp interactions at $\sqrt{s} = 0.9$, 2.36, and 7 TeV. *JHEP*, 01:079, 2011.

[Col11b] The ALICE Collaboration. Rapidity and transverse momentum dependence of inclusive J/ψ production in pp collisions at $\sqrt{s} = 7$ TeV. *Phys. Lett.*, B704:442–455, 2011. [Erratum: Phys. Lett.B718,692(2012)].

[Col11c] The ATLAS Collaboration. Charged-particle multiplicities in pp interactions measured with the ATLAS detector at the LHC. *New J. Phys.*, 13:053033, 2011.

[Col11d] The ATLAS Collaboration. Charged-particle multiplicities in pp interactions measured with the ATLAS detector at the LHC. *New J. Phys.*, 13:053033, 2011.

[Col12a] CMS Collaboration. Observation of a new boson at a mass of 125 GeV with the CMS experiment at the LHC. *Phys. Lett.*, B716:30–61, 2012.

[Col12b] The ALICE Collaboration. Heavy flavour decay muon production at forward rapidity in proton-proton collisions at. *Physics Letters B*, 708(3-5):265 – 275, 2012.

[Col12c] The ALICE Collaboration. J/ψ Production as a Function of Charged Particle Multiplicity in pp Collisions at $\sqrt{s} = 7$ TeV. *Phys. Lett.*, B712:165–175, 2012.

[Col12d] The ALICE Collaboration. J/ψ suppression at forward rapidity in Pb-Pb collisions at $\sqrt{s_{NN}} = 2.76$ TeV. *Phys. Rev. Lett.*, 109:072301, 2012.

[Col12e] The ALICE Collaboration. Measurement of charm production at central rapidity in proton-proton collisions at $\sqrt{s} = 7$ TeV. *JHEP*, 01:128, 2012.

[Col12f] The ALICE Collaboration. Measurement of charm production at central rapidity in proton-proton collisions at $\sqrt{s} = 2.76$ TeV. *JHEP*, 07:191, 2012.

[Col12g] The ALICE Collaboration. The ALICE Data Acquisition DAQ. `http://aliceinfo.cern.ch/DAQ/`, 2012. [Online; accessed 29-January-2016].

[Col12h] The ALICE Collaboration. Underlying Event measurements in pp collisions at $\sqrt{s} = 0.9$ and 7 TeV with the ALICE experiment at the LHC. *JHEP*, 07:116, 2012.

[Col12i] The ATLAS Collaboration. Measurements of the electron and muon inclusive cross-sections in proton-proton collisions at $\sqrt{s} = 7$ TeV with the ATLAS detector. *Phys. Lett.*, B707:438–458, 2012.

[Col12j] The ATLAS Collaboration. Observation of a new particle in the search for the Standard Model Higgs boson with the ATLAS detector at the LHC. *Phys. Lett.*, B716:1–29, 2012.

[Col13] The ALICE Collaboration. Multiplicity dependence of the average transverse momentum in pp, p-Pb, and Pb-Pb collisions at the LHC. *Phys. Lett.*, B727:371–380, 2013.

[Col14a] The ALICE Collaboration. Beauty production in pp collisions at $\sqrt{s} = 2.76$ TeV measured via semi-electronic decays. *Phys. Lett.*, B738:97–108, 2014.

[Col14b] The ALICE Collaboration. Multiple Parton Interactions with ALICE: from pp to p-Pb. *Journal of Physics: Conference Series*, 535(1):012012, 2014.

[Col15a] LHCb Collaboration. Observation of $\mathrm{J}/\psi\ p$ Resonances Consistent with Pentaquark States in $\Lambda_b^0 \rightarrow \mathrm{J}/\psi\ \mathrm{K}^-\mathrm{p}$ Decays. *Phys. Rev. Lett.*, 115:072001, 2015.

[Col15b] The ALICE Collaboration. Measurement of charm and beauty production at central rapidity versus charged-particle multiplicity in proton-proton collisions at $\sqrt{s} = 7$ TeV. *JHEP*, 09:1–46, 2015.

[Col16a] The ALICE Collaboration. ${}^{3}_{\Lambda}\mathrm{H}$ and ${}^{3}_{\bar{\Lambda}}\overline{\mathrm{H}}$ production in Pb-Pb collisions at $\sqrt{s_{\mathrm{N}N}} =$ 2.76 TeV. *Phys. Lett.*, B754:360–372, 2016.

[Col16b] The ALICE Collaboration. ALICE DCS monitoring. http://alicedcs.web.cern.ch/AliceDCS/monitoring/main.aspx, April 2016. [Online; accessed 19-April-2016].

[Col16c] The ALICE Collaboration. Direct photon production in Pb-Pb collisions at $\sqrt{s_{NN}}$ = 2.76 TeV. *Phys. Lett.*, B754:235–248, 2016.

[Cou04] CERN Courier. Twenty-five years of gluons. http://cerncourier.com/cws/article/cern/29201, Nov 2004.

[Das14] Indranil Das. Charmonia and Bottomonia at pp collision at $\sqrt{s} = 8TeV$. https://indico.cern.ch/event/269667/session/7/contribution/20/

attachments/483514/668683/Autun_Indra_Charmonia_Bottomonia.pdf, July 2014. [Online; accessed 15-March-2016].

[DG+13] Sebastien Descotes-Genon et al. Understanding the $B \to K^* \mu^+ \mu^-$ Anomaly. *Phys. Rev.*, D88:074002, 2013.

[DM16] Cinzia De Melis. The CERN accelerator complex. https://cds.cern.ch/record/2119882, Jan 2016. General Photo.

[FG06] B. Franek and C. Gaspar. Object Oriented Framework for Designing and Implementing Distributed Control Systems . *SLAC-PUB-12067*, Aug 2006.

[GL66] S. Gasiorowicz and P. Langacker. *Elementary particles in physics, ISBN10:0471292877, ISBN13:9780471292876*. John Wiley and Sons Inc., Dec 1966.

[GS04] J.P. Guillaud and A.E. Sobol. Simulation of diffractive and non-diffractive processes at the LHC energy with the PYTHIA and PHOJET MC event generators. pages 1–20, 2004.

[GW73] David J. Gross and Frank Wilczek. Ultraviolet behavior of non-abelian gauge theories. *Phys. Rev. Lett.*, 30:1343–1346, Jun 1973.

[Hal84] Alan. Halzen, Francis; Martin. *Quarks and Leptons An Introductory Course in Modern Particle Physics*. John Wiley & Sons. ISBN 0-471-88741-2, 1984.

[Ian14] Edmond Iancu. QCD in heavy ion collisions. In *Proceedings, 2011 European School of High-Energy Physics (ESHEP 2011)*, pages 197–266, 2014.

[J+12] A Jeff et al. Measurement of Satellite Bunches at the LHC. *Conf. Proc.*, C1205201(CERN-ATS-2012-088):MOEPPB010. 3 p, May 2012.

[K+11] O. Kaczmarek et al. Phase boundary for the chiral transition in (2+1) -flavor QCD at small values of the chemical potential. *Phys. Rev.*, D83:014504, 2011.

[K^+13] Borut Paul Kersevan et al. The Monte Carlo event generator AcerMC versions 2.0 to 3.8 with interfaces to PYTHIA 6.4, HERWIG 6.5 and ARIADNE 4.1. *Computer Physics Communications*, 184(3):919–985, 2013.

[Kon15] Jende. Konrad. When protons collide. http://atlas.physicsmasterclasses.org/en/zpath_protoncollisions.htm, 2015. [Online; accessed 23-January-2016].

[Kou11] Ravjeet Kour. *J/ψ production in proton-proton collisions at ALICE LHC*. PhD thesis, Birmingham U., 2011.

[Lea16] ALICE Shift Leader. training course slides. https://svnweb.cern.ch/cern/wsvn/alicep2/ShiftLeaders/SL_course.pdf, April 2016. [Online; accessed 19-April-2016].

[Lip12] Christian Lippmann. Particle identification. *Nuclear Instruments and Methods in Physics Research Section A: Accelerators, Spectrometers, Detectors and Associated Equipment*, 666:148 – 172, 2012. Advanced Instrumentation.

[Man12] Vito Manzari. The present Inner Tracking System - Steps forward! http://alicematters.web.cern.ch/sites/alicematters.web.cern.ch/files/images/ITS.jpg, December 2012. [Online; accessed 18-April-2016].

[Mar15] M. Marchisone. Muon production vs charged particle multiplicity: pile-up and normalization. https://indico.cern.ch/event/449946/contributions/1112116/attachments/1162494/1674429/30Sep2015_pagHFM.pdf, 2015. [Online; accessed 30-January-2016, private communication].

[Max06] C. J. Maxwell. Perturbative and non-perturbative QCD. *eConf*, C0605151:0002, 2006.

[MCN98] M. Greco M. Cacciari and P. Nason. The p_T spectrum in heavy-flavour hadroproduction. http://www.lpthe.jussieu.fr/~cacciari/fonll/fonllform.html, 1998. [Online; accessed 30-January-2016].

[Mil10] Leonardo Milano. Vertex and track reconstruction with the ALICE Inner Tracking System. `http://personalpages.to.infn.it/~milano/presentations/LeonardoMilano_LHCBeyond.pdf`, 2010. [Online; accessed 2-May-2016].

[Mou14] Philippe Mouche. Overall view of the LHC. Vue d'ensemble du LHC. `https://cds.cern.ch/record/1708847`, Jun 2014. General Photo.

[Mul08] Aurelien Muller. The ALICE Dimuon Spectrometer. `http://aliceinfo.cern.ch/Public/en/Chapter2/Chap2_dim_spec.html`, 2008. [Online; accessed 18-April-2016].

[N$^+$08] Pavel M. Nadolsky et al. Implications of CTEQ global analysis for collider observables. *Phys. Rev.*, D78:013004, 2008.

[P$^+$02] J. Pumplin et al. New generation of parton distributions with uncertainties from global QCD analysis. *JHEP*, 07:012, 2002.

[PI15] Physik-Institut. Standard Model. `http://www.physik.uzh.ch/groups/serra/StandardModel.html#top`, 2015. [Online; accessed 13-April-2016].

[Pol73] H. David Politzer. Reliable perturbative results for strong interactions? *Phys. Rev. Lett.*, 30:1346–1349, Jun 1973.

[RES05a] CERN EUROPEAN ORGANIZATION FOR NUCLEAR RESEARCH. FLUKA: A Multi-Particle Transport Code. *CERN-2005-010*, 2005.

[RES05b] CERN EUROPEAN ORGANIZATION FOR NUCLEAR RESEARCH. LHC Computing Grid Technical Design Report. *CERN-LHCC-2005-024. ISBN-92-9083-253-3*, June 2005.

[R.G14] R.Grosso. The Offline Conditions DB framework. `http://aliweb.cern.ch/Offline/Activities/ConditionDB.html#SimulReco.`, 2014. [Online; accessed 26-April-2016].

[S$^+$06] T Sjostrand et al. PYTHIA 6.4 Physics and Manual. *JHEP*, 05:026, 2006.

[S$^+$07] Frixione Stefano et al. Matching NLO QCD computations with Parton Shower simulations: the POWHEG method. *JHEP*, 11:070, 2007.

[San11] R. Santoro. Performance of the ALICE silicon detectors . https://indico.cern.ch/event/104062/contributions/23123/attachments/13979/20370/santoro_vertex2011.pdf, 2011. [Online; accessed 06-May-2016].

[Shi98] Mikhail A. Shifman. Snapshots of hadrons or the story of how the vacuum medium determines the properties of the classical mesons which are produced, live and die in the QCD vacuum. *Prog. Theor. Phys. Suppl.*, 131:1–71, 1998.

[Sin16] Vikas. Singhal. ALICE GRID and Kolkata Tier-2 . http://docplayer.net/3090488-Alice-grid-kolkata-tier-2.html, 2016. [Online; accessed 26-January-2016].

[StAc13] Kyrre Skjerdal and the ALICE collaboration. Photoproduction of ρ^0 in ultra–peripheral nuclear collisions at ALICE. *J. Phys. Conf. Ser.*, 455:012010, 2013.

[Vel03] M. Veltman. World Scientific. *ISNB 918-238-149-X*, pages 45–47, 2003.

[Vog08] R. Vogt. The Total charm cross-section. *Eur. Phys. J. ST*, 155:213–222, 2008.

[WD06] F. Wilczek and B Devine. World Scientific. *ISNB 981-256-649- X*, page 400, 2006.

[Wie10] Urs Achim Wiedemann. Jet Quenching in Heavy Ion Collisions. pages 521–562, 2010. [Landolt-Bornstein23,521(2010)].

[Yul02] T. Yulsman. CRS Press. *ISNB 0-7503-0765-X*, page 55, 2002.

[Z$^+$12] X Zhang et al. *Study of Heavy Flavours from Muons Measured with the ALICE Detector in Proton-Proton and Heavy-Ion Collisions at the CERN-LHC*. PhD thesis, Clermont-Ferrand U., 2012. presented 23 May 2012.

[Zer14] Dirk Zerwas. Search for higgs and supersymmetry. *Journal of Physics: Conference Series*, 485(1):012011, 2014.

APPENDIX A

RUNLISTS, ANALYSIS TASKS AND SIMULATION MACROS

A.1 Runlists

A.1.1 LHC12h

192732 192731 192729 192727 192724 192548 192542 192535 192534 192533 192531 192510 192505 192499 192492 192471 192468 192264 192246 192244 192242 192205 192202 192201 192200 192199 192197 192194 192192 192190 192177 192174 192172 192171 192166 192141 192140 192136 192128 192120 192119 192117 192095 192073 192072 192067 192004 192003 191996 191539 191527 191521 191485 191451 191450 191448 191447 191443 191344 191343 191340 191337 191329 191309 191307 191275 191248 191247 191245 191244 191242 191234 191232 191231 191230 191229 191227 191224 191222 191217 191163 191159 191129 191121 191110 191105 191083 191079 191032 191022 190984 190983 190981 190979 190970 190969 190968 190960 190904 190903 190898 190895 190894 190879 190870 190866 190864 190848 190844 190822 190821 190819 190818 190815 190714 190712 190685 190683 190585 190581 190578 190561 190541 190540 190535 190521 190517 190495 190493 190419 190418 190417 190416 190414 190413 190407 190393 190392 190390 190389 190388 190386 190380 190379 190374 190342 190341 190340 190337 190336 190330 190325 190324 190307 190305 190304 190302 190301 190299 190296 190244 190242 190240 190239 190237 190235 190216 190215 190214 190212 190209 190206 190150 190147 190142 190141 190138 190136 190119 190118 190117 190116 190115 190113 190112 190110 190057 190050 189737 189736 189735 189734 189729 189728 189725 189698 189697 189696 189694 189687 189685 189659 189658 189656 189654 189650 189648 189647 189642 189641 189623 189621 189616 189612 189611 189610 189608 189607 189605 189603 189601 189596 189578 189577 189576

A.1.2 LHC12i

193341 193339 193295 193276 193274 193270 193243 193240 193236 193179 193144 193141 193084 193079 193051 193049 193047 193046 193044 193014 193011 193010 193008 193007 193005 193004 193000 192824 192822 192820 192816 192813 192811 192808 192806 192796 192779 192778 192775 192772 192765 192762 192750 192747 192745

A.2 Analysis Tasks

The analysis task used to obtain the p_T and multiplicity distributions is shown below.

A.2.1 AliAnalysisTaskPtCMSH.cxx

```

#include "TChain.h"
#include "TTree.h"
#include "TH1F.h"
#include "TH1D.h"
#include "TH2F.h"
#include "TAxis.h"
#include "TRandom3.h"
#include "TStyle.h"
#include "TLegend.h"
#include "THnSparse.h"
#include "TCanvas.h"
#include "TFile.h"
#include "AliAnalysisTask.h"
#include "AliAnalysisManager.h"
#include "AliAODEvent.h"
#include "AliESDEvent.h"
#include "AliAODTrack.h"
#include "AliESDInputHandler.h"
#include "AliAODInputHandler.h"
#include "AliMuonTrackCuts.h"
#include "AliMuonEventCuts.h"
#include "AliAnalysisTaskPtCMSH.h"
#include "AliAODTracklets.h"
#include "AliMultiplicity.h"
#include "AliAnalysisTaskMuonCollisionMultiplicity.h"
#include "AliCounterCollection.h"
// example of an analysis task creating a p_t spectrum
// Authors: Panos Cristakoglou, Jan Fiete Grosse-Oetringhaus,
// Christian Klein-Boesing
// Reviewed: A.Gheata (19/02/10)

ClassImp(AliAnalysisTaskPtCMSH)


AliAnalysisTaskPtCMSH::AliAnalysisTaskPtCMSH(const char *name, TH1D *hinput)
  : AliAnalysisTaskSE(name),
  ftrclasses(0),
```

```
  fAOD(0),
  fOutputList(0),
  fNtracklets(0),
  fHn(0),
  fMuonTrackCuts(0),
  fMuonEventCuts(0),
  hmultprofile(0),
  fEventCounter(0)
  {
  // Constructor
    if( hinput ) hmultprofile = new TH1D(*hinput);

    Nrand = new TRandom3();

  fMuonTrackCuts = new AliMuonTrackCuts(Form("TrackCuts_%s",name),"TrackCuts");

  fMuonEventCuts = new AliMuonEventCuts(Form("EventCuts_%s",name),"event");


  DefineInput(0, TChain::Class());
  // Output slot #0 id reserved by the base class for AOD
  // Output slot #1 writes into a TH1 container
  DefineOutput(1, TList::Class());
}



void AliAnalysisTaskPtCMSH::UserCreateOutputObjects()

{
  // Create histograms
  fOutputList = new TList();
  fOutputList->SetOwner();

  fEventCounter = new AliCounterCollection("EventCounter");
  fEventCounter->AddRubric("event","MUON/ANY");
  fEventCounter->AddRubric("trigger",10000);
  fEventCounter->AddRubric("run",100000);
  fEventCounter->Init();

  int bins[kNvars]    ={100,60,80,300,2};
  double min[kNvars] ={0.,-6.,-10,-0.5,-2};
  double max[kNvars] ={100.,6.,10,299.5,2};

  fNtracklets = new TH2F("Ntracklets","Ntracklets",bins[2],min[2],max[2],bins[3],
```

```
  min[3],max[3]);
  fHn = new THnSparseD("hn","hn",kNvars,bins,min,max);

  fOutputList->Add(fHn);
  fOutputList->Add(fNtracklets);
  fOutputList->Add(fEventCounter);

  PostData(1, fOutputList);
}

void AliAnalysisTaskPtCMSH::NotifyRun()
{
  fMuonTrackCuts->SetRun(fInputHandler);
}


void AliAnalysisTaskPtCMSH::UserExec(Option_t *)
{
  // Main loop
  // Called for each event

  if (! fMuonEventCuts->IsSelected(fInputHandler)) return;

  // retrive the AOD event
  fAOD = dynamic_cast<AliAODEvent*>(InputEvent());
  if (!fAOD) {
    printf("ERROR: fAOD not available\n");
    return;
  }

  // trigger classes selection
  TString trclasses = fAOD->GetFiredTriggerClasses();
  if( ! trclasses.Contains(ftrclasses) ) return;

  //count events
  fEventCounter->Count(Form("event:MUON/trigger:%s/run:%d",trclasses.Data(),
  fCurrentRunNumber));

  // check for a good vertex
  const AliAODVertex* trkVtx = fAOD->GetPrimaryVertex();
  if (!trkVtx || trkVtx->GetNContributors()<=0) return;
  TString vtxTtl = trkVtx->GetTitle();
  if (!vtxTtl.Contains("VertexerTracks")) return;

```

```
AliAODVertex *vz = fAOD->GetPrimaryVertexSPD();
if (vz->GetNContributors()<=0) return;
TString vtxTyp = vz->GetTitle();
Double_t cov[6]={0};
vz->GetCovarianceMatrix(cov);

Double_t zRes = TMath::Sqrt(cov[5]);
// resolution cut
if (vtxTyp.Contains("vertexer: Z") && (zRes>0.25)) return;
//difference between the main vertex and the SPD
if (TMath::Abs(trkVtx->GetZ() - vz->GetZ())>0.5) return;

if ( vz->GetZ() < -10. || vz->GetZ() > 10. ) return;

// count the tracklet multiplicity
Int_t multiplicity = 0;

AliAODTracklets *tracklets = fAOD->GetTracklets();

Int_t nTracklets = tracklets->GetNumberOfTracklets();
for (Int_t nn = 0; nn < nTracklets; nn++)
{
  // consider only tracklets in the good eta range
  Double_t theta = tracklets->GetTheta(nn);
  Double_t eta = -TMath::Log(TMath::Tan(theta/2.0));
  if ( TMath::Abs(eta) > 1.0) continue; // Eta Cut implemented here

  multiplicity += 1;
}
// end tracklets loop
if ( multiplicity < 1 ) return; // skip event with 0 tracklets


// correction for the SPD acceptance
// if hmultprofile is not present the correction is not applied
double corrfactor = 1.;
if( hmultprofile) corrfactor = hmultprofile->GetMaximum()/hmultprofile->
GetBinContent(hmultprofile->FindBin( vz->GetZ() ));

cout << "Nref = " << hmultprofile->GetMaximum() << endl;

//poisson randomization

//difference between corrected and the measured number of tracklets
double deltaN = (corrfactor * multiplicity) - multiplicity;
```

```
  //cout << deltaN << endl;
  //computes number of missing tracklets
  //TRandom *Nrand = new TRandom();
  int missingtracklets = Nrand->Poisson(deltaN);
  cout << "Number of missing tracklets = " << missingtracklets << endl;

  int corrmult = multiplicity + missingtracklets;//corrected number of tracklets
  // fill the multiplicity vs vertex histogram
  if(corrmult < 0) corrmult = 0;
  fNtracklets->Fill(vz->GetZ(),corrmult);


  // informations about muons

  // create data array used to fill the THnSparse fHn
  Double_t data[kNvars];

  data[kMult] = corrmult;
  data[kVz]    = vz->GetZ();

  bool aretheregoodmuons = kFALSE;
  for ( Int_t iTracks = 0; iTracks < fAOD->GetNumberOfTracks(); iTracks++ ) {
    AliAODTrack* track = dynamic_cast<AliAODTrack*>(fAOD->GetTrack(iTracks));
    if (!track) {
      printf("ERROR: Could not receive track %d\n", iTracks);
      continue;
    }

    if (!fMuonTrackCuts->IsSelected(track)) continue;

    data[kPt]     = track->Pt();
    data[kEta]   = track->Eta();
    data[kCharge] = track->Charge()/3;
    aretheregoodmuons = kTRUE;

    // fill for _each_ muon
    //*******************
    fHn->Fill(data);
  }// end loop on AOD tracks

  PostData(1, fOutputList);
}

 void AliAnalysisTaskPtCMSH::Terminate(Option_t *)
{
```

```
TString naming = this->GetName();
naming.Resize( naming.First("_") );

// prepare string for naming stuff
TString name;

// retrieve the output list
fOutputList = dynamic_cast<TList*> (GetOutputData(1));
if (!fOutputList) {
  printf("ERROR: Output list not available\n");
  return;
}

SetStyle(kFALSE);

// get output histograms/containers from the list
fNtracklets = (TH2F*)fOutputList->FindObject("Ntracklets");
fEventCounter = (AliCounterCollection*)fOutputList->FindObject("EventCounter");
fHn = (THnSparse*)fOutputList->FindObject("hn");

// print event conter information
fEventCounter->Print("event");

// Tracklet multiplicity vs Vertex position
name = naming + "_Multip";
TCanvas *c6 = new TCanvas(name.Data(),name.Data(), 10,10,510,510);
c6->cd(1)->SetLogz();
fNtracklets->GetXaxis()->SetTitle("Vertex (cm)");
fNtracklets->GetYaxis()->SetTitle("Number of tracklets ");
fNtracklets->GetYaxis()->SetTitleOffset(1);
fNtracklets->GetXaxis()->CenterTitle(1);
fNtracklets->Draw("colz");
fNtracklets->SaveAs(Form("%s_2D.root",naming.Data()));


name = naming + "_hprof";
TH1D *hp = new TH1D(name.Data(), "hp",80, -10,10);

double mean = 0;
TH1D* h1;
for(int j = 0; j<80;j++){
  h1 = (TH1D*)fNtracklets->ProjectionY("_px",j+1,j+1,"");
  h1->SetName(Form("%i",j));
  mean = h1->GetMean(1);
  hp->SetBinContent(j+1,mean);
```

```
}
hp->SetLineColor(kBlack);
hp->Draw("same");

hp->SaveAs(Form("%s_fproj.root",naming.Data()));

// Tracklet multiplicity distribution
name = naming + "_multiplicity";
TCanvas *c1 = new TCanvas(name.Data(), name.Data(), 10,10,510,510);
c1->cd(1)->SetLogy();

TH1D* hist1 = fNtracklets->ProjectionY();
name = naming + "_h_multiplicity";
hist1->SetName(name.Data());
hist1->SetTitle("Tracklet multiplicity");

hist1->GetXaxis()->SetTitle("Ntracklets");
hist1->GetYaxis()->SetTitle("Number of Events");
hist1->GetYaxis()->SetTitleOffset(1.5);
hist1->GetXaxis()->SetTitleOffset(1.0);
hist1->GetXaxis()->CenterTitle(1);
hist1->Draw("");

hist1->SaveAs(Form("%s_multi.root",naming.Data()));

// vertex distribution
name = naming + "_vertex";
TCanvas *ccc = new TCanvas(name.Data(), name.Data(), 10,10,510,510);
ccc->cd(1)->SetLogy();

TH1D* histvz = fNtracklets->ProjectionX();
name = naming + "_h_vertex";
histvz->SetName(name.Data());
histvz->SetTitle("vertex distribution");

histvz->GetXaxis()->SetTitle("vertex position (cm)");
histvz->GetYaxis()->SetTitle("Entries");
histvz->GetYaxis()->SetTitleOffset(1.5);
histvz->GetXaxis()->SetTitleOffset(1.0);
histvz->GetXaxis()->CenterTitle(1);
histvz->Draw();

// muon pT distribution
name = naming + "_canvas_pT";
TCanvas *c12 = new TCanvas(name.Data(), name.Data(), 10,10,510,510);
```

```
c12->cd(1)->SetLogy();
//fHn = (THnSparse*)fOutputList->FindObject("hn");
fHn->GetAxis(kMult)->SetRangeUser(0,300);


name = naming + "_transverse_momentum";
TH1D* hist2 = fHn->Projection(kPt, name.Data()); // give proper name
hist2->GetXaxis()->SetTitle("Pt (GeV/c)");
hist2->GetYaxis()->SetTitle("dN/dPt (c/GeV)");
hist2->GetYaxis()->SetTitleOffset(1.5);
hist2->GetXaxis()->SetTitleOffset(1.0);
hist2->GetXaxis()->CenterTitle(1);

hist2->Draw("E1");
hist2->SaveAs(Form("%s_corrpt.root",naming.Data()));

// muon Yield vs multiplicity
Int_t multLimits[] = {0,7,10,13,17,22, 27, 34, 300};
const Int_t kNumMultLimit = 8; // the number of multiplicity bins + 1

//defining the pT integration limits
Float_t pTmin = 6.;  // in GeV/c
Float_t pTmax = 20.;  // in GeV/c

Int_t pTbinMin = fHn->GetAxis(kPt)->FindBin(pTmin);
Int_t pTbinMax = fHn->GetAxis(kPt)->FindBin(pTmax);

// let's plot them all together
name = naming + "_canvas_pT_in_mult_bins";
TCanvas *c13 = new TCanvas(name.Data(),
"pT distributions in different multiplicity bins", 10,10,510,510);
c13->cd(1)->SetLogy();

// we need an empty frame where to draw the various pT projection with "same"
TH1 *hframe = c13->cd(1)->DrawFrame(0.,0.9,80.,
hist2->GetMaximum(),naming.Data() );

 // here the loop on the foreseen multiplicity bins starts.
 for( int imult = 0; imult < kNumMultLimit; imult++){

   // definition of the multiplicity limits
   Int_t minMultLimit = multLimits[imult]+1;
   // value in the array at position imult+1
   Int_t maxMultLimit = multLimits[imult+1];

```

```
      // setting the range for the kMult axis
      fHn->GetAxis(kMult)->SetRangeUser( minMultLimit, maxMultLimit);

      TH1D* hist3 = fHn->Projection(kPt, Form("%s_pt_mult_%d",naming.Data(),imult));
      hist3->SetLineColor( imult+1);
      hist3->Draw("esame");

      double integral1 =  hist3->Integral( pTbinMin, pTbinMax);
      cout << "integral("<< minMultLimit << "< Mult <" << maxMultLimit<<") = "
       << integral1 << endl;

    }

  }

  void AliAnalysisTaskPtCMSH::SetStyle(Bool_t graypalette) {
  cout << "Setting style!" << endl;

  gStyle->Reset("Plain");
  gStyle->SetOptTitle(1);
  gStyle->SetOptStat(1);
  gStyle->SetStatY(0.9);
  gStyle->SetStatX(0.85);
  gStyle->SetStatW(0.4);
  gStyle->SetStatH(0.2);
  if(graypalette) gStyle->SetPalette(8,0);
  else gStyle->SetPalette(1);
  gStyle->SetCanvasColor(10);
  gStyle->SetCanvasBorderMode(0);
  gStyle->SetFrameLineWidth(1);
  gStyle->SetFrameFillColor(kWhite);
  gStyle->SetPadColor(10);
  gStyle->SetPadTickX(1);
  gStyle->SetPadTickY(1);
  gStyle->SetPadBottomMargin(0.15);
  gStyle->SetPadRightMargin(0.15);
  gStyle->SetPadLeftMargin(0.15);
  gStyle->SetHistLineWidth(1);
  gStyle->SetHistLineColor(kRed);
  gStyle->SetFuncWidth(2);
  gStyle->SetFuncColor(kGreen);
  gStyle->SetLineWidth(2);
  gStyle->SetLabelSize(0.045,"xyz");
  gStyle->SetLabelOffset(0.01,"y");
  gStyle->SetLabelOffset(0.01,"x");
```

```
  gStyle->SetLabelColor(kBlack,"xyz");
  gStyle->SetTitleSize(0.05,"xyz");
  gStyle->SetTitleOffset(2.5,"y");
  gStyle->SetTitleOffset(2.2,"x");
  gStyle->SetTitleFillColor(kWhite);
  gStyle->SetTextSizePixels(26);
  gStyle->SetTextFont(42);
  gStyle->SetErrorX();
  gStyle->SetEndErrorSize();
  gStyle->SetLegendBorderSize(0);
  gStyle->SetLegendFillColor(kWhite);
  gStyle->SetLegendFont(42);
}
```

The plugins used to run the analysis task on the ALICE Environment (ALIEN) grid where the analysis is done. These plugins: CreateAlienHandler.C, the runGrid.C connect the user task (analysis task) to the grid and enables the user to define the versions of the analysis packages as well as the physics libraries to be used. And the AddTask.C is a small execution macro responsible for registering the task to an analysis manager and collects input and output files, connects everything to the manager.

A.2.2 CreateAlienHandler.C

```
AliAnalysisGrid* CreateAlienHandler()
{
  AliAnalysisAlien *plugin = new AliAnalysisAlien();
  // Set the run mode (can be "full", "test", "offline", "submit" or "terminate")
  plugin->SetRunMode("terminate");

  // Set versions of used packages
  plugin->SetAPIVersion("V1.1x");
  plugin->SetROOTVersion("v5-34-08-7");
  plugin->SetAliROOTVersion("v5-06-12");
  plugin->SetAliPhysicsVersion("vAN-20150410");


  // Analysis on grid
  // Define production directory LFN
  plugin->SetGridDataDir("/alice/data/2012/LHC12i/");

  plugin->SetRunPrefix("000");
  plugin->SetDataPattern("*ESDs/muon_calo_pass2/AOD/*/AliAOD.root");
  const char *runListName = "Runlist140.txt";
  if(!runListName) {
  cout << "run list file name does not exist... stop now!" <<endl;
  return NULL;
  }
      ifstream runListFile;
      runListFile.open((char*)runListName);
      Int_t runNr;
      if (runListFile.is_open()) {
        while (kTRUE){
    runListFile >> runNr;
    if(runListFile.eof()) break;
    cout<<runNr<<"\n";
    plugin->AddRunNumber(runNr);
```

```
        }
  }
    else {
        cout << "run list file "<<runListName<<" does not exist...
        stop now!" <<endl; return NULL;
  }
   runListFile.close();

   // Define alien work directory where all files will be copied.
   plugin->SetGridWorkingDir("multiplicity_task_
   LHC_12i_T0_ChangingBins2_corrected140");
   plugin->SetFileForTestMode("data.txt");
   //Declare alien output directory. Relative to working directory.
   plugin->SetGridOutputDir("ChangingBins_corrected22");

   plugin->SetProofDataSet("/alice/data/LHC11h_000169554_p1_muon_AOD_AliAODs");
   plugin->SetAnalysisSource("AliAnalysisTaskPtCMSH.cxx");

  plugin->SetAdditionalLibs
  ("libCORRFW.so libPWGmuon.so AliAnalysisTaskPtCMSH.h AliAnalysisTaskPtCMSH.cxx");

  plugin->SetAnalysisMacro("MyAnalysis.C");
  plugin->AddIncludePath("-I.");
  plugin->AddIncludePath("-I$ALICE_ROOT/include");
  plugin->AddIncludePath("-I$ALICE_PHYSICS/include");
  plugin->SetNtestFiles(1);
  plugin->SetOutputToRunNo();
  //plugin->SetMergeViaJDL();
  return plugin;
}
```

A.2.3 runGrid.C

```
void runGrid()
{
  // Load common libraries
  gSystem->Load("libCore.so");
  gSystem->Load("libTree.so");
  gSystem->Load("libGeom.so");
  gSystem->Load("libVMC.so");
  gSystem->Load("libPhysics.so");
  gSystem->Load("libMinuit.so");
  gSystem->Load("libSTEERBase");
  gSystem->Load("libESD");
  gSystem->Load("libAOD");
  gSystem->Load("libANALYSIS");
  gSystem->Load("libANALYSISalice");
  gSystem->Load("libCORRFW");
  gSystem->Load("libPWGmuon");
  // Use AliRoot includes to compile our task
  gROOT->ProcessLine(".include $ALICE_ROOT/include");
  gROOT->ProcessLine(".include $ALICE_PHYSICS/include");
  gSystem->AddIncludePath("-I.");

  // Create and configure the alien handler plugin
  gROOT->LoadMacro("CreateAlienHandler.C");
  AliAnalysisGrid *alienHandler = CreateAlienHandler();
  if (!alienHandler) return;

  // Create the analysis manager
  AliAnalysisManager *mgr = new AliAnalysisManager("testAnalysis");

  // Connect plug-in to the analysis manager
  mgr->SetGridHandler(alienHandler);

  gROOT->LoadMacro("AliAnalysisTaskPtCMSH.cxx++g");

  AliAODInputHandler* aodH = new AliAODInputHandler();
  aodH->SetCheckStatistics(kTRUE);
  mgr->SetInputEventHandler(aodH);
  gROOT->LoadMacro("AddTask.C");


  AddTask( "CMSH8-S-NOPF-MUON", kFALSE );
  AddTask( "CINT8-S-NOPF-ALLNOTRD", kFALSE );

```

```
   // Enable debug printouts
   mgr->SetDebugLevel(0);


   if (!mgr->InitAnalysis())
     return;

   mgr->PrintStatus();
   // Start analysis
   mgr->StartAnalysis("grid terminate"); // Use this for grid
   //mgr->StartAnalysis("proof"); // Use this for proof

 };

```

A.2.4 AddTask.C

```
#if !defined(__CINT__) || defined(__MAKECINT__)
#include "TString.h"

#include "AliAnalysisManager.h"
#include "AliAnalysisDataContainer.h"

#include "AliMuonTrackCuts.h"
#include "AliMuonEventCuts.h"
#include "AliAnalysisTaskPtCMSH.h"
#endif
AliAnalysisTaskPtCMSH *AddTask(TString trigger, Bool_t useMC){

AliAnalysisManager *mgr = AliAnalysisManager::GetAnalysisManager();
 if (!mgr) {
  ::Error("AddtaskSingleMu", "No analysis manager to connect to.");
  return NULL;
  }

  // open input file
  TFile *inf = TFile::Open("/home/nomvelo/Nomvelo/
  NewAnalysis_Changing_bins/Raw/140/CINT8_fproj.root");
 TH1D *hinputprofile = (TH1D*) inf->Get("CINT8_hprof");
  hinputprofile = (TH1D*) hinputprofile->Clone("profile");
```

```
hinputprofile->SetDirectory(0);
inf->Close();

//  my task
TString naming = trigger;
naming.ReplaceAll("-","_");
AliAnalysisTaskPtCMSH *task =
new AliAnalysisTaskPtCMSH(Form("%s_Task",naming.Data()), hinputprofile);

// specific setting for task
//track cuts settings
Bool_t isMC = kFALSE;
task->GetMuonTrackCuts()->
SetFilterMask
( AliMuonTrackCuts::kMuEta
|AliMuonTrackCuts::kMuThetaAbs
| AliMuonTrackCuts::kMuPdca
| AliMuonTrackCuts::kMuMatchHpt);

task->GetMuonTrackCuts()->SetIsMC(useMC);
task->GetMuonTrackCuts()->Print("mask");
task->GetMuonTrackCuts()->SetPassName("muon_calo_pass2");
task->GetMuonTrackCuts()->SetAllowDefaultParams(kTRUE);
task->GetMuonTrackCuts()->ApplySharpPtCutInMatching(kTRUE);


// event cuts settings
task->GetMuonEventCuts()->SetFilterMask ( AliMuonEventCuts::kPhysicsSelected |
AliMuonEventCuts::kSelectedTrig |
AliMuonEventCuts::kGoodVertex );

task->GetMuonEventCuts()->SetVertexMinNContributors(1);
task->GetMuonEventCuts()->SetVertexVzLimits(-10., 10.);
task->GetMuonEventCuts()->SetTrigClassPatterns(trigger.Data(),"0MSH:13");


mgr->AddTask(task);

AliAnalysisDataContainer *cinput = mgr->GetCommonInputContainer();

AliAnalysisDataContainer *coutput3 = mgr->
CreateContainer(Form("chist_%s",naming.Data()), TList::Class(),
AliAnalysisManager::kOutputContainer, Form("MSH_corr.root:%s",naming.Data()));


```

```
  mgr->ConnectInput(task, 0, cinput);

  mgr->ConnectOutput(task, 1, coutput3);

  return task;
}
```

Below are the simulation macros used to reproduce the p_T distribution which would be obtained if the Muon spectrometer was 100 % efficient. together with the reconstruction macro used to reproduce the p_T shape taking into account the actual detector conditions on a run by run basis for pp collisions at 8 TeV in 2012.

A.3 simulation macros

A.3.1 GenParamCustomSingleForHF2.C

This is the generator for the heavy flavour single muons, using as inputs the parameters (p0 - p7) obtained from the fit functions obtained from the FONNL simulations.

```
#if !defined(__CINT__) || defined(__MAKECINT__)
#include <Riostream.h>
#include "TRandom.h"
#include "AliGenerator.h"
#include "AliGenParam.h"
#endif


static Int_t IpMuon( TRandom *ran);
static Double_t PtMuon( const Double_t *px, const Double_t * /*dummy*/ );
static Double_t YMuon( const Double_t *py,  const Double_t * /*dummy*/ );
static Double_t V2Muon( const Double_t *pv, const Double_t * /*dummy*/ );

 AliGenerator* GenParamCustomSingleForHF2()
{
 AliGenParam *singleMu = new AliGenParam(1,-1,PtMuon,YMuon,V2Muon,IpMuon);
 singleMu->SetMomentumRange(0,1e6);
 singleMu->SetPtRange(4.,40.);
 singleMu->SetYRange(-4.5, -2.);
 singleMu->SetPhiRange(0., 360.);
 singleMu->SetForceDecay(kNoDecay);
 singleMu->SetTrackingFlag(1);
 return singleMu;
}

 Int_t IpMuon(TRandom *ran)
{
 // muon composition
```

```
  if (ran->Rndm() < 0.5 )
  {
    return 13;
  }
  else
  {
    return -13;
  }
}

  Double_t PtMuon( const Double_t *px, const Double_t * /*dummy*/ )
 {
  // muon pT

  Double_t x=*px;
  if( x < 1. ) return 0.;
  Float_t p0,p1,p2,p3, p4, p5, p6, p7; /*p8;*/

  p0 = 361.736;
  p1 = -0.372774;
  p2 = -0.254151;
  p3 = 0.279416;
  p4 = 4.55285;
  p5 = 11962.8;
  p6 = 207419;
  p7 = 1591.83;

  // norm
  Float_t norm = p0;
  //slope
  Float_t slope = p1 * ( 1. - TMath::Exp( p2*x)) + p3;
  //double
  Float_t den = 1./TMath::Power(x,p4);
  // pol
  Float_t pol = p5 + p6*x+p7*x*x;

  return norm * TMath::Exp( slope*x ) * den * pol;
 }

  Double_t YMuon( const Double_t *py, const Double_t */*dummy*/ )
 {
  // muon y

 //Float_t yswitch = VAR_GENPARAMCUSTOMSINGLE_Y_RAPIDITY_SWITCH;
  Double_t x = *py;
```

```
 //pol4 only valid in y= -4;-2.5
 Float_t p0,p1,p2,p3, p4, p5/*, p6, p7, p8*/;

 p0 = 4.25146e+06;
 p1 = -2.12906;
 p2 = -245711;
 p3 = 1936.69;
 p4 = 114.396;
 p5 = -1.91095;



 }

 Double_t V2Muon( const Double_t */*dummy*/, const Double_t */*dummy*/ )
{
 return 0.;
}
```

A.3.2 rec.C

This macro runs the reconstruction. It takes into account the configuration of the Muon tracking Chambers from the OCDB and takes into alignment in 2012.

```

void rec()
{
  AliReconstruction reco;
  reco.SetRunQA("MUON:ALL");

  reco.SetCleanESD(kFALSE);
  reco.SetStopOnError(kFALSE);

  reco.SetDefaultStorage("raw://");

  if ( 0 )
  {
    reco.SetRunReconstruction("VZERO T0 MUON ITS FMD");
  }
  else
  {
    reco.SetRunReconstruction("MUON");
  }
  AliCDBManager* man = AliCDBManager::Instance();
  man->SetDefaultStorage("alien://folder=/alice/data/2012/OCDB");
  man->SetSpecificStorage("GRP/GRP/Data",Form("local://%s",gSystem->pwd()));
  man->SetSpecificStorage("MUON/Align/Data",
  "alien://folder=/alice/simulation/2008/v4-15-Release/Residual");
  man->SetSpecificStorage("MUON/Calib/RecoParam",
  "alien://folder=/alice/data/2012/OCDB",5,0);

  reco.SetRunPlaneEff(kTRUE);
  reco.SetUseTrackingErrorsForAlignment("ITS");

  // ITS

  reco.SetSpecificStorage("ITS/Align/Data","alien://folder=
  /alice/simulation/2008/v4-15-Release/Residual");
  reco.Run();
}
```

A.3.3 sim.C

This macro runs the simulation.

```

  void sim(Int_t nev=3000)
  {

  #if defined(__CINT__)
  // Parton density functions
  gSystem->Load("liblhapdf");
  if ( TString("GenParamCustomSingleForHF2").Contains
  ("pythia6",TString::kIgnoreCase) )
  {
    std::cout << "Setting up Pythia6 required env. variables" << std::endl;
    gSystem->AddIncludePath("-I$ALICE_ROOT/include");

  }
  else  gSystem->Load("libpythia6");     // Pythia 6.2 (for decayer)

  if ( TString("GenParamCustomSingleForHF2").Contains("pythia8",TString::kIgnoreCase) )
  {
    std::cout <<
    "Setting up Pythia8 required libraries and env. variables" << std::endl;
     gSystem->AddIncludePath("-I$ALICE_ROOT/include");

  }
#endif


  if ( 0) {
  TGeoGlobalMagField::Instance()->
  SetField(new AliMagF("Maps","Maps", -1., -1, AliMagF::k5kG));
  }

  AliSimulation simulator;
  simulator.SetRunQA("MUON:ALL");
  simulator.SetRunHLT("");

  if ( 0 )
  {
    // T0 and VZERO for trigger efficiencies, FMD for diffractive studies
    simulator.SetMakeSDigits("MUON T0 VZERO FMD");
    // ITS needed to propagate the simulated vertex
    simulator.SetMakeDigitsFromHits("ITS");
    simulator.SetMakeDigits("MUON T0 VZERO FMD");););
```

```
  }
  else
  {
    simulator.SetTriggerConfig("MUON");
    simulator.SetMakeSDigits("MUON");
    // ITS needed to propagate the simulated vertex
    simulator.SetMakeDigits("MUON"););
  }


  simulator.SetDefaultStorage("raw://");

  if ( kFALSE )
  {
    simulator.SetCDBSnapshotMode("OCDB_sim.root");
  }

  if ( !0 ) {

    // MUON Tracker
    simulator.SetSpecificStorage("MUON/Align/Data",
    "alien://folder=/alice/simulation/2008/v4-15-Release/Ideal");

    // Mag.field from OCDB
    simulator.UseMagFieldFromGRP();

    if ( 0 )
    {
      simulator.SetSpecificStorage("ITS/Align/Data",
      "alien://Folder=/alice/simulation/2008/v4-15-Release/Ideal");
      simulator.UseVertexFromCDB();
    }
  }

   // The rest
  TStopwatch timer;
  timer.Start();
  simulator.Run(nev);
  timer.Stop();
  timer.Print();
}
```

A.3.4 test.C

```

{
  gSystem->Load("libANALYSIS");
  gSystem->Load("libANALYSISalice");
  gSystem->Load("libCORRFW");
  gSystem->Load("libPWGmuon");
  gSystem->Load("libPWGmuondep");

  // Parton density functions
  gSystem->Load("liblhapdf");
  // TGenerator interface
  gSystem->Load("libEGPythia6");
  gSystem->Load("libpythia6_4_25");
  gSystem->Load("libAliPythia6");
  gSystem->AddIncludePath("-I$ALICE_ROOT");
  gSystem->AddIncludePath("-I$ALICE_PHYSICS");

AliMuonAccEffSubmitter a("GenParamCustomSingleForHF2",kFALSE,"4.25");

a.TemplateFileList()->Add(new TObjString("loadLibs.C"));
a.UseOCDBSnapshots(kFALSE);
a.SetRemoteDir("/alice/cern.ch/user/n/ndindika/
sim/FONLLnew/NewSimulationLHC12h_iT0");
a.ShouldOverwriteFiles(true);
a.SetCompactMode(1);
a.SetPackages("VO_ALICE@AliPhysics::vAN-20150410",
              "VO_ALICE@AliRoot::v5-06-12",
              "VO_ALICE@GEANT3::v1-15a-1");

a.MakeNofEventsPropToTriggerCount("CMSH8-S-NOPF-MUON",0.2);
a.SetRunList("runlist2LHC12hi.txt");
a.SetMaxEventsPerChunk(3000);
a.Print();
a.Run("full");
}
```